On lunar collision orbits:
new methodologies for Moon-to-Moon transfer design

Stefano Bonasera

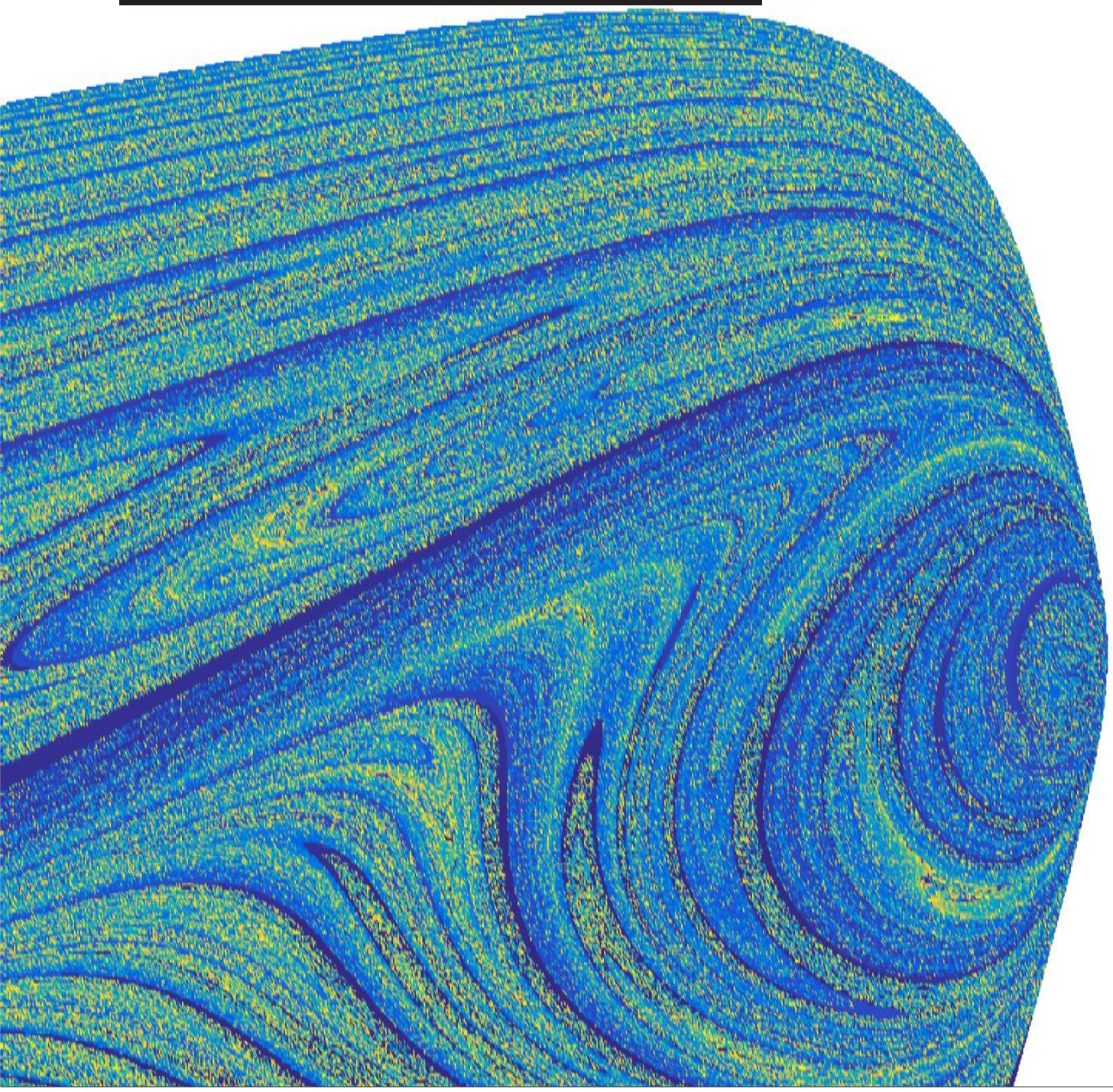

TU Delft Delft University of Technology

Challenge the future

On lunar collision orbits:

new methodologies for Moon-to-Moon transfer design

by

Stefano Bonasera

to obtain the degree of Master of Science
at the Delft University of Technology,
to be defended publicly on Friday October 20th, 2017 at 9:30.

Student number:	4519906	
Project duration:	February 2th, 2017 – July 31st, 2017	
Thesis committee:	Dr. D. M. Stam,	TU Delft (Chairholder)
	ir. R. Noomen,	TU Delt
	MSc MBA K. J. Cowan,	TU Delft
	Dr. F. Topputo,	TU Delft (supervisor)
	Prof. Dr. Y. Kawakatsu,	ISAS/JAXA (external supervisor)

An electronic version of this thesis is available at http://repository.tudelft.nl/.

The work here presented has been carried out at Institute of Space and Astronautical Science, part of the Japanese Aerospace Exploration Agency. Their hospitality is here acknowledged.

Acknowledgments

First of all I would like to thank my supervisor in TU Delft, prof. Francesco Topputo for his long-distance support and commendable will to guide me throughout this work. Grazie mille!

Next, I would like to thank prof. Yasuhiro Kawakatsu for his hospitality at JAXA and all the members of Kawakatsu lab. for the shown warmth in this six-month period in Asia. Without any doubt, it has been the most incredible and exciting experience of my life so far, from both the working and living perspective. I feel privileged and honoured of having being involved in a real mission design team. A special thank goes to my wingman and travel mate, Mattia. あ り が と う ご ざ い ま す

I am also very grateful for the support I received during the first year I spent in Delft from my classmates and friends, especially to Cristian and Giuseppe. Thanks for the moments you shared with me, I hope to see you all again somewhere in the future!

Vorrei ringraziare i miei genitori, per aver sempre supportato le mie decisioni, seppur mi abbiano portato lontano da loro. Grazie per avermi ascoltato, consigliato e sopportato in questi anni. Per ultimo, ringrazio Serena, per avermi sostenuto come amica e come sorella.

Stefano Bonasera
Delft, October 2017

Contents

List of Figures vii

List of Tables xi

Nomenclature xi

1 Introduction 1
- 1.1 Mission heritage . . . 1
  - 1.1.1 Hiten . . . 1
  - 1.1.2 EQUULEUS . . . 1
  - 1.1.3 DESTINY+ . . . 2
- 1.2 State of the Art . . . 2
- 1.3 Research questions & objectives . . . 3
- 1.4 Report content and structure . . . 4

2 Theoretical background 5
- 2.1 Dynamical system theory . . . 5
  - 2.1.1 Introduction to nonlinear systems . . . 5
  - 2.1.2 Autonomous vs nonautonomous . . . 6
  - 2.1.3 Poincaré map . . . 6
  - 2.1.4 State Transition Matrix and Differential Correction . . . 7
- 2.2 Dynamical model . . . 7
  - 2.2.1 CR3BP . . . 7
  - 2.2.2 BR4BP . . . 12
  - 2.2.3 Levi Civita regularization . . . 12
- 2.3 Optimization . . . 14
  - 2.3.1 Overview . . . 14
  - 2.3.2 Strategies . . . 14

3 Simple M2M transfer in the Earth–Moon CR3BP 17
- 3.1 Approach . . . 17
  - 3.1.1 Lunar ejection orbits . . . 18
  - 3.1.2 Propagation scheme . . . 19
  - 3.1.3 Ejection orbits and Poincaré cut . . . 20
- 3.2 Single M2M transfer . . . 21
  - 3.2.1 M2M transfer retrieval . . . 21
  - 3.2.2 M2M analysis . . . 24
- 3.3 Collision and Lyapunov orbits . . . 27
- 3.4 Conclusion and possible applications . . . 30

4 Extended M2M transfer in the Earth–Moon CR3BP 33
- 4.1 Ballistic multiple M2M transfer . . . 33
- 4.2 Controlled M2M transfer . . . 35
  - 4.2.1 Single M2M transfer . . . 35
  - 4.2.2 Multiple M2M transfer . . . 40
- 4.3 Conclusions . . . 43

5 M2M transfer in the Sun–Earth–Moon BR4BP 45
- 5.1 BR4BP analysis . . . 45
- 5.2 Single M2M transfer . . . 47
  - 5.2.1 M2M transfer with a pseudo-Poincaré cut . . . 47
  - 5.2.2 M2M transfer from double-collision orbits . . . 49

5.3 Multiple M2M transfer . . . 52
5.3.1 Multiple M2M transfer on a pseudo-Poincaré cut . . . 52
5.3.2 Database of double-collision M2M transfer . . . 54
5.4 Conclusions . . . 56

6 Conclusions **59**
6.1 Achievements . . . 59
6.2 What follows . . . 60
6.3 Possible future research . . . 61

A Derivation **65**

B Code validation **69**

Bibliography **73**

List of Figures

2.1 Representation of the P_1P_2-barycentric reference frame, in both the inertial and synodic form. In this exemplary case $\mu = 0.1$. 8

2.2 Example of the Zero Velocity Curves (grey) for different values of $\bar{C}$. Note how, by decreasing their values, the available space widens. **(a)** $\bar{C}_{L_2} < \bar{C} < \bar{C}_{L_1}$; **(b)** $\bar{C}_{L_3} < \bar{C} < \bar{C}_{L_2}$; **(c)** $\bar{C}_{L_{4,5}} < \bar{C} < \bar{C}_{L_3}$; 10

2.3 Example of three HLOs' associated with the collinear Lagrange points, for $\bar{C} \approx 3.0115$. 11

2.4 **(a)** Stable (green) and unstable (red) invariant manifold emanating from the HLO at L_2 (dashed black line) for $\bar{C} \approx 3.0514$. Earth and Moon as black dots, Lagrange points as red dots. ZVC in grey; **(b)** magnification of the stable manifold of (a) in proximity of the Moon. Manifold propagated for $t \approx 55$ terrestrial days. 11

2.5 Geometry of the BR4BP in the synodic P_1P_2-barycentric reference frame. a_s not in scale. 12

2.6 Architecture of the algorithm used for optimization 14

3.1 Example of a lunar ejection orbit (blue) for $\bar{C} = 3.1$ and $\theta_C = 5\pi/8$. Zero Velocity Curve outlined in grey. Earth and Moon depicted as black dots at $(x, y) = (-\mu, 0)$ and $(x, y) = (1-\mu, 0)$ respectively. Lagrange points L_1 and L_2 in red. 18

3.2 **(a)** Linear correlation between collision angle θ_C and ejection angle θ_E; **(b)** Example of lunar ejection orbits (red) for different initial collision angles θ_C at $\bar{C} = 3.1$. Moon represented by the black circle, while its center being the black dot at $(x, y) = (1-\mu, 0)$. 18

3.3 79 computed orbits with random initial conditions. Difference between final and initial Jacobi constant $\bar{C}$ vs. frequencies N for **(a)** Levi Civita and **(b)** Cartesian scheme; **(c)** computational speedup: Levi Civita divided by Cartesian. The integration time is set at $t \approx 434$ terrestrial days. 19

3.4 The same initial condition of one lunar ejection orbit is here propagated for $t \approx 218$ days, using different $n = \{1, 2, \ldots, 100\}$ as number of lunar radii for switching the propagation scheme from Levi Civita to Cartesian. Precision of the algorithm, in the shape of Jacobi constant $\bar{C}$ difference between the end and start of the trajectory is reported in the y-axis. 20

3.5 Poincaré cut examples with lunar ejection orbits (blue); **(a)** x-axis Poincaré cut, yellow intersections; **(b)** y-axis Poincaré cut, green intersections. Earth and Moon depicted as black dots at $(x, y) = (-\mu, 0)$ and $(x, y) = (1-\mu, 0)$ respectively. Lunar Hill's sphere reported as a dashed black circle around the Moon. 21

3.6 Intersections of 12000 backward-propagated lunar ejection orbits with the Poincaré cut on the positive y-axis. First encounter only, with $\bar{C} = 2.97$ and $\dot{x} \geq 0$ at intersection is here shown; representation on the **(a)** $y\dot{y}$- and **(b)** $\dot{x}\dot{y}$-plane. 22

3.7 **(a)** $\left(1^{st}\text{ bw}, 2^{nd}\text{ fw}\right)_{y+}$ intersections (green and red respectively) with the positive y-axis. $\bar{C} = 2.97$ and $\dot{x} \geq 0$; **(b)** to **(d)** propagated orbits from the cut, according to the location in (a). Backward- and forward- propagated transfers in red and green respectively. Earth and Moon as black dots. Lunar Hill's sphere depicted as a dashed circle about the Moon. 23

3.8 **(a)** Location of the propagated points on the y-axis Poincaré cut, for $\bar{C} = 2.97$, with $\dot{x} \geq 0$; **(b)** magnified view of (a); **(c)** resulting propagated orbits from the intersection points in (a) in (yellow point) and red (green point). Earth and Moon depicted as black dots, lunar Hill's sphere as dashed black circle about the Moon; **(d)** magnified view of (c) in a neighbourhood of the Moon. Starting and ending states for the trajectories depicted in green and red respectively. 23

3.9 **(a)** General view of the studied area (black box) of the whole domain. $\left(1^{st}\text{ bw}, 2^{nd}\text{ fw}\right)_{y+}$ intersections (green and red, respectively), with $\dot{x} \geq 0$ and $\bar{C} = 3.01$; **(b)** magnification inside the black box. 24

3.10 $\left(1^{st}\text{ bw}, 2^{nd}\text{ fw}\right)_{y+}$ intersections (green and red, respectively), with $\dot{x} \geq 0$, $\bar{C} = 3.01$; colors show perilunes for **(a)** backward- and **(b)** forward-propagated trajectories; **(c)** black dots report the propagation points satisfying the M2M transfer requirements. 25

3.11 $\left(1^{st}\text{bw}, 2^{nd}\text{fw}\right)_{y+}$ intersections (green and red, respectively), with $\dot{x} \geq 0$ and $\bar{C} = 3.01$; **(a)** on the z-axis the angular momentum with respect to the Moon, h_2, at perilune for the backward-integrated arcs; **(b)** top-view of (a); **(c)** on the z-axis the angular momentum with respect to the Moon, h_2, at perilune for the forward-integrated arcs; **(d)** top-view of (c). 25
3.12 $\left(1^{st}\text{bw}, 2^{nd}\text{fw}\right)_{y+}$ intersections (green and red, respectively), with $\dot{x} \geq 0$ and $\bar{C} = 3.01$; **(a)** on the z-axis the energy with respect to the Moon, H_2, at perilune for the backward-integrated arcs; **(b)** top-view of (a); **(c)** on the z-axis the energy with respect to the Moon, H_2, at perilune for the forward-integrated arcs; **(d)** top-view of (c). 26
3.13 Second-order intersections of the forward-propagated lunar collision orbits (red) with the Poincaré cut on the positive y-axis, for $\bar{C} = 3.01$ and $\dot{x} \geq 0$; grid of points propagated backward in time, reporting **(a)** minimum perigee heights and **(b)** the associated time to reach the perigee. 27
3.14 **(a)** First order intersections of the backward-propagated lunar collision orbits (green) and the stable invariant manifolds of the L_2 HLO (black) with the Poincaré cut at the positive y-axis; **(b)** second order intersections of the forward-propagated lunar collision orbits (red) and the unstable invariant manifolds of the L_2 HLO (black) with the Poincaré cut at the positive y-axis; $\bar{C} = 3.01$ and $\dot{x} \geq 0$. 27
3.15 **(a)** Forward-integrated collision orbit (straight yellow) and orbit approaching L_2 HLO on the stable manifold (dashed magenta), from two close initial points on the Poincaré cut. Zero Velocity Curve highlighted in grey. Earth and Moon depicted as black dots; **(b)** magnification of (a) in a neighbourhood of the Moon. 28
3.16 First order intersections of lunar ejection orbits (green) and the stable invariant manifold of **(a)** L_1 (magenta) and **(b)** L_2 (cyan) HLOs' with the Poincaré cut at the positive y-axis. 28
3.17 Trend of H_2 at perilune (in blue) for trajectories propagated from the Poincaré cut; **(a)** first-order intersections of backward-propagated lunar ejection orbits (green) with stable invariant manifold of L_2, L_1 and L_3 HLOs' (black, magenta and cyan respectively); in blue, H_2 for forward-propagated trajectories; **(b)** top-view of (a); **(c)** second-order intersections of forward-propagated lunar ejection orbits (red) with unstable invariant manifold of L_2, L_1 and L_3 HLOs' (black, magenta and cyan respectively); in blue, H_2 for backward-propagated trajectories; **(d)** top-view of (c). 29
3.18 **(a)** & **(b)** $\left(1^{st}\text{bw}, 2^{nd}\text{fw}\right)_{y+}$ intersections (green and red respectively) and stable invariant manifolds from L_2 and L_3 HLOs' (black and cyan respectively). $\bar{C} = 3.01$. Earth-M2M-escape ballistic sequence propagated from the cyan dot of (a) depicted in **(c)** and **(d)** for the synodic barycentric and Earth-centered inertial reference frames ($\approx$ 238 days); Earth-M2M-HLO in L_2 ballistic sequence propagated from the yellow dot of (b) depicted in **(e)** and **(f)** for the barycentric synodic and Earth-centered inertial reference frames ($\approx$ 208 days); Earth-M2M-HLO in L_3 ballistic sequence propagated from the magenta dot of (b) depicted in **(g)** and **(h)** for the barycentric synodic and Earth-centered inertial reference frames ($\approx$ 313 days). Earth and Moon are black dots in the synodic frame, while lunar Hill's sphere is as a dashed circle. Lunar orbit about the Earth plotted as a dashed circle in the inertial frame. 31

4.1 **(a)** $\left(1^{st}\text{bw}, 3^{rd}\text{bw}, 2^{nd}\text{fw}, 4^{th}\text{fw}\right)_{y+}$ intersections (green, cyan, red and orange respectively) with the Poincaré cut on the positive y-axis with $\bar{C} = 3.01$ and $\dot{x} \geq 0$; **(b)** magnification of (a), with highlighted the candidate points for the propagation (7207, black), the actual points generating a sequence of three and two M2M transfers (yellow, 1136 $\approx$ 16% and magenta, 889 $\approx$ 12% respectively). Mind how every sequence of three M2M transfers can be regarded as two distinct sequences of two M2M transfers. 34
4.2 **(a)** Example of a sequence of three M2M transfers. Earth and Moon depicted as black dots, lunar Hill's sphere as a dashed circle about the Moon; **(b)** magnification of (a) about the Moon. Green and red dots marking the start and end of the trajectory, respectively; **(c)** trend in time of r_2 and H_2 (red and blue, respectively) for the trajectory highlighted in (a) and (b). 34
4.3 Different trajectories (blue) propagated for the amount of time needed by EQUULEUS engine ([22]) to perform a maneuver of **(a)** $\Delta v = 1$ m/s, **(b)** $\Delta v = 5$ m/s, **(c)** $\Delta v = 12$ m/s. Earth and Moon depicted as black dots, lunar Hill's sphere as dashed circle about the Moon. 35
4.4 **(a)** location of the propagation points on the $\left(1^{st}\text{bw}, 2^{nd}\text{fw}\right)_{y+}$ Poincaré cut; **(b)** trajectories propagated forward and backward in time from the black dots in (a). Initial and final points marked by green and red dots respectively. 36

4.5 **(a)** Corrected trajectories (straight lines) compared to unperturbed ones (dashed lines). Impulses given by black arrows and magnified by a factor of 15. Initial and final state depicted as green and red points respectively; **(b)** Time of the impulse with respect to perilune vs magnitude of the impulse. Red and green points represent the plotted case in (a), as well as the minima for the corrected red and green dashed trajectories. 37

4.6 **(a)** Corrected trajectories (straight lines) compared to unperturbed ones (dashed lines). Impulses given by black arrows and magnified by a factor of 15. Relative impulses' magnitudes reported in Table 4.2. Initial and final state depicted as green and red points respectively. Red and green trajectories last for about 90 and 70 terrestrial days, respectively; **(b)** result of the optimizing algorithm in terms of piercing the Poincaré cut, from the unperturbed black dots to the optimized blue points. 38

4.7 Corrected trajectories (straight lines) vs unperturbed ones (dashed lines). Impulses given by black arrows and magnified by a factor of 15. Impulses' magnitudes reported in Table 4.2. Initial and final state depicted as green and red points respectively. Red and green trajectories last for about 90 and 70 terrestrial days, respectively. Two different initial guesses used for **(a)** and **(b)**. . 39

4.8 Corrected trajectories (straight lines) vs unperturbed ones (dashed lines). Initial and final state depicted as green and red points respectively. Red and green trajectories last for about 90 and 70 terrestrial days, respectively; **(a)** two impulses per trajectory, $\bar{V} = 5$ m/s, magnification by a factor of 50; **(b)** five impulses per trajectory, $\bar{V} = 1.5$ m/s, magnification by a factor of 300. Data reported in Table 4.3 40

4.9 **(a)** first-order intersections of the backward-propagated lunar collision orbits with the cut at the negative x-axis, with $\bar{C} \approx 2.962$ and $\dot{y} \geq 0$; **(b)** top-view of a collection of intersections of first-order intersections of backward-propagated lunar collision orbits with the same cut as in (a), for a the range $\bar{C} \in \{2.930, 2.935, \ldots, 3.000\}$; **(c)** 3D-view of (b); **(d)** side-view of (b). 41

4.10 **(a)** Path among the different cuts of the perturbed trajectory in (d). Initial, mid and ending points marked in green, black and red; **(b)** top-view of (a); **(c)** side view of (a); **(d)** resulting trajectory (blue) from (a). Clearly notice the location of the start, mid and ending points (green, black and red) at the intersections with the cut. 42

4.11 Trend of the value of $\bar{C}$ for the trajectory depicted in Fig. 4.10d. Notice how the last jump misses since no correction is needed. 43

5.1 Lunar ejection orbits propagated for ≈ 65 days with the BR4BP and CR3BP dynamical models (straight blue and dashed red, respectively) with an equal initial $\bar{C}$ for an **(a)** inbound and **(b)** outbound initial Sun's phase angle θ_{S0}. ZVC depicted in grey, while Earth and Moon as black dots. Synodic barycentric reference frame. 46

5.2 Lunar ejection orbits propagated for ≈ 30 days with the BR4BP dynamical model, with an increasing initial Sun's phase angle θ_{S0} (from red to blue); **(a)** inbound initial ejection angle; **(b)** outbound initial ejection angle. Earth and Moon depicted as black dots, while lunar's Hill's sphere as dashed black circle. Synodic barycentric reference frame. 46

5.3 $\left(1^{st}\,\mathrm{bw}_0, 2^{nd}\,\mathrm{fw}_0\right)_{y+}$ intersections (green and red respectively) with the Poincaré cut on the positive y-axis, with $\dot{x} \geq 0$, $\bar{C}_0 = 2.97$. Black points representing the ones satisfying Eqs. (5.2) and (5.3), while cyan ones the one where actual M2M transfer are propagated from; **(a)** 3D-view; **(b)** top-view. 48

5.4 One example M2M transfer out of the obtained 796 results in Fig. 5.3; **(a)** synodic barycentric reference frame. Earth and Moon depicted as black dots, lunar Hill's sphere as black dashed circle about the Moon; **(b)** Earth-centered inertial reference frame. Lunar orbit depicted as dashed black line. Starting and ending point marked as green and red dots respectively. 48

5.5 First-order intersections with the Poincaré cut on the x-axis for $x \in \left[1-\mu-R_{hill}; 1-\mu+R_{hill}\right]$ of lunar ejection orbits. Initial condition $\theta_{S0} = \pi/2$, $\bar{C}_0 = 2.97$; **(a)** view of the intersections of the ejection orbits with the cut in the $x\dot{y}$-plane. Lunar surface depicted as dashed black lines. See the classification in four different families; **(b)** shape of the different families. The cyan one is not reported since meaningless; **(c)** initial lunar collision angles for the different families. 49

5.6 Second-order intersections with the Poincaré cut on the x-axis at $x \in [1-\mu-R_{hill}; 1-\mu+R_{hill}]$ of lunar ejection orbits. Initial condition $\theta_{S0} = \pi/2$, $\bar{C}_0 = 2.97$; **(a)** view of the intersections of the ejection orbits with the cut in the $x\dot{y}$-plane. Lunar surface depicted as dashed black lines. See the classification in seven different families; **(b)**, **(c)** and **(d)** shape of the different families; **(e)** initial lunar collision angles for the different families. 50
5.7 Fourth-order intersections with the Poincaré cut on the x-axis at $x \in [1-\mu-R_{hill}; 1-\mu+R_{hill}]$ of lunar ejection orbits. Initial condition $\theta_{S0} = \pi/2$, $\bar{C}_0 = 2.97$; **(a)** view of the intersections of the ejection orbits with the cut in the $x\dot{y}$-plane. One family only here reported, similar to family-g' from [10]; **(b)** shape of the green family shown in (a); **(c)** initial lunar collision angles for the green family. 51
5.8 $\left(1^{st}\text{bw}_0, 3^{rd}\text{bw}_0, 2^{nd}\text{fw}_0, 4^{th}\text{fw}_0\right)_{y+}$ intersections (green, cyan, red and yellow respectively) of lunar ejection orbits with the Poincaré cut on the positive y-axis, for $\dot{x} \geq 0$ and $\bar{C}_0 = 2.97$; **(a)** 3D-view; **(b)** top-view. 52
5.9 **(a)** Example of a ballistic sequence of three M2M transfers in the BR4BP dynamical model. Earth and Moon depicted as black dots, lunar Hill's sphere as a dashed circle about the Moon; **(b)** magnification of (a) about the Moon. Green and red dots marking the start and end of the trajectory, respectively; **(c)** trend in time of r_2 and H_2 (red and blue, respectively) for the trajectory highlighted in (a) and (b). 53
5.10 **(a)** Single (black) and double (red) double-collision M2M satisfying Eq. (5.8). $\Delta\bar{C}$ vs cumulative TOF. Green point representing the double double-collision M2M transfer depicted in (b) to (d); **(b)** trajectory in the inertial Earth-centered reference frame from the green point in (a). Sun's position depicted in dashed red line (not in scale). Mind how the starting and ending points overlap (green and red), being the latter the one coming from the hyperbolic-like trajectory about the Earth. Sun's path too is marked by same starting and ending points; **(c)** trajectory in (b) in the synodic barycentric frame; **(d)** trend of Jacobi constant $\bar{C}$ (blue), distance from the Moon r_2 (green) and scaled energy with respect to Earth E (red) vs time. Vertical dashed black line marking the patching. 56

6.1 Different views for the intersections of the backward-propagated ejection orbits of the JE-system up to the fifth order (green) and the forward-propagated of the JG-one up to the sixth order (red) in the $y\dot{y}\bar{C}_{JE}$-space. The former obtained with a $\bar{C}_{JE} = 2.97$, while the latter with a $\bar{C}_{JG} = 2.9$; **(a)** top-, **(b)** $y\bar{C}$-side, **(c)** $\dot{y}\bar{C}$-side and **(d)** 3D-view, respectively. 62
6.2 Example transfer generated from propagating two initial conditions on the cut distant 4.5×10^{-4} in the $y\dot{y}\bar{C}_{JE}$-space. The transfer starts from Ganymede (green point) along the red trajectory, switching system at the yellow point, representing the Poincaré-cut. The transfer culminates at the red point, namely Europa. Starting propagation points are retrieved from the 21^{st} intersections of the JE-system and the 4^{th} from the JG-one. Transfer time is 90 terrestrial days; **(a)** Jupiter-centered inertial reference frame; **(b)** JE barycentric reference frame. 63

B.1 **(a)** Orbits from [21] (straight red) compared to the ones originated from the dynamical model employed in this report (dashed blue) for different starting collision angles θ_C; **(b)** difference in $\bar{C}$ between straight red and dashed blue orbits of (a) versus the relative value of θ_C. 69
B.2 **(a)** (x) trajectory (blue) in the Earth-centered inertial reference frame from Fig. 8 of [29], propagated with the dynamical model used in this report. Earth referred to as black central dot, while lunar circular orbit depicted as a dashed black line; **(b)** magnification of (a), in the synodic barycentric reference frame. Ending point for the trajectory (red dot) intersects the 100 km circular orbit (dashed black line) about the Moon (straight black line). 70
B.3 Trend of Jacobi constant difference $\Delta\bar{C} = |\bar{C}_{start} - \bar{C}_i|$ compared to time. Two different orbits compared in **(a)** and **(b)** respectively, revolving in the vicinity of the system (i.e. not spiralling outwards). `ode113`, `ode45` and `ode78` in blue, red and green respectively. 71

List of Tables

1 List of Roman symbols [1]. In case symbols have multiple units, the latter are not indicated. . . xiii
2 List of Roman symbols [2]. In case symbols have multiple units, the latter are not indicated. . . xiv
3 List of Greek symbols. In case symbols have multiple units, the latter are not indicated. xiv
4 List of approximated constants. Taken from [1, 18]. xiv
5 List of Acronyms. xv
6 List of other symbols. In case symbols have multiple units, the latter are not indicated. xv

2.1 Coordinates and associated Jacobi constant values for the collinear Lagrange points. 10
2.2 Main orbital data for Earth and the Moon, with respect to the Sun and Earth respectively. Table shows their average semi-major axis, periods, eccentricities and inclinations (with respect to Earth's orbit about the Sun), respectively from left to right. Mind how Earth's inclination about the Sun is null since the ecliptic is taken as reference plane. A single day refer to one terrestrial day, namely 86400 s (taken from Acton [1], Lissauer and de Pater [18]). 12

4.1 EQUULEUS' engine characteristics ([22]). I_{sp} indicates the specific impulse, M the mass and $\bar{T}$ the thrust. 35
4.2 Δvs' and $\Delta\bar{C}$s' of the different optimized perturbed trajectories. 39
4.3 Δvs' and $\Delta\bar{C}$s' of the different optimized perturbed trajectories in Fig. 4.8 40
4.4 Characteristics of the impulses associated with the trajectory in Fig. 4.10d. 43

5.1 Statistics concerning ballistic sequences of M2M transfers. Mind how every sequence of three M2M transfers can be regarded as two different sequences of double M2M transfers: however, this is not considered in the shown numbers. Moreover, notice how the triple and double percentages are higher than what shown in Fig. 4.1. 53

6.1 Main orbital data for both Europa and Ganymede, second and third Galilean moon of Jupiter respectively, with respect to Jupiter. Table shows their average semi-major axis, periods, eccentricities and inclinations (Jupiter's equator as a reference), respectively from left to right. A single day refer to one terrestrial day, namely 86400 s (constants taken from Acton [1], Lissauer and de Pater [18]). 61

B.1 Computational time for the two orbits in Fig. B.3 for the different propagation schemes. 70

Nomenclature

Symbol	Description	Unit
a	Semi-major axis	m
a_u, b_u, c_u	Levi Civita parameter functions	-
$\bar{a}$, $\bar{d}$	Generic constants	-
A, A^*, C^*, D^*, D, I, S, $\boldsymbol{S}$, V	Subsets	-
$A(t)$	Jacobian of the system	-
$\boldsymbol{c}$, $\boldsymbol{c}_{eq}$	Nonlinear equality and inequality constraints	-
$\bar{C}$	Jacobi constant	-
d	Distance function	-
$D_{\boldsymbol{x}}$	Jacobian	-
e	Eccentricity	-
E	Energy	-
$\boldsymbol{f}$, $\boldsymbol{g}$	Generic functions	-
F	Cost function	-
$\boldsymbol{F}$	Force	N
h_2	Angular momentum with respect to the secondary	-
H	First Integral	-
H_2	Energy with respect to the secondary	-
i	Inclination	deg
I_{sp}	Specific impulse	s
J	Jacobi integral	-
L_1, L_2, …, L_5	Lagrange points	-
l	Switching radius	-
m_1, m_2, m_S	Mass of the main bodies	kg
M	Mass	kg
n, m	Orders	-
$\bar{n}$	Orbital mean motion	rad/s
N	Number of particles	-
P	Poincaré map	-
P_i	i^{th} point	
P-cut$_{y,\dot{y}}$	Intersection set with the Poincaré cut	-
r_1, r_2	Distances from primaries	-
r_S	Distance from fourth body	-
r_y, $r_{\dot{y}}$, r_{θ_S}	Semi-major axes	-
$\boldsymbol{r}$, $\boldsymbol{R}$	Position vectors	-
R_{Hill}	Hill's sphere radius	-
t	Time	s
T	Period	s
$\bar{T}$	Thrust	N
$\boldsymbol{u}$	Regularized state	-
U, U_3, U_4	Potential functions	-
v	Velocity	-

Table 1: List of Roman symbols [1]. In case symbols have multiple units, the latter are not indicated.

Symbol	Description	Unit
v_2	Velocity with respect to the secondary	-
$\boldsymbol{v}_2$	Velocity vector with respect to the secondary	-
$\boldsymbol{v}$, $\boldsymbol{V}$	Eigenvectors	-
$\bar{V}$	Velocity boundary	m/s
W	Invariant manifold	-
x, y	Spatial coordinates in synodic frame	-
$\dot{x}$, $\dot{y}$	Velocity coordinates in synodic frame	-
$\ddot{x}$, $\ddot{y}$	Acceleration coordinates in synodic frame	-
X, Y	Spatial coordinates in inertial frame	m
$\dot{X}$, $\dot{Y}$	Velocity coordinates in inertial frame	m/s
$\boldsymbol{x}$	State	-

Table 2: List of Roman symbols [2]. In case symbols have multiple units, the latter are not indicated.

Symbol	Description	Unit
α	Deflection angle	deg
δ	Infinitesimal difference	-
Δ	Difference	-
ϵ	Small quantity	-
θ	Phase angle	deg
θ_C	Lunar collision angle	deg
θ_E	Lunar ejection angle	deg
θ_S	Sun's phase angle	deg
ϕ	Flow	-
$\phi_{j,k}$	(j, k)th term of the STM	-
Φ	State Transition Matrix	-
ψ	Periodic solution	-

Table 3: List of Greek symbols. In case symbols have multiple units, the latter are not indicated.

Symbol	Description	Value	Unit
a_S	Scaled Sun–(Earth–Moon) distance	388.81114	-
DU	Unit of distance	3.844×10^8	m
G	Universal gravitational constant	6.67408×10^{-11}	$m^3/kg\,s^2$
M_{Earth}	Mass of the Earth	5.97237×10^{24}	kg
M_{Moon}	Mass of the Moon	7.34603×10^{22}	kg
M_{Sun}	Mass of the Sun	1.98848×10^{30}	kg
μ_{EM}	Earth–Moon mass parameter	0.01215	-
μ_S	Solar mass parameter	3.289001×10^5	-
R_{Moon}	Mean lunar radius	1737.4	km
TU	Unit of time	4.3425646	days
VU	Unit of velocity	1.02454×10^3	m/s
ω_S	Scaled solar angular velocity	-9.25196×10^{-1}	-

Table 4: List of approximated constants. Taken from [1, 18].

Symbol	Description
$BR4BP$	Bi-circular Restricted Four Body Problem
$CR3BP$	Circular Restricted Three Body Problem
$DESTINY+$	Demonstration and Experiment of Space Technology for INterplanetary voYage +
$EQUULEUS$	EQUilibriUm Lunar-Earth point 6U Spacecraft
EM	Earth–Moon
$G2E$	Ganymede to Europa
HLO	Horizontal Lyapunov Orbit
IES	Ion Engine System
$ISAS$	Institute of Space and Astronautical Science
$JAXA$	Japanese Aerospace Exploration Agency
JE	Jupiter–Europa
JG	Jupiter–Ganymede
LSB	Lunar Swing-By
$M2M$	Moon-to-Moon
$NASA$	National Aeronautics and Space Administration
SLS	Space Launch System
SOI	Sphere Of Influence
STM	State Transition Matrix
TOF	Time Of Flight
ZVC	Zero Velocity Curve

Table 5: List of Acronyms.

Symbol	Description
$\mathscr{I}$	Identity matrix
$\mathscr{J}$	Projection of a $J(\boldsymbol{x}) = \bar{C}$
$\mathscr{G}$	Region
$\mathbb{N}$	Set of natural numbers
∇	Nabla
$\mathscr{O}$	Landau's big O
$\mathbb{R}$	Set of real numbers

Table 6: List of other symbols. In case symbols have multiple units, the latter are not indicated.

Abstract

Many interplanetary missions massively leverage the lunar gravitational pull in the so-called low-energy regime to converge to their aim, saving consistent amount of fuel. Among these, two future Japanese spacecraft are expected to repeatedly encounter the Moon along their trajectories to either facilitate the escape from the Earth–Moon system or opportunely target a specific region in its neighbourhood. Although never actively employed for preliminary trajectory design, lunar collision orbits have shown a rich dynamical structure and an applicability for both medium- and low-energy regimes. These characteristics, together with their intrinsic nature of being close to trajectories experiencing lunar fly-by, have encouraged this research.
In this work, lunar collision orbits are employed to delineate a method for obtaining ballistic transfers between two successive lunar encounters, briefly addressed as Moon-to-Moon. This study is first carried out with the assumptions of the autonomous Circular Restricted Three-Body Problem, subsequently extended to the nonautonomous Bi-circular Restricted Four-Body Problem, including the solar gravitational influence. Poincaré cuts are extensively used as a dimensionality reductant for lunar collision orbits: this allows to ascertain their similar behaviour with trajectories flybying the Moon, whose characteristics are partly foreseen by determining the associated intersection with the same cut. A patching is performed at the cut to obtain both single and multiple ballistic Moon-to-Moon transfers. The strict bond of lunar collision orbits with the invariant manifolds of simple periodic orbits about Lagrangian points is confirmed and exploited to design ballistic itineraries connecting highly elliptic orbits about the Earth to horizontal Lyapunov orbits of the Earth–Moon system, via a single Moon-to-Moon transfer. With the usage of the lunar collision orbits and the Poincaré cut, a simple optimization technique is implemented to retrieve a properly defined Moon-to-Moon transfer from a trajectory missing a second fly-by with the Moon.
Including the presence of the Sun, a similar method for obtaining single and multiple Moon-to-Moon transfers is developed. A classification of lunar double-collision transfers is then performed within the same framework, highlighting their similarity with other studies in past literature, eventually leading to the construction of a database of Moon-to-Moon transfers. The latter, conceived as an improvement with respect to the former version by adding the lunar gravitational influence, shows its applicability in real preliminary trajectory design.

1 Introduction

This chapter introduces to the research performed by the author in his six-month period at ISAS, JAXA, in Sagamihara, Japan.
The structure is divided in four parts. In Section 1.1 a brief description of Japanese past and future space missions is outlined: two of them are taken as examples within this report. A short literature review concerning the main aspects treated in this work is addressed in Section 1.2, followed by the definition of the main research questions and objectives in Section 1.3. Concluding, the structure of the whole report is delineated in Section 1.4.

1.1. Mission heritage

In this section, examples from past and future space missions are introduced: in particular, higher attention is given to the trajectory design part for those missions exploiting the low-energy domain, in agreement with the framework of this report. In Section 1.1.1, JAXA's Hiten mission is presented, followed by other two future Japanese missions, namely EQUULEUS and DESTINY+, reported in Sections 1.1.2 and 1.1.3, respectively. The author is particularly attached to the latter two since he has been actively involved in their trajectory design teams during his interning. As a further reason, this whole work has been conceived to help in the analysis of the preliminary trajectory for both missions.

1.1.1. Hiten

Hiten (also known as MUSES-A) was the first space experimental satellite of the Institute of Space and Astronautical Science (ISAS), now within the Japanese Aerospace Exploration Agency (JAXA). The demonstration of a double lunar swing-by (Moon-to-Moon) was the primary aim among the mission objectives [30, 31].
On the 24th of January 1990, Hiten was launched on a highly elliptical orbit around the Earth; however, its first apogee was 200,000 km below the nominal 470,000 km, therefore, after inquiring a database of *failure*-case trajectories, wisely prepared before the launch, the engineers allowed the spacecraft to perform a first corrective maneuver. In its whole trajectory, Hiten actively employed lunar resonances and solar perturbation (especially during the last part of the mission) to achieve a total of ten lunar fly-bys (with several correction maneuvers) and two Earth aerobreaking maneuvers. After the final one, about half of the initial fuel was still unused, therefore the mission was extended: first, a looping around Earth–Moon fourth and fifth Lagrange points was executed, followed by a lunar insertion maneuver, which ended up with a crash on the Moon's surface. Hiten represents the pioneer among the past space missions which effectively employed a low-energy trajectory, in order to recover from the missed ejection conditions.

1.1.2. EQUULEUS

JAXA's EQUULEUS (EQUilibriUm Lunar-Earth point 6U Spacecraft) is one of the selected CubeSat missions which will be piggybacked by the Space Launch System (SLS) during its first flight for NASA's Exploration-Mission 1, recently re-scheduled for 2019. Developed as a joint mission between the University of Tokyo and ISAS/JAXA, the trajectory design part is entirely performed by the latter. The aim is to lead the spacecraft towards a *quasi-halo* orbit of the second Earth–Moon Lagrange point, demonstrating the controllability of a CubeSat with a low-thrust engine under luni-solar perturbations. Up to the current baseline [22], the avail-

able Δv budget is 80 m/s, employed for correction and clean-up maneuvers first and station-keeping activity later.
The constraints on the initial state for the trajectory design are dictated by the SLS, which ejects the spacecraft with a considerable energy: due to its final aim, EQUULEUS trajectory is designed to reduce its energy. After the first close lunar fly-by, Sun's perturbation will be heavily exploited in order to lower down the energy of the spacecraft. The overall trajectory consists of a multiple step approach. A first grid search is performed, intersecting forward and backward arcs at their apogees: the former is obtained by propagating from the initial condition at ejection while the latter from the quasi-halo orbit. Subsequently, these trajectories are optimized to fill the *state-gap* at the closest patching points, by providing impulsive Δvs' along the arcs. Concluding, the optimal trajectories are again optimized to substitute the impulses with finite-burn arcs.
The trajectory for EQUULEUS is both a challenging and interesting task: the initial condition at ejection has changed already numerous times and the available fuel is rather low.

1.1.3. DESTINY+

DESTINY+ (Demonstration and Experiment of Space Technology for INterplanetary voYage +) is an ISAS/JAXA deep-space small-size science mission [35] expected to be launched in 2020 onboard the Japanese Epsilon rocket: the first objective of DESTINY+ is to demonstrate the usage of Japanese Ion Engine System (IES) for an interplanetary spacecraft leveraging lunar gravitational pull, which will eventually aim at an encounter with Asteroid (3200) Phaethon.
After the injection on an extended elliptical orbit, the spacecraft will use its IES to allow for a first lunar encounter, while exploiting lunar resonances at the very last phase of its raising spiralling. A sequence of lunar encounters, defined as Moon-to-Moon (M2M) transfers, will increase the energy of the spacecraft for its escape from the Earth–Moon region; in this intermediate phase, solar gravitational influence will be properly used to obtain a favourable final condition, before pointing towards Phaethon [4].
Hence, trajectory design has been preliminarily divided into three phases, each one corresponding to a specific arc: for what concerns the mid-phase (escaping from the Earth–Moon region), a toolbox using a database of M2M transfers [36] has been designed to obtain feasible trajectories which will target a specific energetic final condition, producing a multitude of initial conditions. Being a preliminary assessment, this toolbox will be further refined to account for a specific final condition, to be *jointed* with the initial condition of the final phase; a similar scenario happens for the final condition of the early phase with the initial condition of the intermediate one. A possible mission extension to visit other small bodies is under study [4].
Similarly to EQUULEUS, this mission is rather challenging. Indeed, as indicated above, the study of the preliminary trajectory is divided in three phases: finding the optimum for the whole trajectory, obtained by patching together the different arcs, is not a straightforward task. For this reason subsequent refinements of the whole trajectory will be needed.

1.2. State of the Art

This work is motivated by contemporary needs within the space industry and triggered by new discoveries in the realm of space trajectory design. Being a really wide research area, the main topic has been narrowed down to a study of trajectories starting and ending in proximity of the Moon. These kind of transfers are briefly referred throughout this work as Moon-to-Moon (M2M).
The spark igniting the idea behind this research comes from an industrial need: in a real trajectory design scenario, where both lunar and solar gravitational influences are employed, the availability of a database of M2M transfers becomes a necessity for a fast and reliable preliminary design. This idea has been first pointed out by Lantoine and McElrath [15] who discussed the applicability of a database of ballistic M2M transfers (namely without any mid-course maneuver) within the low-energy framework of the Sun–Earth planar Circular Restricted Three Body Problem (CR3BP). Although this survey represents a good starting point, demonstrating a direct applicability of the developed database in two different space mission trajectories, it employs a rather simplified dynamics, since it excludes the lunar gravitational pull from the model; this leads to a low fidelity of the transfers with respect to the real case, especially when the spacecraft approaches the Moon with a low level of relative velocity. Two limitations on spacecraft motion are evident: neither a multi-revolution case around the Earth between two consecutive encounters with the Moon nor an out-of-plane component of the trajectory is allowed.
In their recent work, Yarnoz et al. [36] managed to solve the former issue, while ongoing projects are carried out to allow for a 3D motion of the spacecraft in the construction of the database. Each of the previously

referenced work highlights a great computational effort in the definition of the database: this is due to the overwhelming amount of propagated trajectories.
A possible choice for a model which is dynamically closer to the full ephemeris one with respect to the CR3BP, therefore more correct, consists in taking in consideration the Sun, the Moon and the Earth together as gravitational bodies. In this case the researcher may bypass part of the dynamical troubles given by the increased number of bodies by constraining their relative motion: a possible representation is suggested by Simó et al. [27] and Topputo [29], where the planar Bi-circular Restricted Four Body Problem (BR4BP) is employed as a dynamical model for the computation of spacecraft trajectory. The latter adheres more precisely to the real case when compared to the similar result of the CR3BP: this makes it a valid alternative to overcome with the poor precision for relative low-velocity approach with the Moon, without extensively weighing on the propagation scheme. However the BR4BP dynamical model presents an important drawback: indeed, due to the constrained relative motion, Sun, Earth and Moon do not perfectly respect Newton's dynamics, which translates in a lack of coherency. Nevertheless this flaw is minimal and the intrinsic approximation within the model has shown an improvement in precision of the resulting trajectories when compared to the CR3BP case.
A recent discovery by Oshima et al. [21] on lunar collision orbits (namely orbits hitting the Moon) opens to new possibilities in the so-called *medium-energy* trajectory design regime. In their work, Oshima et al., by employing Levi Civita regularization scheme to the equations of motion (Lega et al. [16]), discovered that this type of orbits shapes a rich phase-space structure which perfectly separates two different kinds of motion for orbits approaching the Moon, namely prograde and retrograde. A similar separatrix behaviour, although associated to a different nature and pertaining a different dynamical characteristic, has already been observed in the invariant manifolds of the periodic orbits associated with the collinear Lagrangian points in the CR3BP, but at a low-energy level, as demonstrated by Conley [7], whose result were later used in different works for the computation of low-energy trajectories (Gómez et al. [8], Koon et al. [14], Parker and Anderson [23]). The usage of the invariant manifolds emanating from the periodic orbits of the Lagrange points is suggested for low-energy regime only, since at medium- and high-energy they lose their well-behaving nature, due to the close passage with the secondary body. Conversely, this problem is outflanked by the collision orbits which show a good behaviour on a wider and higher level of energies.
Even though representing a niche within the space trajectory design, the low- and the recently defined medium-energy regimes allow new and cheaper solutions for the design of space trajectories, although generally demanding a larger time to accomplish the transfer. By considering a higher number of main gravitational bodies the problem increases in complexity, although, depending on the case, this becomes necessary for obtaining a better preliminary trajectory. Eventually, collision orbits have shown an interesting structure, which needs to be further studied to gain insight in their underlying dynamics: accounting to the best of author's knowledge, they have never been actively employed for space trajectory design.

1.3. Research questions & objectives

In this section both the questions which gave birth and drove this research, together with the final objectives, are highlighted. The former are fully addressed by the establishment of two main research questions and relative sub-questions, while the latter are structured in two main research objectives and relative sub-goals, reported below.

Main research questions:

1 *Which useful information can lunar collision orbits provide to obtain Moon-to-Moon transfers within the framework of the Circular Restricted Three Body Problem and the Bi-circular Restricted Four Body Problem?*

2 *In the context of a preliminary trajectory design, to what extent can a database of Moon-to-Moon transfers benefit from the introduction of the gravitational pull of the Moon within the dynamical model?*

Sub-questions:

1.1 *What are the benefits of propagating an orbit with Levi Civita regularization scheme, when compared to Cartesian one?*

1.2 *To what extent can a Poincaré cut be employed for gaining insight within the dynamics of lunar collision orbits?*

1.3 *Which are the feasible strategies to opportunely correct a missing Moon-to-Moon transfer by means of impulsive maneuvers?*

2.1 *In which case should the Bi-circular Restricted Four Body Problem dynamical model be preferred to the simpler Circular Restricted Three Body Problem one?*

2.2 *Which key-characteristics of lunar collision orbits can be employed to design a database of Moon-to-Moon transfers?*

Main research objectives:

1 *Furnish a new solution to design transfers between two successive lunar encounters, by employing lunar collision orbits and Poincaré cuts within the framework of the Circular Restricted Three Body Problem and Bi-circular Restricted Four Body Problem.*

2 *Develop a new and more precise database of Moon-to-Moon transfers, by employing lunar double-collision orbits within the framework of the Bi-circular Restricted Four Body Problem.*

Sub-goals:

1.1 *Properly define what a Moon-to-Moon transfer is, from both a qualitative and quantitative perspective.*

1.2 *Understand the advantages and disadvantages of propagating trajectories with Levi Civita regularized scheme, when compared to the common Cartesian one.*

1.3 *Leverage Poincaré cut to obtain information concerning lunar collision orbits.*

1.4 *Employ the main characteristics of lunar collision orbits to obtain Moon-to-Moon transfers.*

1.5 *Understand the benefits of using different optimization strategies for correcting a Moon-to-Moon transfer by means of impulsive maneuvers.*

2.1 *Delineate which variables of the double-collision transfers need to be stored for a light and easy-to-inquiry database.*

2.2 *Define a fast and reliable algorithm for database construction.*

2.3 *Investigate both advantages and drawbacks of the new approach when compared to the former version.*

1.4. Report content and structure

The structure of this report is divided in five chapters, concerned with the different aspects of the performed research. Besides this introductive part, the theoretical background is outlined in Chapter 2, where the building blocks of this report are briefly discussed. Successively, the three main chapters of this work are reported: in Chapter 3 Moon-to-Moon transfers are presented within the dynamical model of the Circular Restricted Three-Body Problem. This chapter provides the answer to the first main question. Chapter 4 extends the concepts of the previous one, by including more complex themes of Moon-to-Moon transfer. The dynamical model is subsequently extended to encompass the solar influence in Chapter 5: here, with the Bi-circular Restricted Four-Body Problem model, the first main question receives its second answer, while the implementation of the new database replies to the second main research question. Concluding, in Chapter 6 a final summary of the achieved results and a critical overview of the whole work are presented, together with the proposal of an interesting new research topic. Supplementary material is gathered in Appendices A and B, reporting the derivation of the most relevant equations here employed and code validation, respectively.

2

Theoretical background

In this chapter, the main aspects of the theory constituting the backbone of this report are discussed. Dealing with low-energy trajectory design, in order to understand both the scientific outcome and the procedure followed throughout this work, this chapter is divided in three parts: Section 2.1 highlights the key-features of *dynamical system theory*, a branch of Mathematics which is severely employed in the treatment of nonlinear dynamical problems, while in Section 2.2 a general view of the dynamical model is reported, in order to properly grasp the physics behind spacecraft motion. Concluding, Section 2.3 outlines the basics concerning space trajectory optimization theory employed in this report.

2.1. Dynamical system theory

Dynamical system theory is a field of Mathematics focusing on nonlinear differential (or difference) equations. Specific tools of the latter are highlighted in this section, for a correct reading of this work. First, an introduction to the nonlinear systems is given in Section 2.1.1, followed by a general overview of autonomous and nonautonomous systems in Section 2.1.2. The theory behind Poincaré maps is presented in Section 2.1.3 while a concluding introduction to the State Transition Matrix and the Differential Corrector scheme is reported in Section 2.1.4. For a more in-depth analysis of the topic, refer to Verhulst [33].

2.1.1. Introduction to nonlinear systems

A general n^{th}-order differential equation can always be transformed in a n^{th}-dimensional system of first-order differential equations. In this work, the mathematical statement of the general problem is

$$\dot{\boldsymbol{x}} = \boldsymbol{f}(\boldsymbol{x}, t), \qquad \boldsymbol{x}(t_0) = \boldsymbol{x}_0 \tag{2.1}$$

defined as initial value problem. $\boldsymbol{x} \in D \subset \mathbb{R}^n$ represents the solution, $t \in I \subset \mathbb{R}$ refers to the independent variable (usually time), while $\boldsymbol{f} : A \longrightarrow \mathbb{R}^n$, with $A \subset \mathbb{R}^{n+1}$, is a vector function, shaping how the solution evolves in time. The nonlinearity of the system is provided by the nonlinear function $\boldsymbol{f}(\boldsymbol{x}, t)$. If the system obeys the *existence and uniqueness* hypotheses, Eq. (2.1) has one and only one solution $\boldsymbol{x}(t)$[1], sometimes referred to as *flow* $\phi(\boldsymbol{x}_0, t_0; t)$. This property is a necessary first step to treat every problem here discussed. Three important definitions, widely used throughout this work are here stated:

Definition Phase space:
Given the system in Eq. (2.1), phase space is considered as the subset D where the state is defined: $\boldsymbol{x} \in D \subset \mathbb{R}^n$.

Definition Periodic solution:
$\psi(t)$ is defined as a periodic solution if it satisfies Eq. (2.1) and if $\exists\, T \in \mathbb{R} : \psi(t+T) = \psi(t)$, $\forall\, t \in I \subset \mathbb{R}$

Definition Invariant manifold:
An invariant manifold is defined as an invariant set[2] of points, shaping a continuous and smooth object,

[1] According to [33] one should demand how $\boldsymbol{f}(\boldsymbol{x}, t)$ is continuous in the definition set of $\boldsymbol{x}$ and t, namely $A = [t_0 - \bar{a},\, t_0 + \bar{a}] \times \{\boldsymbol{x} : \|\boldsymbol{x} - \boldsymbol{x}_0\| \leq \bar{d}\}$ and it is *Lipschitz*-continuous in $\boldsymbol{x}$. Then the theorem follows for $|t - t_0| \leq min\left(\bar{a}, \frac{\bar{d}}{\sup \|\boldsymbol{f}\|}\right)$, with $\bar{a}, \bar{d}$ positive constants.

[2] the set $\boldsymbol{S} \subset \mathbb{R}^n$ is invariant under the flow $\boldsymbol{x}(t) = \phi_t(\boldsymbol{x}_0)$ if $\forall \boldsymbol{x}_0 \in \boldsymbol{S}$, $\boldsymbol{x}(t) \in \boldsymbol{S}$

namely a *differentiable manifold*. Alternatively, an invariant manifold is a manifold which is invariant under the effect of the dynamical flow.

2.1.2. Autonomous vs nonautonomous

A system of differential equations, like the one in Eq. (2.1), is defined as *autonomous* if the nonlinear function $\boldsymbol{f}$ does not explicitly depend on time, namely the mathematical statement of the problem is [33]

$$\dot{\boldsymbol{x}} = \boldsymbol{f}(\boldsymbol{x}), \qquad \boldsymbol{x}(t_0) = \boldsymbol{x}_0 \tag{2.2}$$

consequently, Eq. (2.1) refers to the general *nonautonomous* system. Now, other important definitions are given:

Definition Critical point:
For the general autonomous system outlined in Eq. (2.2), a critical (or equilibrium) point is defined as $\boldsymbol{x}^* \in \mathbb{R}^n : \boldsymbol{f}(\boldsymbol{x}^*) = \boldsymbol{0}$. If, in a neighbourhood of $\boldsymbol{x}^*$, $\lim_{t\to\pm\infty} \boldsymbol{x}(t) = \boldsymbol{x}^*$, the critical point is referred to as positive ($t+ \to \infty$) or negative ($t \to -\infty$) *attractor*. Stability characteristics of the critical point can be easily inferred if the system is linear; if the latter does not hold, drawing any conclusion about the stable nature of this point may become a more difficult task. Generally, critical points are studied for autonomous systems only, since for nonautonomous ones they are hard to obtain.

Definition First integral:
As a straightforward definition, once Eq. (2.2) is given, a *first integral* of the system is defined as $H : \mathbb{R}^n \to \mathbb{R}$ for $\boldsymbol{x} \in D \subset \mathbb{R}^n$ such that $\nabla_{\boldsymbol{x}} H \cdot \dot{\boldsymbol{x}} = 0$, where $(\cdot)$ represents the *scalar product*. For this reason, any first integral can be seen as a constant of motion for autonomous systems.

Three more aspects must be here reported. First of all, an important property holds for autonomous systems, referred to as *translation property* by Verhulst [33]: it states how, if a solution $\phi(t - t_0)$ of the system of Eq. (2.2) exists, then $\phi(t - t_1)$ is a solution of the same problem, with initial condition $\boldsymbol{x}(t_1) = \boldsymbol{x}_0$.
Another important assertion for autonomous systems is that periodic solutions are closed orbits in the phase space, and vice versa; this straightforwardly follows from the existence and uniqueness theorem.
A theorem holds for the existence of invariant manifolds of a critical point: it states how, under certain conditions related to the structure of the problem in Eq. (2.1), the stable and unstable invariant manifolds of the nonlinear problem, referred to as W_s, W_u respectively, are tangent to, equidimensional to and with the same order of smoothness of the stable and unstable eigenspaces of their linearized counterparts[3].

2.1.3. Poincaré map

Named after the nineteenth century mathematician H. Poincaré, they are defined as:

Definition Poincaré map:
It is a mapping of a point $\bar{\boldsymbol{x}} \in V \subset \mathbb{R}^{n-1}$ to the same subspace V, usually referred to as hyperplane or more informally, *cut*. Therefore $P : V \to V$ is the Poincaré map; however, the starting point and the projected one can occupy the same location within the phase space.

By mapping, one literally exits from V; the out-of-V link is performed by the unique flow $\phi(t)$, solution of Eq. (2.1), passing through $\bar{\boldsymbol{x}}$. Although the map for almost every case links two different points of V, the intersection *order*, namely the number of consecutive intersections the map had with V, is a key-element of this report. To cite an example, $P(\bar{\boldsymbol{x}})$ is the first order mapping of $\bar{\boldsymbol{x}}$, while $P(P(\bar{\boldsymbol{x}})) = P^2(\bar{\boldsymbol{x}})$ represents its second one and so forth.
The Poincaré map requires the subset V to be everywhere *transversal* to the flow, namely $\nexists \boldsymbol{x}^* \in V : \boldsymbol{f}(\boldsymbol{x}^*) = 0$ and V is nowhere tangential to the flow itself.
An intrinsic feature of this particular mapping, which is evident from its definition, is that it lowers the dimensionality of the analysed space: indeed, the flow is usually studied in V in order to gain insight on its general characteristics, rather than looking at its behaviour in the whole phase space. For this reason, in autonomous

[3] According to [33], Eq. (2.1) can be written as $\dot{\boldsymbol{x}} = A\boldsymbol{x} + \boldsymbol{g}(\boldsymbol{x})$, with $A\boldsymbol{x}$ following from the linearization of the nonlinear equation, while $\boldsymbol{g}(\boldsymbol{x})$ expressing a sort of nonlinear *rest*. If A ($n \times n$ matrix) has n eigenvalues with non-zero real part and $\boldsymbol{g}(\boldsymbol{x})$ is $k-$ times continuous in a neighbourhood of $\boldsymbol{x}^*$ (critical point), the theorem holds true.

planar problems like the one discussed in this report where $\boldsymbol{x} \in \mathbb{R}^4$ and a first integral $H = H(\boldsymbol{x})$ exists, the whole state of every point defined by the flow in the bidimensional projection of V can be retrieved. It is important to notice how periodic orbits are mapped as single points on V.

2.1.4. State Transition Matrix and Differential Correction

The State Transition Matrix (STM) $\Phi(t_0, t_1)$ linearly approximates how a slight deviation $\delta\boldsymbol{x}_0$ from the state $\boldsymbol{x}_0 \in \mathbb{R}^n$ at $t = t_0$ is mapped as a deviation $\delta\boldsymbol{x}_1$ from the unperturbed solution $\boldsymbol{x}^*(t)$ at $t = t_1$. Hence, the linear relation between the two deviations is expressed by

$$\delta\boldsymbol{x}_1 = \Phi(t_0, t_1)\delta\boldsymbol{x}_0 \tag{2.3}$$

From the generic Eq. (2.1), it follows how the dynamics of the STM is defined by

$$\frac{\mathrm{d}\Phi(t_0, t_1)}{\mathrm{d}t} = A(t)\Phi(t_0, t_1), \qquad \Phi(t_0, t_0) = \mathscr{I}_{n\times n} \tag{2.4}$$

where $A(t) = D_{\boldsymbol{x}}\boldsymbol{f}(\boldsymbol{x}, t)|_{\boldsymbol{x}=\boldsymbol{x}^*(t)}$ (namely the Jacobian of $\boldsymbol{f}(\boldsymbol{x}, t)$ evaluated along $\boldsymbol{x}^*(t)$) while $\mathscr{I}_{n\times n}$ is the $n \times n$ identity matrix. From Eq. (2.4) it can be obtained $\delta\dot{\boldsymbol{x}} = A(t)\delta\boldsymbol{x}$.
If Eq. (2.1) allows for a $T-$periodic solution $\phi(t)$, then $\Phi(t_0, T)$ is referred to as *Monodromy* matrix. The STM has some other important properties, namely [33]

$$\Phi(t_1, t_2) = \Phi(t_2, t_1)^{-1}, \qquad \Phi(t_0, t_2) = \Phi(t_1, t_2)\Phi(t_0, t_1) \tag{2.5}$$

In the framework of this research, the STM has a twofold usage: it is employed for the computation of the initial condition of the simple periodic orbits discussed in Section 2.2.1, as shown by Howell [12], and for the optimization of a trajectory, as explained in Section 2.3. Although for different purposes, the STM is used in both cases in an identical way, namely within a Differential Correction scheme.
In a typical Differential Correction, by propagating an initial state $\boldsymbol{x}_0$ up to the final time $t = t_1$, a final state $\boldsymbol{x}_f = \boldsymbol{x}(t_1)$ is obtained. If a *desired* final state $\boldsymbol{x}_d$ is sought, corresponding to a shift from the reference one $\delta\boldsymbol{x}_1 = \boldsymbol{x}_d - \boldsymbol{x}_f$, an initial deviation can be added to $\boldsymbol{x}_0$, which helps in reaching $\boldsymbol{x}_d$. By inverting Eq. (2.3) one can retrieve this deviation as $\delta\boldsymbol{x}_0 = \Phi^{-1}(t_0, t_1)\delta\boldsymbol{x}_1$. The new initial state is propagated and the whole procedure iterated, if needed: this follows from the approximated nature of Eq. (2.3).
The Differential Corrector largely depends on three elements: the degree of nonlinearity of the problem, the distance of the first *guess* $\boldsymbol{x}_0$ from the actual $\bar{\boldsymbol{x}}_0$ which, once propagated for the required time gives exactly $\boldsymbol{x}_d$, and the size of $[t_0, t_1]$.

2.2. Dynamical model

In this section, the main elements of the dynamical models used for this work are discussed. The latter are reported from the easiest to the theoretically most complex one: starting from a restricted case of the three-body model in Section 2.2.1, the section moves forward to highlight the main characteristics of a four-body model in Section 2.2.2. Concluding, in Section 2.2.3 the mathematical concepts of the Levi Civita regularization scheme are applied to the first described dynamical model.

2.2.1. CR3BP

The Circular Restricted Three-Body Problem (CR3BP) is a special case of the Three-Body Problem which defines in its generality the mutual gravitational interactions of a system of three bodies P_1, P_2 and P_3. Two assumptions are stated before deriving the equations of motion, which justify the definition of Restricted and Circular. These are briefly stated below:

1. m_3, namely the mass of the third body P_3, is infinitesimal when compared to m_1 and m_2, masses of P_1 and P_2, often referred together as *primaries* or singularly as *primary* and *secondary*, respectively.

2. Following from the previous assumption, the motion of the two massive bodies is considered planar and circular about their common centre of mass. In the case the third body has its motion constrained to the same plane, the CR3BP takes the further adjective of Planar.

Before continuing with the mathematical definition of the dynamical model, two different reference frames are here mentioned, namely the *inertial* and *synodic* one.

The former is defined as a reference frame where the first principle of dynamics holds true, namely a point with a total null force is *seen* from the frame in its condition of steadiness or constant speed; conversely, the latter is defined as when this does not happen.
Besides the general description, throughout this work as well as in the majority of the existing literature, a *pseudo*-inertial frame is implicitly used to ease the treatment of data. A clear example rises when employing the centre of the Earth as origin of the frame, although the Earth itself moves under other forces. Hereafter, the *pseudo* adjective is discarded to facilitate the reading, although this simplification should always be assumed as implicit.
Assuming the two reference frames as coplanar and with a common origin, they are separated by a central angle θ on the xy-plane. The following transformation holds:

$$\boldsymbol{x}_{syn} = \left[\begin{array}{c|c} A & 0_{2\times 2} \\ \hline A_\theta & A \end{array}\right] \boldsymbol{x}_{in} \tag{2.6}$$

with the states $\boldsymbol{x}_{syn}, \boldsymbol{x}_{in} \in \mathbb{R}^4$, $0_{2\times 2}$ the 2×2 zero-matrix and

$$A = \begin{bmatrix} \cos(\theta) & -\sin(\theta) \\ \sin(\theta) & \cos(\theta) \end{bmatrix} \quad \text{and} \quad A_\theta = \frac{\mathrm{d}A}{\mathrm{d}\theta} \tag{2.7}$$

where θ is taken anticlockwise from the positive x-axis of the inertial reference frame. Before dealing with the involved mathematics, a sketch comparing the inertial and synodic frame is reported in Fig. 2.1.

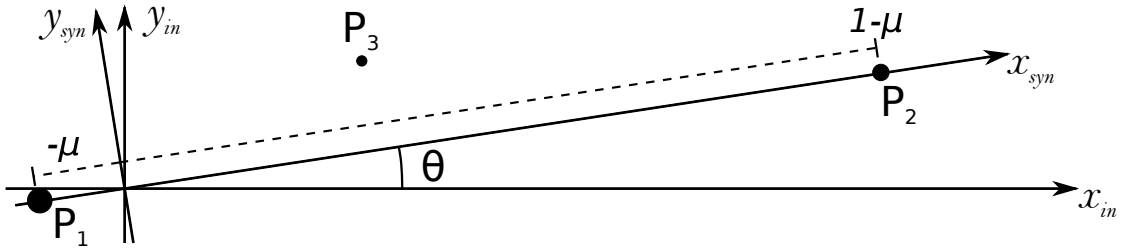

Figure 2.1: Representation of the P_1P_2-barycentric reference frame, in both the inertial and synodic form. In this exemplary case $\mu = 0.1$.

Equations of motion

The equations of motion, expressing the dynamical model, are obtained as a specific case of the three body problem. The lengthy derivation is here not reported. Since the whole work described in this report has been performed with the planar assumption of the dynamics, thanks to severe simplification on the data handling, the state is hereafter considered bidimensional.
It is custom to express every involved quantity in its dimensionless version: this gives several advantages in the comprehension of the data and in the computation of the associated trajectories, while at the same time extending the applicability of the singular case to a multitude of similar ones. Equations, in the synodic xy-frame, centered on the barycenter of the two primaries, are described by [28]

$$\begin{cases} \ddot{x} = 2\dot{y} + \dfrac{\partial U_3}{\partial x} \\ \ddot{y} = -2\dot{x} + \dfrac{\partial U_3}{\partial y} \end{cases} \quad \text{where:} \quad U_3(x,y) = \frac{1}{2}(x^2+y^2) + \frac{1-\mu}{r_1} + \frac{\mu}{r_2} + \frac{1}{2}\mu(1-\mu) \tag{2.8}$$

with the mass parameter $\mu = m_2/(m_1+m_2)$, $r_1 = \sqrt{(x+\mu)^2+y^2}$ and $r_2 = \sqrt{(x+\mu-1)^2+y^2}$ representing the distances of m_3 from the two primaries, located at $(x, y) = (-\mu, 0)$ and $(x, y) = (1-\mu, 0)$, respectively. The function $U_3(x, y)$ is referred to as *effective potential*: it describes a non-central and *conservative* scalar field.
Quantities are transformed into their dimensionless versions by three problem-depending constants, namely DU, VU, and TU, unit of distance, velocity and time respectively. The latter act as divisors for every time-, distance- and velocity-like quantity. In particular, once DU is obtained from the geometry of the problem (usually taken as the average distance between the primaries), the other two follows as

$$TU = \sqrt{\frac{DU^3}{G(m_1+m_2)}} \quad \text{and} \quad VU = \frac{DU}{TU} \tag{2.9}$$

where G is the universal gravitational constant. From Eq. (2.9), TU can be conceived as the inverse of the orbital mean motion for a massless spacecraft around a body with mass $m = m_1 + m_2$.
As it is discussed in Section 2.1.2, the system of equations is autonomous: it allows the existence of one and one only first integral, called *Jacobi's integral*, defined as

$$J(x, y, \dot{x}, \dot{y}) = 2U_3(x, y) - (\dot{x}^2 + \dot{y}^2) \tag{2.10}$$

The projection of the 4-dimensional space defined by

$$\mathscr{J}(\bar{C}) = \{(x, y, \dot{x}, \dot{y}) \in \mathbb{R}^4 : J(x, y, \dot{x}, \dot{y}) = \bar{C}\} \tag{2.11}$$

on the xy-plane is called Hill's region, as depicted in Fig. 2.2. There is an intrinsic difference between the constant $\bar{C}$ and the projection of the Hill's region on the phase space $\mathscr{J}(\bar{C})$, although often confused in literature: the former represents a constant, while the latter is a subset of the phase space for a certain value of the constant.
Throughout this report, the angular momentum h_2 and the energy H_2 with respect to the Moon are largely employed. Their derivation is reported in Appendix A, while their definition is [29]

$$h_2(\boldsymbol{x}) = (x + \mu - 1)(\dot{y} + x + \mu - 1) - y(\dot{x} - y) \tag{2.12a}$$

$$H_2(\boldsymbol{x}) = \frac{v_2(\boldsymbol{x})^2}{2} - \frac{\mu}{r_2(\boldsymbol{x})} = \frac{(x + \mu - 1 + \dot{y})^2 + (\dot{x} - y)^2}{2} - \frac{\mu}{r_2(\boldsymbol{x})} \tag{2.12b}$$

Referring to Section 2.1.4, the Jacobian of the system of Eq. (2.8) is given by

$$A(t) = \begin{bmatrix} 0 & 0 & 1 & 0 \\ 0 & 0 & 0 & 1 \\ \dfrac{\partial^2 U_3}{\partial x^2} & \dfrac{\partial^2 U_3}{\partial y \partial x} & 0 & 2 \\ \dfrac{\partial^2 U_3}{\partial x \partial y} & \dfrac{\partial^2 U_3}{\partial y^2} & -2 & 0 \end{bmatrix}_{\boldsymbol{x} = \boldsymbol{x}^*(t)} \tag{2.13}$$

It is helpful, for the purpose of this report, to have a geometrical delimiter about the secondary: the Hill's sphere. The latter helps to distinguish the area on the xy-plane where the gravitational pull of the secondary either *largely* (inside the sphere) or *weakly* (outside the sphere) influences the motion of the spacecraft. Its radius is given by [25]

$$R_{Hill} = \sqrt[3]{\frac{\mu}{3(1 - \mu)}} \tag{2.14}$$

Hill's sphere is selected as a suitable boundary thanks to its meaning and derivation[4], although representing an approximation of the real case since the gravitational perturbation of the Earth in a neighbourhood of the Moon is position-depending. In this report the term *sphere* is widely interchanged with circumference (representing Hill's sphere intersection with the synodic xy-plane) in order to maintain the proper nomenclature.

Lagrange points and periodic orbits

Equation 2.8 has five equilibrium points, named *Lagrange* or *Lagrangian* points. From the strict definition, their location can be computed setting the left-hand side of Eq. (2.8) to zero, after having converted it into a

[4] Hill's sphere should not be confused with the Sphere of Influence (SOI). The difference stands either in the formulation and in the meaning. According to [34], the SOI is described as the volume-space centered on a massive body P_1 within which one can consider the motion of the spacecraft as a perturbed two-body problem about P_1. The relative formulation is directly derived from the general N-body equation of motion. However, according to [32], Hill's sphere (to be discerned from Hill's region in Eq. (2.10)) is derived from a stability analysis of spacecraft's orbit about the secondary, directly following from *Hill's equations*, which represents a revised approximated $(1 - \mu \approx 1)$ set of equations about the secondary. The latter are derived from the CR3BP system of Eq. (2.8). For this reasons, the Hill's sphere constitutes a suitable boundary for the case treated in this report. It must be noted how the radius of the SOI is by definition larger than the Hill's sphere one.

four-dimensional system of first-order differential equations, as

$$\begin{cases} \dot{x} = v_x \\ \dot{y} = v_y \\ \dot{v}_x = x + 2v_y - \dfrac{(x+\mu)(1-\mu)}{r_1^3} - \dfrac{\mu(x+\mu-1)}{r_2^3} \\ \dot{v}_y = y - 2v_x - \dfrac{y(1-\mu)}{r_1^3} - \dfrac{\mu y}{r_2^3} \end{cases} \tag{2.15}$$

This leads to $\nabla U_3(x, y) = \mathbf{0}$ for the derivation of these points.
Hence, their location is on the xy-plane even in the 3D-case; three of them, namely L_1, L_2 and L_3, are set on the line connecting the two primaries m_1 and m_2, as depicted in Fig. 2.2 and for this reason are addressed as *collinear* Lagrange points. With the definition of potential given in Eq. (2.8), they have a location so that their associated Jacobi constants are $\bar{C}_{L_1} > \bar{C}_{L_2} > \bar{C}_{L_3} > \bar{C}_{L_4} = \bar{C}_{L_5} = 3$. Their values, for the Earth–Moon case are reported in Table 2.1.

L_i	x_{L_i}	$\bar{C}_{L_i}$
L_1	0.836914718893202	3.200344909832180
L_2	1.155682483478614	3.184164143176462
L_3	-1.003037603428298	3.024162670307643

Table 2.1: Coordinates and associated Jacobi constant values for the collinear Lagrange points.

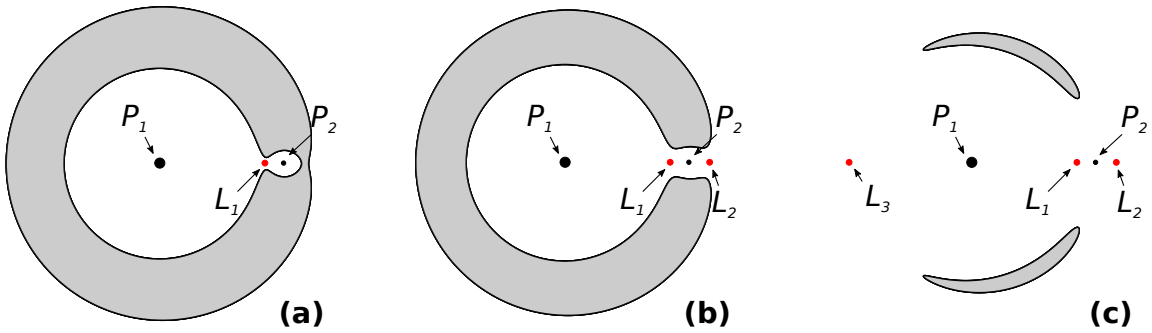

Figure 2.2: Example of the Zero Velocity Curves (grey) for different values of $\bar{C}$. Note how, by decreasing their values, the available space widens. **(a)** $\bar{C}_{L_2} < \bar{C} < \bar{C}_{L_1}$; **(b)** $\bar{C}_{L_3} < \bar{C} < \bar{C}_{L_2}$; **(c)** $\bar{C}_{L_{4,5}} < \bar{C} < \bar{C}_{L_3}$;

The dynamics concerning the collinear Lagrange points and associated periodic orbits have been widely studied in the past (Conley [7], Koon et al. [14], Parker and Anderson [23]). It is interesting, for the sake of completeness, to briefly show the computation of both the simple planar periodic orbits about the collinear Lagrange points and the associated invariant manifold [23]. As a first step, a guessed state along the $x-$axis is given as $\boldsymbol{x}_0 = (x, 0, 0, \dot{y})_0$. This state is *corrected* to meet a final constraint of $\boldsymbol{x}_{T/2} = (x, 0, 0, \dot{y})_{T/2}$ in order to comply with the symmetric requirement of a $T-$periodic orbit [12]. The initial condition, generating a periodic orbit at a fixed $\bar{C}$ is then obtained by iterating the following system

$$\begin{cases} \begin{bmatrix} \delta x \\ \delta \dot{y} \end{bmatrix}_{0,i} = \begin{bmatrix} \phi_{3,1} - \phi_{2,1}\dfrac{\ddot{x}}{\dot{y}}\Big|_{\boldsymbol{x}=\boldsymbol{x}_{T/2,i}} & \phi_{3,4} - \phi_{2,4}\dfrac{\ddot{x}}{\dot{y}}\Big|_{\boldsymbol{x}=\boldsymbol{x}_{T/2,i}} \\ \dfrac{\partial J}{\partial x}\Big|_{\boldsymbol{x}=\boldsymbol{x}_{0,i}} & \dfrac{\partial J}{\partial \dot{y}}\Big|_{\boldsymbol{x}=\boldsymbol{x}_{0,i}} \end{bmatrix}^{-1} \begin{bmatrix} -\dot{x}_{T/2,i} \\ \bar{C} - J(\boldsymbol{x}_{0,i}) \end{bmatrix} \\ \boldsymbol{x}_{0,i+1} = \boldsymbol{x}_{0,i} + [\delta x, 0, 0, \delta \dot{y}]_{0,i}^T \end{cases} \tag{2.16}$$

where $\phi_{j,k}$ is the $(j,k)^{\text{th}}$ element of the STM evaluated at $\boldsymbol{x} = \boldsymbol{x}_{T/2,i}$. The whole procedure is repeated, in agreement with what is discussed in Section 2.1.4. The first equation in the system of Eq. (2.16) is derived in Appendix A and as an example, Fig. 2.3 shows the *Horizontal Lyapunov Orbits* (HLO) about the collinear points for the same value of $\bar{C}$.
After the Differential Corrector has converged and the initial state $\boldsymbol{x}_0$ for the periodic orbit is obtained, the associated invariant manifold is constructed by perturbing and subsequently propagating the state $\boldsymbol{x}_{t_i,p.o.}$ at time t_i along the periodic orbit as

$$\boldsymbol{x}_{t_i,new} = \boldsymbol{x}_{t_i,p.o.} \pm \epsilon \frac{\boldsymbol{v}_i^k}{\|\boldsymbol{v}_i^k\|} \tag{2.17}$$

where $\boldsymbol{x}_{t_i,new}$ is the perturbed state at time t_i, $\boldsymbol{v}_i^k = \Phi(t_0, t_i)\,\boldsymbol{V}^k$ where k stands for either the stable S or unstable U eigenvector $\boldsymbol{V}$ of the monodromy matrix and $\pm$ distinguishes between the *interior* $(-)$ and *exterior* $(+)$ branch. In this report, for the Earth–Moon system, $\epsilon \approx 2.6 \times 10^{-4}$ (in its dimensionless form, corresponding to 100 km) when perturbing the first two components x_{t_i}, y_{t_i}, while $\epsilon \approx 2.6 \times 10^{-4} / \sqrt{\dot{x}_{t_i}^2 + \dot{y}_{t_i}^2}$ for the remaining velocity components $\dot{x}_{t_i}$, $\dot{y}_{t_i}$ of $\boldsymbol{x}_{t_i,p.o.}$. Although ϵ has a rather high value in this report, the choice is here motivated by a preference of a fast (rather than precise) computation of the invariant manifolds, due to the high amount of generated orbits, in agreement with Parker and Anderson [23]. Indeed, smaller perturbations can approximate better the invariant manifolds, even though they require more time to depart from the orbit. For every perturbed state, the orbits are accordingly propagated (backward in time if $k = S$, forward otherwise) in order to obtain the associated invariant manifold. An example of the invariant manifolds for an L_2 HLO is depicted in Figs. 2.4a and 2.4b.

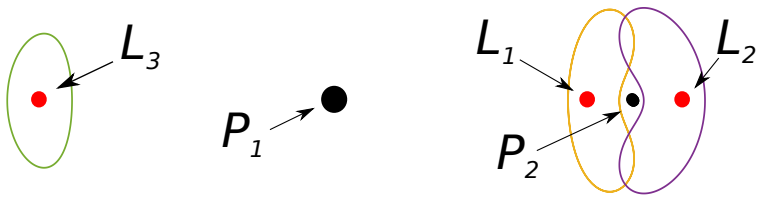

Figure 2.3: Example of three HLOs' associated with the collinear Lagrange points, for $\bar{C} \approx 3.0115$.

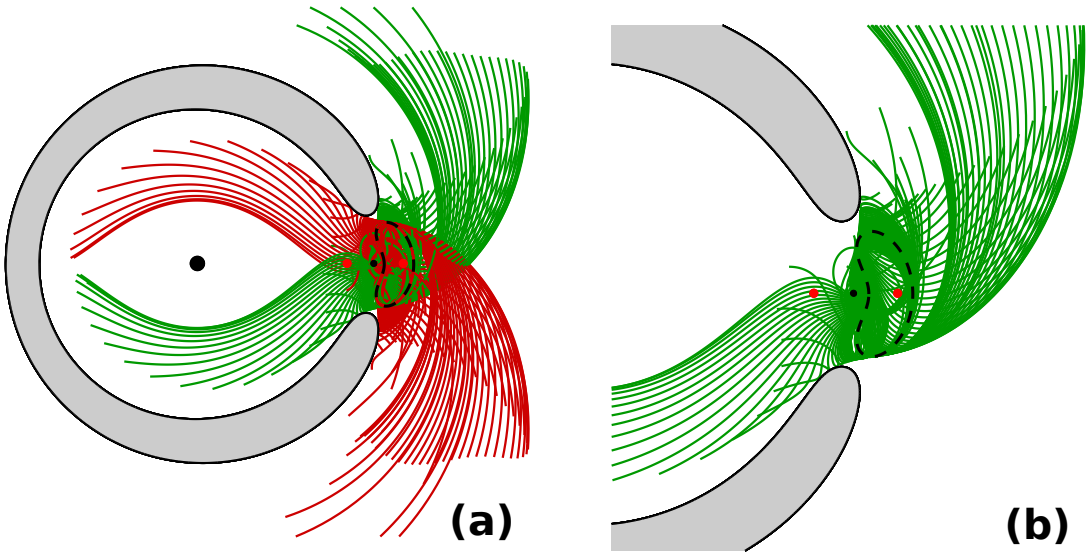

Figure 2.4: **(a)** Stable (green) and unstable (red) invariant manifold emanating from the HLO at L_2 (dashed black line) for $\bar{C} \approx 3.0514$. Earth and Moon as black dots, Lagrange points as red dots. ZVC in grey; **(b)** magnification of the stable manifold of (a) in proximity of the Moon. Manifold propagated for $t \approx 55$ terrestrial days.

2.2.2. BR4BP

The Bi-circular Restricted Four-Body Problem consists in an extension of the former CR3BP, whereas the presence of a fourth body P_S is included. The latter has a non-negligible mass m_S, and its orbit is assumed to be coplanar with the mutual motion of the other two massive bodies, previously indicated as P_1, P_2, and restricted to be circular with respect to their barycentre in the synodic reference frame. Although the relative dynamical model lacks in coherence, not complying with Newton's laws, it can give a deep insight in the involved dynamics.
The BR4BP represents a possible solution among different simplified four-body dynamical architectures: however, for the main purpose of this report, it has been chosen since best fitting with the studied case, namely the Sun–Earth–Moon system, as substantially confirmed by an extensive literature (Qi and Xu [24], Simó et al. [27]). The general equations in the P_1P_2-synodic frame are defined by [29]

$$\begin{cases} \ddot{x} = 2\dot{y} + \dfrac{\partial U_4}{\partial x} \\ \ddot{y} = -2\dot{x} + \dfrac{\partial U_4}{\partial y} \end{cases} \quad \text{where:} \quad U_4(x, y, \theta_s) = U_3(x, y) + \frac{\mu_S}{r_s(\theta_s)} - \frac{\mu_S}{a_S^2}\left(x\cos(\theta_S) + y\sin(\theta_S)\right) \tag{2.18}$$

where $\mu_S = m_S/(m_1 + m_2)$, a_S is the magnitude of the radius of P_S' circular orbit around the barycentre of the P_1P_2 subsystem, ω_S is the angular velocity of P_S' circular motion in the synodic frame, the *time-wise* variable $\theta_S = \theta_{S0} + \omega_S(t - t_0)$ is the angular distance in the synodic frame between the positive $x-$axis and the position vector of P_S, and U_4 represents the new time-dependent potential function. The introduction of a new body has switched the problem from an autonomous to a nonautonomous one, although $2\pi/\omega_S$-periodic. A visual overview in the synodic frame is given by Fig. 2.5. Both the BR4BP and the CR3BP presents few symmetries which ease computational effort. Throughout this thesis work, the following one is extensively used [20]

$$[x, y, \dot{x}, \dot{y}, t] \quad \longrightarrow \quad [x, -y, -\dot{x}, \dot{y}, -t] \tag{2.19}$$

However, when using this symmetry for the BR4BP, the value of θ_{S0} must be switched in sign, accordingly with the time-dependency of Eq. (2.18). In Appendix A the proof of the symmetry is outlined. Information concerning Earth's orbit about the Sun and Moon's orbit about Earth are briefly reported in Table 2.2.

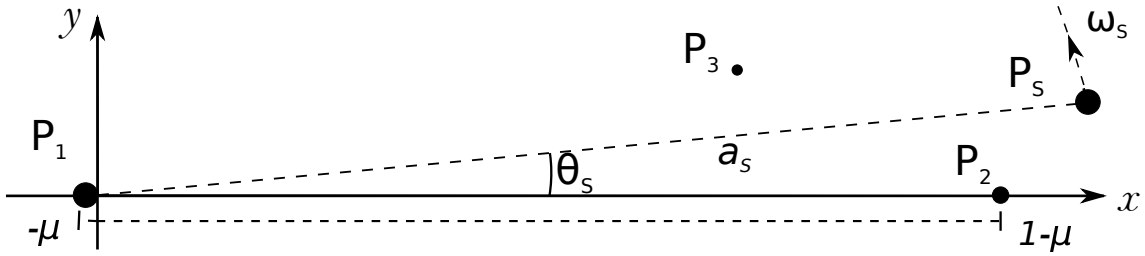

Figure 2.5: Geometry of the BR4BP in the synodic P_1P_2-barycentric reference frame. a_s not in scale.

Body	a [km]	T [days]	e [-]	i [deg]
Earth	1.496×10^8	365.256	0.017	-
Moon	3.844×10^5	27.452	0.055	5.15

Table 2.2: Main orbital data for Earth and the Moon, with respect to the Sun and Earth respectively. Table shows their average semi-major axis, periods, eccentricities and inclinations (with respect to Earth's orbit about the Sun), respectively from left to right. Mind how Earth's inclination about the Sun is null since the ecliptic is taken as reference plane. A single day refer to one terrestrial day, namely 86400 s (taken from Acton [1], Lissauer and de Pater [18]).

2.2.3. Levi Civita regularization

A regularization of the problem is usually performed to avoid a lack in precision in the computation of the state, especially in those areas of the phase space where a singularity of the equations exists. Levi Civita first proposed a local regularization scheme [17] for the synodic CR3BP. In this work, his scheme is employed to accurately propagate orbits starting from or passing really close to the secondary (the Moon in the Earth–Moon

system): without this shrewdness, Eq. (2.8) would lead to a really imprecise computation due to the singularity at $(x, y) = (1-\mu, 0)$. The thorough derivation, in a less old-fashioned manner, is extensively reported in Szebehely [28]. The regularization changes the shape of the equations of the problem, consequently varying the obtained state itself. In this report, $\boldsymbol{u} = (u_1, u_2, u_3, u_4)$ is referred to as the state in regularized coordinates. The transformation between Cartesian synodic and regularized coordinates, $(x, y, \dot{x}, \dot{y}) \Longleftrightarrow (u_1, u_2, u_3, u_4)$ is given as [16, 21]

$$\text{Car2LC:} \quad \begin{cases} \text{if } x < x_0 & \text{if } x \geq x_0 \\ u_2 = \sqrt{\dfrac{r_0 - (x - x_0)}{2}} & u_1 = \sqrt{\dfrac{r_0 - (x - x_0)}{2}} \\ u_1 = \dfrac{y}{2u_2} & u_2 = \dfrac{y}{2u_1} \end{cases} \quad \text{,while:} \quad \begin{bmatrix} u_3 \\ u_4 \end{bmatrix} = \frac{1}{2r_0} \begin{bmatrix} u_1 & u_2 \\ -u_2 & u_1 \end{bmatrix} \begin{bmatrix} \dot{x} \\ \dot{y} \end{bmatrix} \tag{2.20a}$$

$$\text{LC2Car}^4\text{:} \quad \begin{bmatrix} x - x_0 \\ y \end{bmatrix} = \begin{bmatrix} u_1 & -u_2 \\ u_2 & u_1 \end{bmatrix} \begin{bmatrix} u_1 \\ u_2 \end{bmatrix} \quad \text{,while:} \quad \begin{cases} \dot{x} = 2\dfrac{(u_1 u_3 - u_2 u_4)}{u_1^2 + u_2^2} \\ \dot{y} = 2\dfrac{(u_1 u_4 + u_2 u_3)}{u_1^2 + u_2^2} \end{cases} \tag{2.20b}$$

where x_0 is the abscissa of the *regularized* body, while r_0 is the distance of the spacecraft from it. Equations of motion in regularized coordinates are

$$\begin{cases} u_1' = u_3 \\ u_2' = u_4 \\ u_3' = \dfrac{1}{4}\left[(a_u + b_u)\, u_1 + c_u u_2\right] \\ u_4' = \dfrac{1}{4}\left[(a_u - b_u)\, u_2 + c_u u_1\right] \end{cases} \tag{2.21}$$

The independent variable has changed from t to s, according to the regularization $\mathrm{d}t = r_0 \mathrm{d}s$. Consequently, the derivative of the state with respect to s is indicated with $(')$. a_u, b_u, c_u are defined as

$$a_u = \frac{2(1-\mu)}{\sqrt{\left(u_1^2 - u_2^2 + 1\right)^2 + 4u_1^2 u_2^2}} - \bar{C} + \left(u_1^2 - u_2^2 + 1 - \mu\right)^2 + 4u_1^2 u_2^2 + \mu(1-\mu) \tag{2.22a}$$

$$b_u = 8\left(u_2 u_3 + u_1 u_4\right) + 2\left(u_1^2 + u_2^2\right)\left(u_1^2 - u_2^2 + 1 - \mu\right) - \frac{2(1-\mu)\left(u_1^2 - u_2^2 + 1\right)\left(u_1^2 + u_2^2\right)}{\left[\left(u_1^2 - u_2^2 + 1\right)^2 + 4u_1^2 u_2^2\right]^{\frac{2}{3}}} \tag{2.22b}$$

$$c_u = 4u_1 u_2\left(u_1^2 + u_2^2\right) - 8\left(u_1 u_3 - u_2 u_4\right) - \frac{4(1-\mu)u_1 u_2\left(u_1^2 + u_2^2\right)}{\left[\left(u_1^2 - u_2^2 + 1\right)^2 + 4u_1^2 u_2^2\right]^{\frac{2}{3}}} \tag{2.22c}$$

The Jacobi constant $\bar{C}$ appears in Eq. (2.22a), while the singular term r_0 is absent.
One particular case which is severely employed throughout this report is when orbits *start* from the secondary at $(x, y) = (1-\mu, 0)$, where the local regularization reaches its major usefulness. According to [21], the initial condition starting from the centre of the secondary is

$$\begin{bmatrix} u_1 \\ u_2 \\ u_3 \\ u_4 \end{bmatrix} = \begin{bmatrix} 0 \\ 0 \\ \sqrt{\dfrac{\mu}{2}}\cos\theta_c \\ \sqrt{\dfrac{\mu}{2}}\sin\theta_c \end{bmatrix} \tag{2.23}$$

where θ_C represents a parametrizing collision angle. In Appendix A the derivation of Eq. (2.23) is shown.
Levi Civita regularization for the CR3BP is one possible solution to avoid singularities of the problem; nevertheless, a local regularization scheme can be extended to handle global singularities (see Castilho and Vidal [6]). To the best of author's knowledge no Levi Civita regularization scheme is available for the BR4BP.

[4] Car2LC stands for the transformation from Cartesian to Levi Civita. Vice versa holds for LC2Car.

2.3. Optimization

In this section, the problem of optimization for spacecraft trajectories is briefly analysed from a theoretical perspective. The main aspects employed throughout this report do not cover the whole realm of optimization technique available in the existing literature: for this reason, only the necessary information is here described. In Section 2.3.1 the most general aspects regarding optimization are presented, followed by Section 2.3.2 where the techniques employed in this work are described.

2.3.1. Overview

In this report the generic optimization problem can be defined through its mathematical statement: the state variable $\boldsymbol{y} \in D \subset \mathbb{R}^n$ represents the *finite* set of parameters, whose optimization aims at either minimizing or maximizing the *cost function* $F : D \to \mathbb{R}$. Every maximization problem can be regarded as a minimization one, by changing the sign of the cost function. The mathematical statement of the generic optimization is summarized as follows:

$$\begin{aligned} &\text{Find } \boldsymbol{y}, \text{ such that :} \\ &F(\boldsymbol{y}) \text{ is minimized} \\ &\text{subject to :} \\ &\boldsymbol{c}(\boldsymbol{y}) \leq 0, \quad \boldsymbol{c}_{eq}(\boldsymbol{y}) = 0, \end{aligned} \tag{2.24}$$

where $\boldsymbol{c}_{eq} : \mathbb{R}^n \to \mathbb{R}^m$ with $m \in \mathbb{N} : m \leq n$ (when linearly independent) and $\boldsymbol{c} : \mathbb{R}^n \to \mathbb{R}^q$ with $q \in \mathbb{N}$, are referred to as nonlinear equality and inequality constraints, respectively. It is implicit throughout this report to include the linear constraints within the nonlinear ones, for every problem statement, since the former can be thought as a special case of the latter [2]. Every optimization problem needs a first guess $\boldsymbol{y}_0$ to start with the computation. The distance of the guess to the real optimum represents a cardinal element for a fast and precise convergence to the optimum $\boldsymbol{y}_{opt}$.

2.3.2. Strategies

The problem highlighted in Eq. (2.24) is solved in this report with two different strategies, although the structure of the overall algorithm can be described with a single flow, as it is shown in Fig. 2.6.

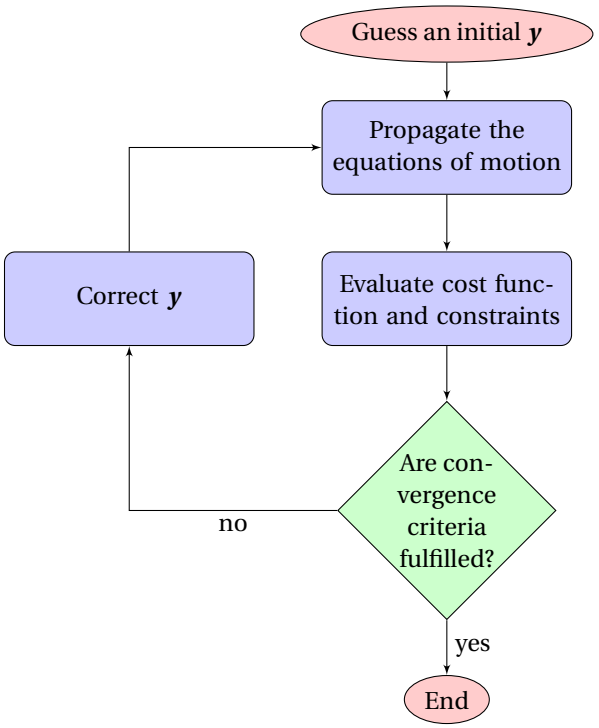

Figure 2.6: Architecture of the algorithm used for optimization

Due to the nonlinear nature of the problem, part of the algorithm is iterated until the convergence criteria are satisfied. The flow can be compared to the single-shooting technique, whereas the *shooting* is embodied by the propagation block. Although the overall algorithm is unique in this report, two different strategies are applied to account for the convergence criteria and the correction of $\boldsymbol{y}$, whose main difference relies on the underlying mathematics.

STM and Differential Corrector: As for the first simpler case, the strategy employing the STM with the Differential Corrector is used for the state correction, whose architecture is delineated in Section 2.1.4. This method has been selected due to its simplicity and fast computational implementation. In this case, having as generic solution $\boldsymbol{x}(t)$, the variable $\boldsymbol{y}$ is fully contained within the initial state $\boldsymbol{x}(t_0)$. The convergence in this report is based on $\left|F\left(\boldsymbol{y}\right)\right|$.

fmincon: MATLAB `fmincon` routine is used, aiming at finding the optimal $\boldsymbol{y}_{opt}$ minimizing the cost function $F(\boldsymbol{y})$, potentially counting on different algorithms (Interior-Point [11] and Sequential Quadratic Programming [2] among others). The problem statement needs to be translated in order to be correctly processed, according to the software standard [19]. The gradients of the cost function as well as the constraints can be given as input to the routine in order to ease the computation and improve the result. Differently from the previous approach, the variable $\boldsymbol{y}$ may not be contained within the initial state $\boldsymbol{x}(t_0)$. The convergence step is performed within the routine.

3

Simple M2M transfer in the Earth–Moon CR3BP

In this chapter Moon-to-Moon (M2M) transfers are addressed, using the planar Earth–Moon CR3BP. The model consists of a severe approximation of the real case: as stated in Section 2.2.1 the two primaries are considered as points, rotating in a circular uniform motion about their barycentre. However, as highlighted in Table 2.2, the assumptions on the dynamics of the involved bodies are rather minimal, due to the low eccentricity of lunar orbit about the Earth . Being a preliminary study for a basic understanding of the involved dynamics, no perturbation (solar radiation pressure, spherical harmonics and so forth) is here taken into account rather then the intrinsic third body one. This approximation is either reasonable, in order to outline the main aspects of the motion and ease the treatment of the chaotic problem, and consistent with a severe amount of examples in literature. The same philosophy is extended to the whole report.
The chapter is divided as follows: in Section 3.1 the author explains the concepts behind an M2M transfer and how the different tools are employed. In Section 3.2 the single ballistic M2M transfer is derived, analysing its main features. Considerations pertaining the invariant manifolds of simple periodic orbits about the Earth–Moon collinear Lagrangian points and lunar collision orbits are discussed in Section 3.3, before the concluding assessments in Section 3.4.

3.1. Approach

The backbone of this chapter, necessary to understand how the M2M transfer are obtained and further analysed, is discussed in this section. First, a formal definition of what in this report is considered as a Moon-to-Moon transfer is here outlined, in both a qualitative and quantitative way.

Definition Moon-to-Moon transfer:
A Moon-to-Moon transfer, shortly addressed as M2M transfer, is defined as every transfer starting and culminating within the lunar Hill's sphere but out from the lunar surface, whose maximum distance from the Moon exceeds the lunar Hill's sphere radius.

Avoiding the Moon surface is a prerequisite for every trajectory; however, the selection of lunar Hill's sphere as implicit boundary to discern what is influenced by the Moon from what is not, can lead to different debates. Nevertheless, following from Section 2.2.1, this choice represents a good quantitative element to catalogue a transfer as an M2M, without any complication.
The procedure to obtain an M2M transfer can be divided into three steps: in Section 3.1.1 lunar *ejection* orbits (a particular case of collision ones) are propagated from the centre of the Moon for different collision angles θ_C but with the same constant $\bar{C}$, according to Levi Civita regularized equations highlighted in Section 2.2.3. Right after the first propagation step, the dynamical scheme is switched from Levi Civita to Cartesian, following the dynamics of the CR3BP. Considerations pertaining the latter issue are addressed in Section 3.1.2. Concluding, in Section 3.1.3, in order to study four-dimensional trajectories within the phase space, the behaviour and main characteristics of the collision orbits are analysed on case-depending Poincaré cuts.

3.1.1. Lunar ejection orbits

Ejection orbits are propagated from the centre of the Moon, therefore the Levi Civita local regularization scheme is employed, in order to avoid the singularity. The initial condition on the four-dimensional state is given in Eq. (2.23).
An example of an ejection orbit is shown in Fig. 3.1.

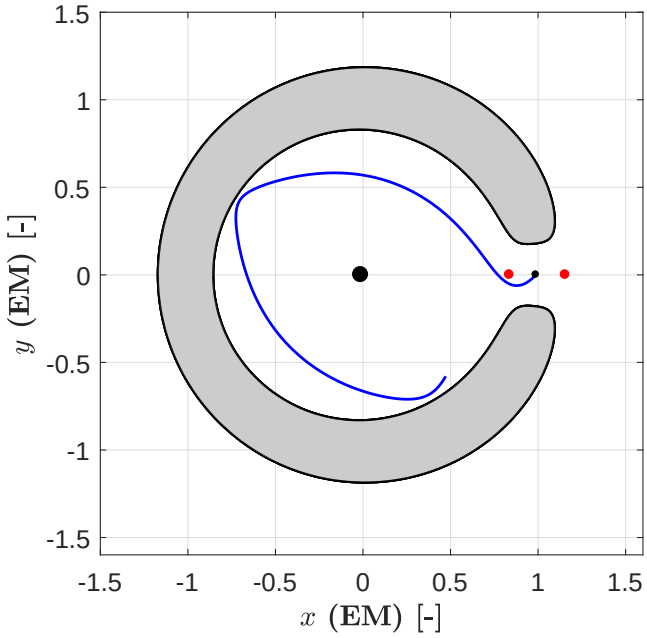

Figure 3.1: Example of a lunar ejection orbit (blue) for $\bar{C} = 3.1$ and $\theta_C = 5\pi/8$. Zero Velocity Curve outlined in grey. Earth and Moon depicted as black dots at $(x, y) = (-\mu, 0)$ and $(x, y) = (1-\mu, 0)$ respectively. Lagrange points L_1 and L_2 in red.

In particular, numerical results have shown a linear correlation between the collision angle θ_C and the physical synodic ejection angle at the Moon θ_E, defined as the departure angle from the Moon with respect to the positive synodic $x-$axis. This relation cannot be determined at the very start of the ejection trajectory from the Cartesian state, due to the singularity; in Fig. 3.2a, this result is numerically shown, while in Fig. 3.2b an example of ejection trajectories is depicted in a magnification about the Moon.

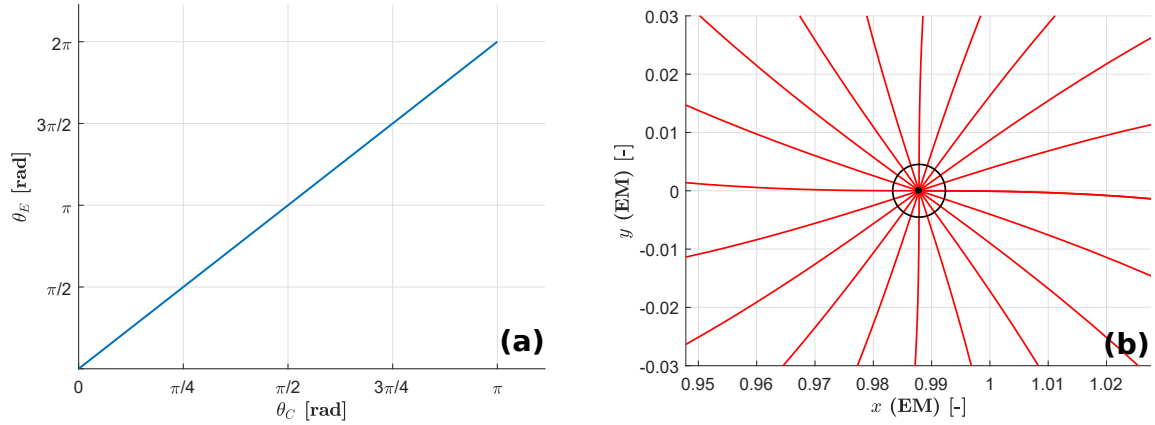

Figure 3.2: **(a)** Linear correlation between collision angle θ_C and ejection angle θ_E; **(b)** Example of lunar ejection orbits (red) for different initial collision angles θ_C at $\bar{C} = 3.1$. Moon represented by the black circle, while its center being the black dot at $(x, y) = (1-\mu, 0)$.

It is clear how $\theta_E = 2\theta_C$: for this reason, the case $\theta_C \in [0, \pi)$ is employed hereafter. It is here evident the usefulness of using collision orbits: having a fixed value of $\bar{C}$, one can analyse the whole set of collision orbits by just varying the collision angle θ_C.

3.1.2. Propagation scheme

Few key-aspects discerning the two dynamical systems, namely Cartesian and regularized Levi Civita are here highlighted: the latter, from Eq. (2.21), is computationally slower to handle and slightly less precise with respect to the former, as evident in Eq. (2.8). The last assessment can be inferred from the results of Fig. 3.3, showing for a set of random initial conditions, the main differences between the two propagation schemes: in Figs. 3.3a and 3.3b the final error in the computation of $\bar{C}$ is reported, for propagations based on Levi Civita and Cartesian scheme respectively. In Fig. 3.3c computational time is compared. Orbits are propagated with identical propagation characteristics (absolute and relative tolerances, events and so forth) and for an identical final time.

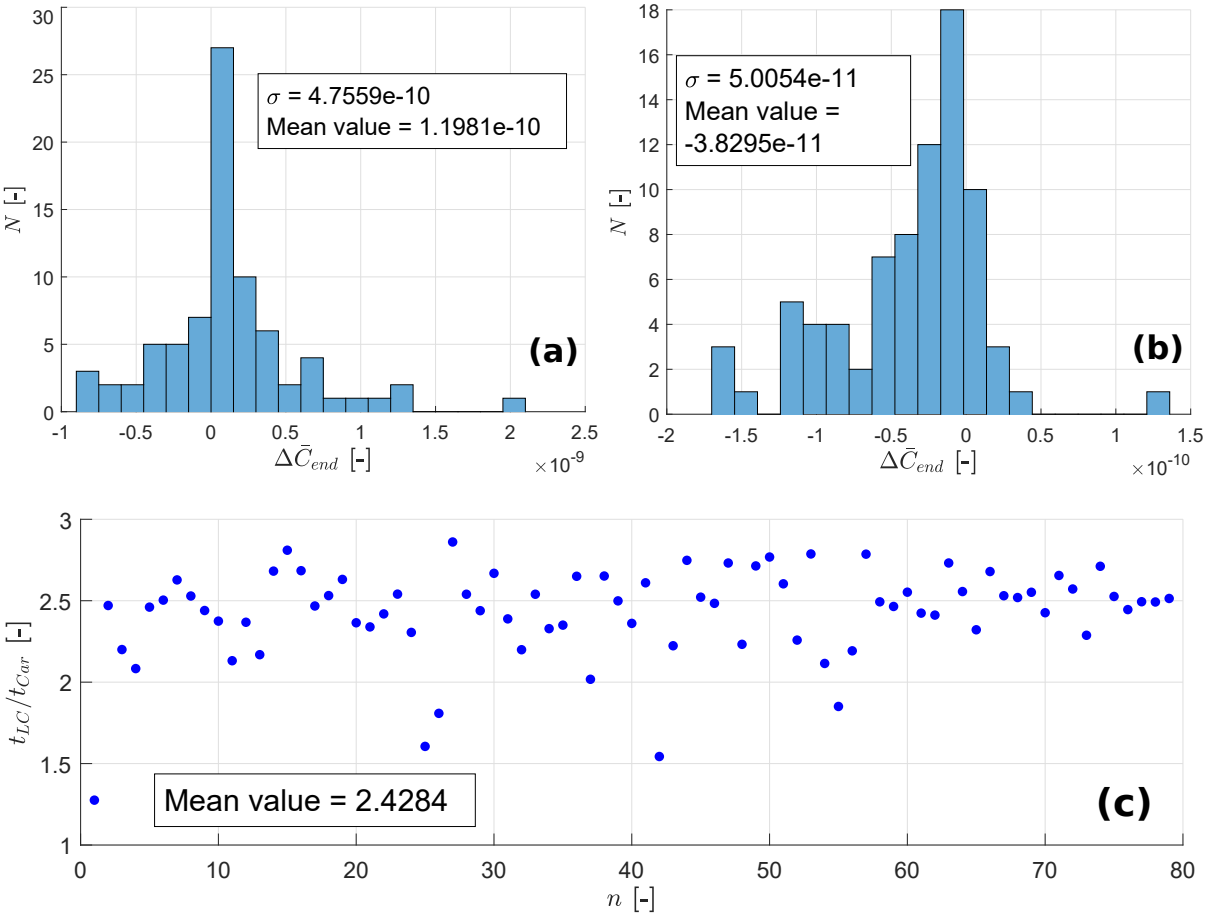

Figure 3.3: 79 computed orbits with random initial conditions. Difference between final and initial Jacobi constant $\bar{C}$ vs. frequencies N for **(a)** Levi Civita and **(b)** Cartesian scheme; **(c)** computational speedup: Levi Civita divided by Cartesian. The integration time is set at $t \approx 434$ terrestrial days.

Due the random search, certain initial conditions may lead to an Earth close passage, which deeply slows the Levi Civita numerical propagation.

Due to a higher computational time and the need to compare the solutions in this chapter with the results of Chapter 5, where no Levi Civita regularization is implemented as pointed out in Section 2.2.2, the latter propagation scheme is employed whereas the state is located in a neighbourhood of the Moon only. For the sake of an easier understanding and implementation, this area is selected as a *disk* centered at $\boldsymbol{x}_{Moon} = (x, y)_{Moon} = (1-\mu, 0)$. The problem translates in finding a proper radius l for this region, so that:

$$\begin{cases} \text{for } \|\boldsymbol{x} - \boldsymbol{x}_{Moon}\| \leq l & \longrightarrow \quad \text{Levi Civita scheme} \\ \text{for } \|\boldsymbol{x} - \boldsymbol{x}_{Moon}\| > l & \longrightarrow \quad \text{Cartesian scheme} \end{cases} \tag{3.1}$$

The choice criteria is based on a combination between a higher precision for the final result and a lower computational time; for what concerns the latter, following the previous analysis, one should conclude how

the sooner one switches from Levi Civita to Cartesian propagation scheme, *the better* it is, since the former is proved to be slower than the latter.
For the former, a different analysis is performed. In order to properly define l in Eq. (3.1), different $l = nR_{Moon}$, with $n \in \mathbb{N}^+$ are used: final precision, in terms of magnitude of the Jacobi integral $\bar{C}$ with respect to the starting one is again used as a discriminating quantity. Results are shown for different l in Fig. 3.4

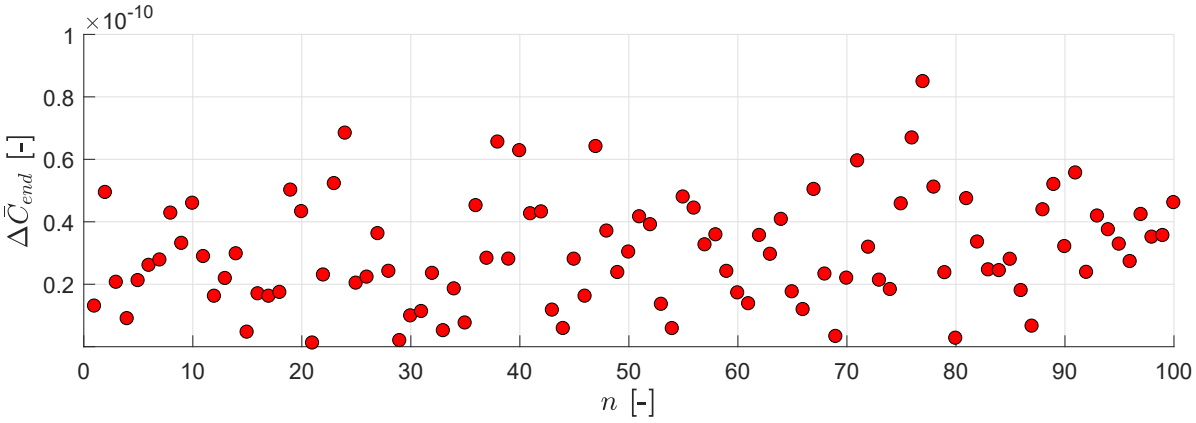

Figure 3.4: The same initial condition of one lunar ejection orbit is here propagated for $t \approx 218$ days, using different $n = \{1, 2, \ldots, 100\}$ as number of lunar radii for switching the propagation scheme from Levi Civita to Cartesian. Precision of the algorithm, in the shape of Jacobi constant $\bar{C}$ difference between the end and start of the trajectory is reported in the y-axis.

Due to the lack of correlation between the final error in the Jacobi constant $\Delta\bar{C}_{end}$ and the number of lunar radii n, in order to have a more-*reasonable* boundary, the radius of the Moon has been selected, so that $l = R_{Moon}$ in Eq. (3.1). This also complies with the previous analysis dealing with computational time.
Therefore lunar ejection orbits are propagated with Levi Civita scheme up to the intersection with the lunar surface; however, the piercing can happen in both directions, namely either exiting from or entering the lunar surface.

3.1.3. Ejection orbits and Poincaré cut

As a final step before deepening in the M2M transfers, collision orbits are here briefly analysed. They are studied throughout this work on two different and really simple Poincaré cuts, namely the $x-$ and $y-$axis: the choice of which one should be used is purely case-depending, as understandable throughout this report. Transversality condition (introduced in Section 2.1.3) is carefully ensured in both cases, by demanding $\dot{y} \neq 0$ and $\dot{x} \neq 0$ at the $x-$ and $y-$axis crossing, respectively. By employing the $y-$axis, one fulfils the requirement of avoiding any critical point of the dynamical system on the cut (Lagrange points, see Section 2.2.1), valid $\forall \mu \in \mathbb{R}^+ : \mu \neq 0.5$, which is always the case in this report. However, the same cannot be stated for the $x-$axis: when referring to the former, the formal definition of the Poincaré cut V, once defined $D = \{\mathbb{R} \setminus \{x_{L_1}, x_{L_2}, x_{L_3}\}\}$, becomes $V = \{(x, \dot{x}, \dot{y}) \in D \times \mathbb{R}^2 : J(x, 0, \dot{x}, \dot{y}) = \bar{C}\}$; this is not repeated elsewhere in this report, but taken as assumed when referring to this particular cut. Both cases, namely the x- and y- Poincaré cut are portrayed in Figs. 3.5a and 3.5b respectively, where the intersections of the lunar ejection orbits are evident.
For the planar case, the employment of the Poincaré cut as a line (namely by fixing a coordinate to have a certain value) means that a point on the cut determines one and only one possible trajectory: indeed, by using the $x-$axis Poincaré cut as an example, if an ejection orbit intersects it, the piercing point can be depicted on the $y\dot{y}$-plane and by employing the Jacobi constant $\bar{C}$, the magnitude of the fourth remaining coordinate can be retrieved ($\dot{x}$ in this case). However, an ambiguity on the sign raises, which needs to be solved by constraining the case.
Concluding this section, in order to study collision orbits, lunar *ejection* orbits are propagated with Levi Civita regularization scheme up to the intersection with lunar surface. From that point onwards, trajectories are propagated with the Cartesian propagation scheme as long as they stay out from the Moon, otherwise the scheme is re-switched. The intersections of the orbits with the x- or y-axis Poincaré cut are employed to gain insight in the characteristics of lunar collision orbits.

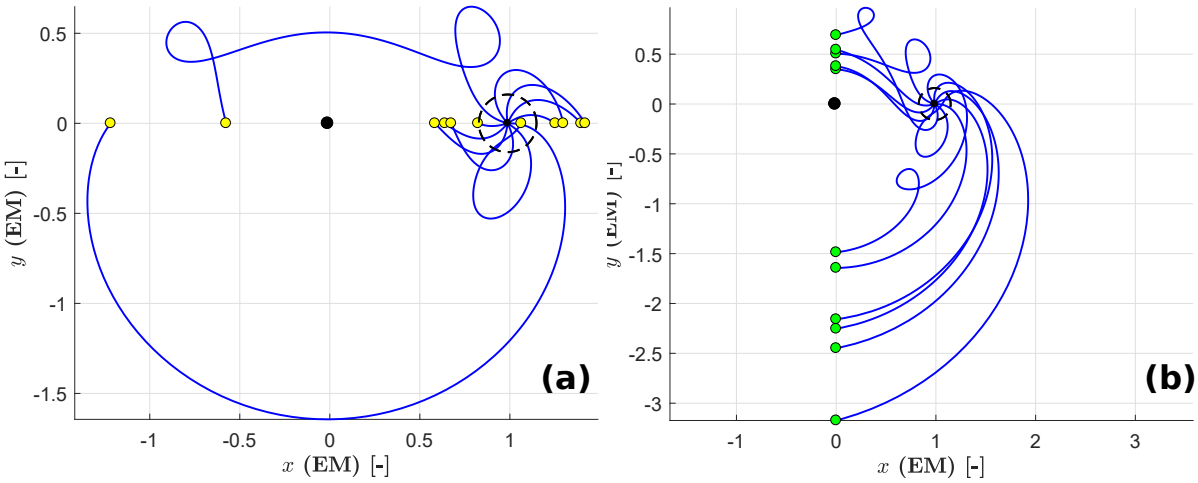

Figure 3.5: Poincaré cut examples with lunar ejection orbits (blue); **(a)** x-axis Poincaré cut, yellow intersections; **(b)** y-axis Poincaré cut, green intersections. Earth and Moon depicted as black dots at $(x, y) = (-\mu, 0)$ and $(x, y) = (1-\mu, 0)$ respectively. Lunar Hill's sphere reported as a dashed black circle around the Moon.

3.2. Single M2M transfer

In this section, lunar collision orbits are used to retrieve and analyse single M2M transfers. The structure is subdivided in two different subparts: in Section 3.2.1 the procedure to obtain a ballistic single M2M transfer out of the lunar collision orbits' characteristics is highlighted, followed in Section 3.2.2 by a deep analysis of the obtained results from the previous section.

3.2.1. M2M transfer retrieval

In this section, the procedure to define and compute a single M2M transfer is presented, with the help of the information given by the intersections of the lunar ejection orbits with a Poincaré cut.
First of all, the main idea on how to define an M2M, one of the main targets of this master thesis, is here outlined. The basic concept is to employ a single Poincaré cut to find the intersections of two different sets of ejection orbits; these data is used to patch two *near*-collision lunar arcs together, therefore obtaining a properly defined and continuous M2M transfer. In this case, collision orbits really help in this procedure, since fly-by orbits behave similarly to collision ones; although this last assessment may intuitively be understood, it is extensively treated and confirmed in Section 3.2.2.
The underlying procedure is similar to what Koon et al. [14] applied to compute homoclinic and heteroclinic transfers about periodic orbits of the Lagrange points: basically, they reported the intersections of the invariant manifolds originated from periodic orbits of the collinear Lagrange points on well-defined Poincaré cuts of the same or different dynamical systems (for example Sun–Earth with Earth–Moon) in order to obtain a patched approximation of a transfer between the same (homoclinic) or different (heteroclinic) periodic orbits. Although the idea here developed resembles the one Koon et al. dealt with, since Poincaré cuts are employed and a patching of two trajectories is sought, the difference stands in both the *purpose* and the *character* of the patching: indeed in this section the author is not trying to merge orbits heading to or departing from a periodic orbit about a Lagrange point, but rather orbits passing close by the Moon, without using invariant manifolds of periodic orbits about Lagrange points, but rather lunar collision orbits.
As stated in Section 3.1, ejection orbits are propagated from the lunar centre at $(x, y) = (1-\mu, 0)$ in the synodic barycentric reference frame, up to the point they intersect the Poincaré cut. In this section, the positive $y-$axis is used as cut, looking at the intersection presenting $\dot{x} \geq 0$. An introductory example on how the intersections of the collision orbits *look like* on the Poincaré cut mentioned above is given in Figs. 3.6a and 3.6b, in the case orbits are propagated backward in time, in the $y\dot{y}$- and $\dot{x}\dot{y}$-plane respectively. First intersections only with the cut is reported.

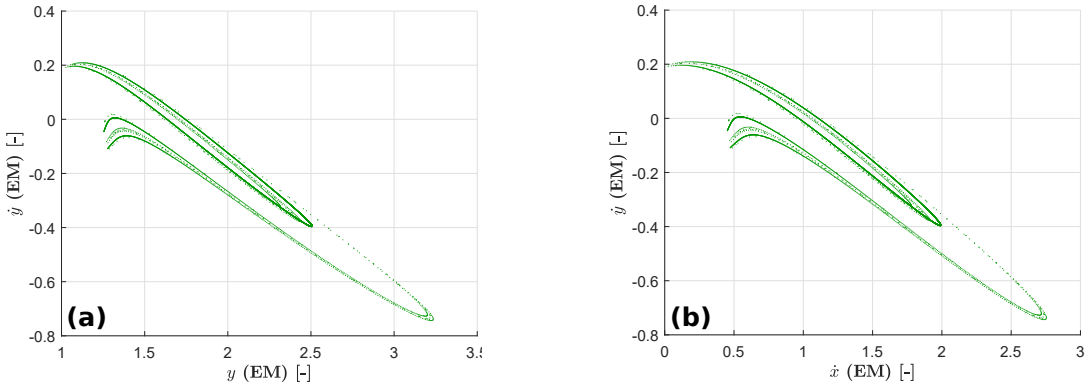

Figure 3.6: Intersections of 12000 backward-propagated lunar ejection orbits with the Poincaré cut on the positive y-axis. First encounter only, with $\bar{C} = 2.97$ and $\dot{x} \geq 0$ at intersection is here shown; representation on the **(a)** $y\dot{y}$- and **(b)** $\dot{x}\dot{y}$-plane.

Figure 3.6 clearly demonstrates the mathematical correctness of the employment of the cut, that is, it does contain neither any critical point, as assessed in Section 3.1 neither any non-transversal point. The former condition is trivial to verify but the latter may raise some doubt: indeed, the curve in Fig. 3.6b almost touches the vertical $\dot{x} = 0$ line. Although this does not happen for this energy level, for different values of $\bar{C}$ it may be the case; however, intersections are stored pointwise, therefore obtaining collision orbits which do not respect the constraint is rather improbable. Nevertheless, by continuity, there exists a proper set of initial conditions for lunar ejection orbits with a certain $\bar{C}$ leading to the unlucky condition mentioned above: in this case, that set should be discarded to save the transversality condition.
The shape drawn by the dots in Figs. 3.6a and 3.6b seem rather similar: this translates into an almost linear correlation between the y- and $\dot{x}$- coordinate of the first order intersection points. For this reason, only one of the two representations is shown for the remainder of this report, namely the $y\dot{y}$- one, which brings the *space* coordinates y, ideal to show when seeking a patching.
In order to obtain an M2M transfer, two sets of intersections of lunar ejection orbits with the same value of Jacobi constant $\bar{C}$, are visualized on the same Poincaré cut. Since the M2M is a transfer starting from the Moon and heading back to it, a Poincaré cut which highlights orbits both *arriving* at and *leaving* the cut is needed. This is achieved by employing two different propagation directions, namely one integrating the state forward in time and one backward. The symmetry in time is valid for trajectories propagated with the BR4BP model, as stated in Section 2.2.2; this result is easily extendable to the simpler CR3BP case, therefore reducing by half the required computational time. In case $t_0 \neq 0$, the symmetry still holds, since either a switch to $-t_0$ is applied or the *translation property* for autonomous systems is used, as discussed in Section 2.1.2.
It is further specified how the same sign for the not-plotted quantity (namely $\dot{x}$) needs to be ensured for intuitive reasons. Depending on at which axis the patching is sought, the order of the encounters (intersections) with the Poincaré cut should always be taken into account: for this reason, the forward- and backward-propagated intersections of the lunar ejection orbits with the Poincaré cut have always a different order, which is shortened in this report as $\left(n^{th}\,\text{bw}, m^{th}\,\text{fw}\right)_{a\pm}$, where $a\pm$ indicates the positive or negative semi-axis a, while n, m the two orders of the backward (bw) and forward (fw) propagation, respectively. As an example, the *first-backward* with the *second-forward* intersections with the positive y-axis, shortened to $\left(1^{st}\,\text{bw}, 2^{nd}\,\text{fw}\right)_{y+}$ is shown in Fig. 3.7a. The great characteristic of the symmetry mentioned above is that Fig. 3.7a is the symmetric counterpart about the $\dot{y}$ axis of the $\left(2^{nd}\,\text{bw}, 1^{st}\,\text{fw}\right)_{y-}$ with $\dot{x} < 0$.
As a final step before obtaining an M2M transfer, a point on the Poincaré cut is taken: since the order of the encounter is *low*, if a point which is close to the *first-backward* set of points is propagated forward in time, then the obtained trajectory passes by the Moon. The same result holds if a point which is close to the *second-forward* set of intersections is propagated backward in time. This result is confirmed by Fig. 3.7. More on this is pointed out in Section 3.2.2.
As a successive step, an M2M transfer is expected if a point on the Poincaré cut, close to both the intersections, is taken as starting point for the propagation. As an example, Figs. 3.8a and 3.8b show the location of two possible candidate points in their global and magnified view on the cut, respectively, while Figs. 3.8c and 3.8d show the propagated results. The latter confirm both the intuition and the applicability of the method itself.
It is further stressed out how, for the *time symmetry*, another free ballistic M2M transfer is automatically obtained for each one already computed; thanks to both the *translation property* and the autonomous characteristic of the CR3BP, setting an initial epoch does not add complexity to the problem.

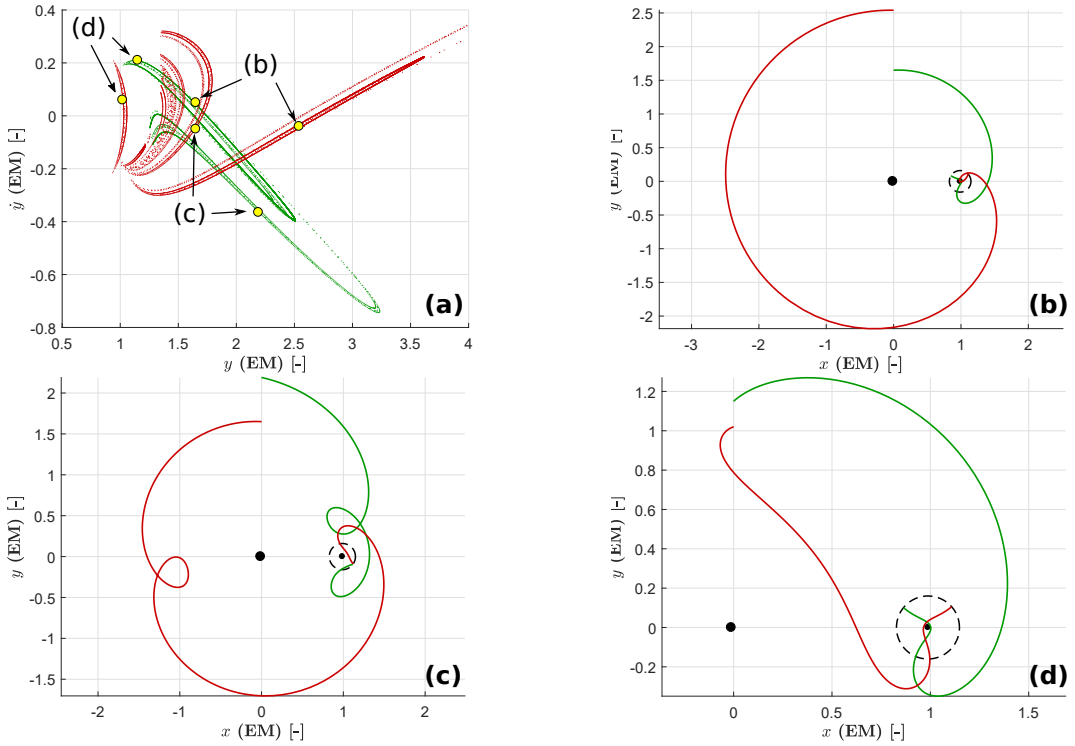

Figure 3.7: **(a)** $\left(1^{st}\text{ bw}, 2^{nd}\text{ fw}\right)_{y+}$ intersections (green and red respectively) with the positive y-axis. $\bar{C} = 2.97$ and $\dot{x} \geq 0$; **(b)** to **(d)** propagated orbits from the cut, according to the location in (a). Backward- and forward- propagated transfers in red and green respectively. Earth and Moon as black dots. Lunar Hill's sphere depicted as a dashed circle about the Moon.

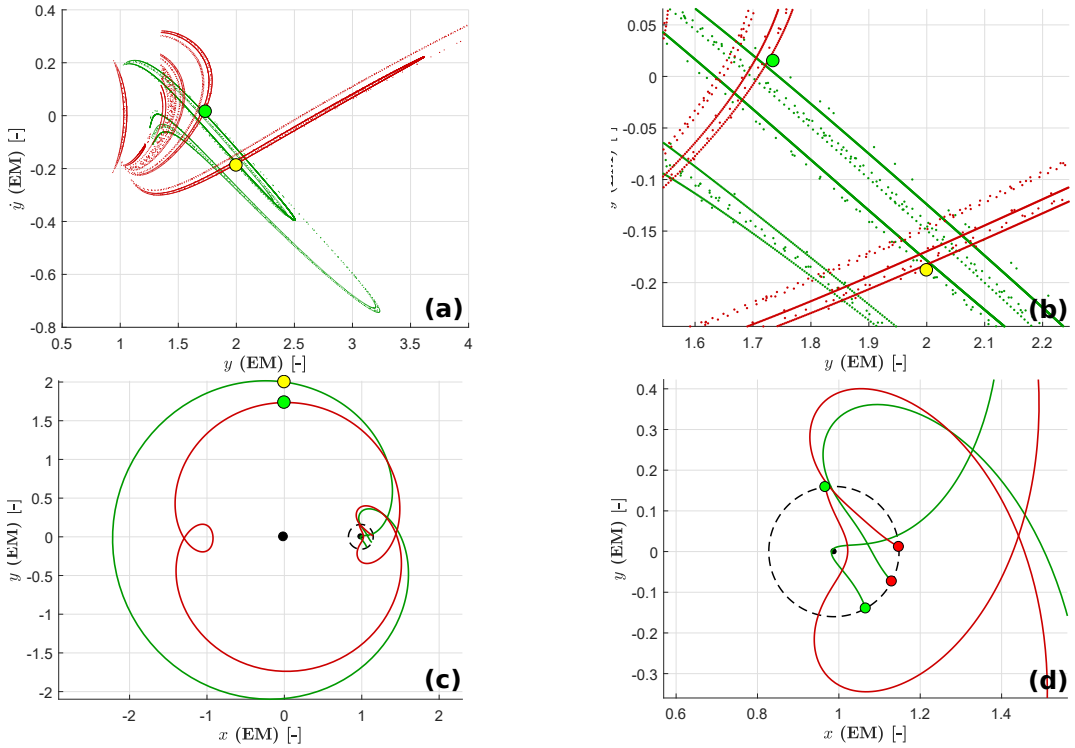

Figure 3.8: **(a)** Location of the propagated points on the y-axis Poincaré cut, for $\bar{C} = 2.97$, with $\dot{x} \geq 0$; **(b)** magnified view of (a); **(c)** resulting propagated orbits from the intersection points in (a) in (yellow point) and red (green point). Earth and Moon depicted as black dots, lunar Hill's sphere as dashed black circle about the Moon; **(d)** magnified view of (c) in a neighbourhood of the Moon. Starting and ending states for the trajectories depicted in green and red respectively.

3.2.2. M2M analysis

In this section a qualitative analysis on the relationship between the lunar collision orbits and the M2M transfers is performed, highlighting important characteristics of the latter. Dealing with a hard nonlinear dynamics, a numerical grid search approach is here preferred. Every grid point on the Poincaré cut is propagated to find the unique associated trajectory; from each of those, one can compute different interesting quantities which are reported and shown at the relative initial states on the cut. Therefore a point on the cut plotted with a certain characteristic is the origin of a trajectory carrying that particular characteristic. Data are shown on the cut in a colorwise fashion or by extending the concept to a third dimension. In the latter case, the intersections of the ejection orbits with the cut are merely used as reference, without respecting the out-of-plane criteria. A specific area of the whole search space is here analysed, as depicted in Fig. 3.9: trajectories are both forward- and backward- propagated from there. Although the plots are concerned with a specific and bounded region of the whole domain, the same analysis has ben carried out in other interesting areas, leading to the same qualitative results.

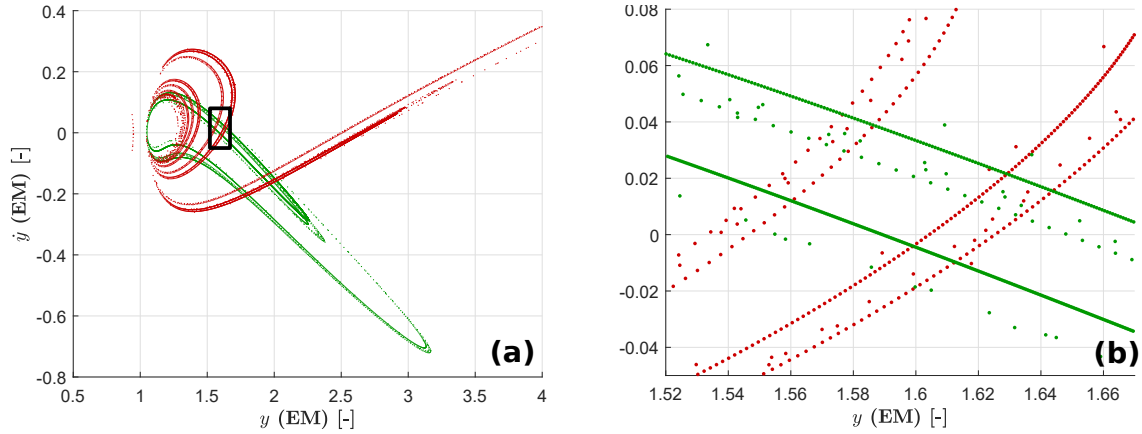

Figure 3.9: **(a)** General view of the studied area (black box) of the whole domain. $\left(1^{st}\,\text{bw}, 2^{nd}\,\text{fw}\right)_{y+}$ intersections (green and red, respectively), with $\dot{x} \geq 0$ and $\bar{C} = 3.01$; **(b)** magnification inside the black box.

The Jacobi constant $\bar{C}$ is now changed with respect to previous analysis, as visible from the different shape, in order to give an idea on how a Poincaré cut *moves* by changing $\bar{C}$. This analysis can however be performed at other plausible values of $\bar{C}$, without qualitatively changing the main final outcome. In Fig. 3.10 the trajectories are analysed with respect to the reached perilune r_2 for both the forward- and backward-propagated arc. This allows to numerically validate a previously implicit assertion: indeed, the results show that a small shift from the intersection of the collision orbit for the initial propagated state on the cut is consequently mapped by the flow to a certain distance from the Moon at the trajectory's closest passage. This mapping is not purely random, but it follows a continuous trend when departing from the intersections of the collision orbits on the Poincaré cut. Indeed, the more one shifts from the backward-propagated intersections of the collision orbits on the cut (green), the more the forward-integrated trajectories are missing the Moon, as depicted in Fig. 3.10b; a similar trend can be inferred for the forward-propagated intersections of the lunar ejection orbits with the cut (red) and the backward-integrated trajectories in Fig. 3.10a. Chaotic regions and other blue shadows are due to high-order intersections with the cut, which are not here reported to ease the reading. However, these become a central topic in Chapter 4. In Fig. 3.10c the region for feasible M2M transfers is outlined: every black dot, once opportunely propagated, generates an M2M transfer, according to the requirements pointed out in Section 3.1.

In Figs. 3.11a and 3.11c the angular momentum with respect to the Moon h_2 at perilune is reported, for the backward- and forward-propagated arcs respectively, along the $z-$axis; the relative top-views are shown in Figs. 3.11b and 3.11d. The separatrix nature of the collision orbits with respect to *prograde* and *retrograde* trajectories at the Moon ($h_2 > 0$ and $h_2 < 0$ respectively) is evident, as confirmed by Oshima et al. [21]. The backward-integrated arc of Figs. 3.11a and 3.11b shows the separatrix nature of the forward-integrated collision orbits; similarly happens for the forward-integrated arc and the backward-propagated ejection orbits in Figs. 3.11c and 3.11d. Especially for the backward-integrated arcs in Fig. 3.10a, only the closest region to the intersections on the cut is shown, since the dynamics of high-order encounters rapidly takes place.

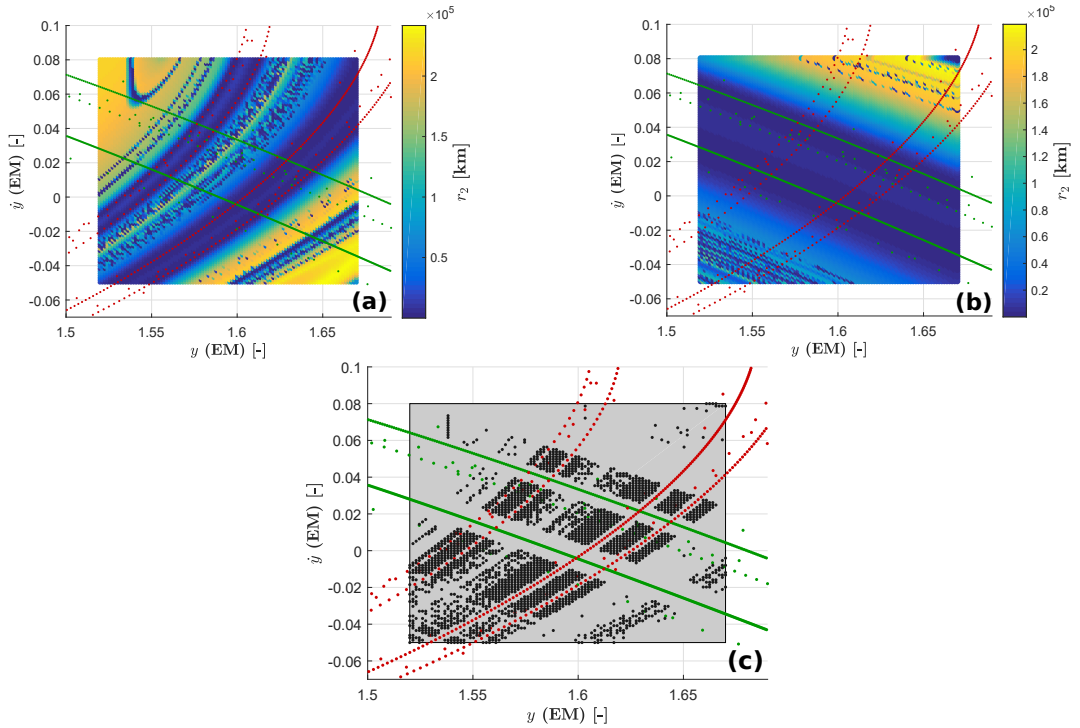

Figure 3.10: $\left(1^{st}\text{bw}, 2^{nd}\text{fw}\right)_{y+}$ intersections (green and red, respectively), with $\dot{x} \geq 0$, $\bar{C} = 3.01$; colors show perilunes for **(a)** backward- and **(b)** forward-propagated trajectories; **(c)** black dots report the propagation points satisfying the M2M transfer requirements.

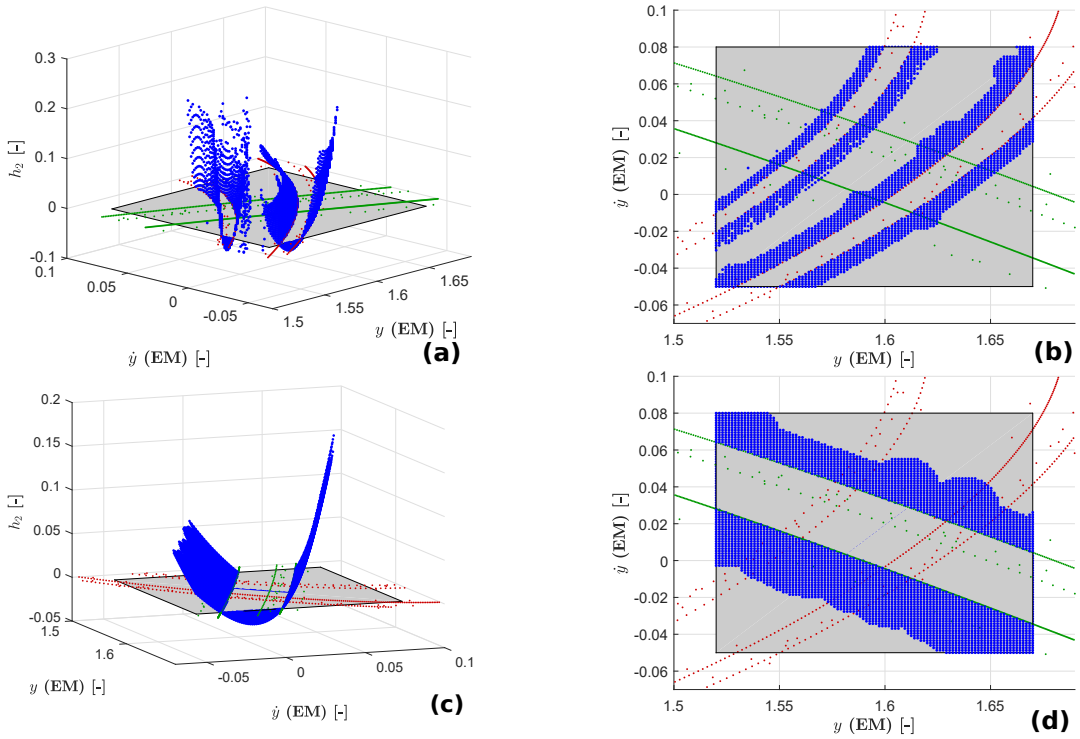

Figure 3.11: $\left(1^{st}\text{bw}, 2^{nd}\text{fw}\right)_{y+}$ intersections (green and red, respectively), with $\dot{x} \geq 0$ and $\bar{C} = 3.01$; **(a)** on the z-axis the angular momentum with respect to the Moon, h_2, at perilune for the backward-integrated arcs; **(b)** top-view of (a); **(c)** on the z-axis the angular momentum with respect to the Moon, h_2, at perilune for the forward-integrated arcs; **(d)** top-view of (c).

The energy with respect to the Moon H_2 at perilune[1] for each arc is plotted in Fig. 3.12. In particular, following the same scheme addressed in Fig. 3.11, H_2 at perilune for the backward- and forward-integrated trajectories are plotted in Figs. 3.12a and 3.12b and in Figs. 3.12c and 3.12d respectively: again, it exists a separatrix boundary between the $H_2 > 0$ and $H_2 < 0$ regions, although the limit-curve is different from what is shown in Fig. 3.11 for h_2, where the separatrix nature of lunar collision orbits is evident. Results have shown how, by decreasing the value of $\bar{C}$, this boundary shifts towards the collision orbits. Although without explaining this behaviour, a deeper insight of this phenomena is given in Section 3.3.

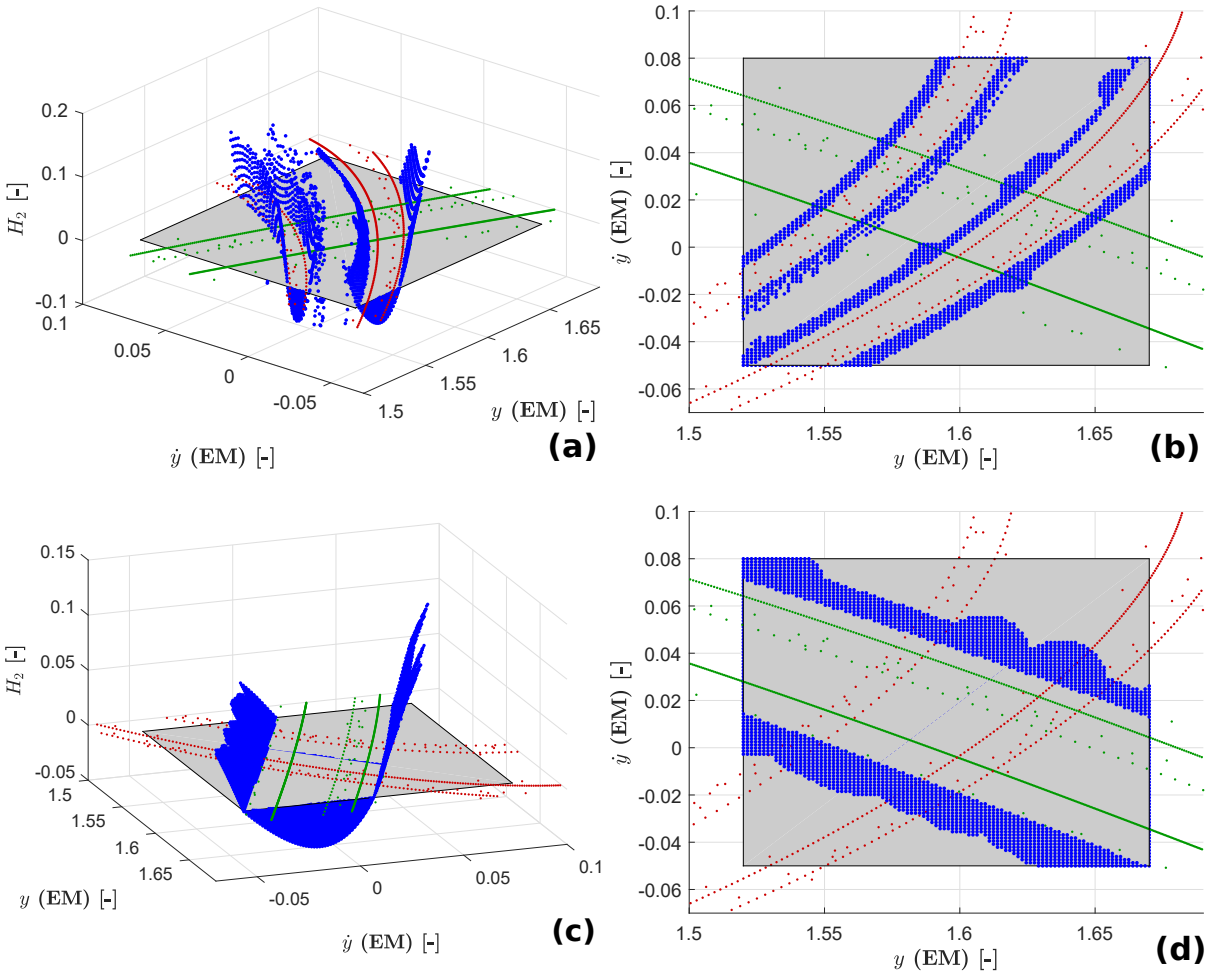

Figure 3.12: $\left(1^{st}\,\text{bw}, 2^{nd}\,\text{fw}\right)_{y+}$ intersections (green and red, respectively), with $\dot{x} \geq 0$ and $\bar{C} = 3.01$; **(a)** on the z-axis the energy with respect to the Moon, H_2, at perilune for the backward-integrated arcs; **(b)** top-view of (a); **(c)** on the z-axis the energy with respect to the Moon, H_2, at perilune for the forward-integrated arcs; **(d)** top-view of (c).

To conclude this section and to provide another interesting characterizing element, a wider grid of initial points on the cut is backward-propagated in time, encompassing the feasible domain (given by the condition $J(\boldsymbol{x}|_{cut}) = \bar{C}$). The main results are reported in Fig. 3.13, in the usual colorwise fashion. Due to the backward integration scheme, both figures follow in colors the trend given by the forward-propagated lunar collision orbits, for both low- and high-order encounters. Even though only the second-order forward propagated intersections are superimposed on the grid (in red), high-order encounters are not shown to ease the reading. In Fig. 3.13a the minimum perigee heights R_1, propagated from every initial point on the grid are shown, while in Fig. 3.13b the associated time to reach the perigee t_{R_1} is reported (taken as positive).

[1] H_2, as well as the angular momentum with respect to the Moon h_2 have a correct meaning whereas the trajectory is primarily influenced by the Moon. Since the outer boundary of an M2M transfer is set at the lunar Hill's sphere (smaller than the lunar Sphere of Influence), both H_2 and h_2 are meaningful in this analysis.

The points on the Poincaré cut getting close to Earth backward in time are mainly set *between* pairs of the same-order intersections of the collision orbits with the cut. Indeed, the other depicted blue-shadows are contained between high-order forward-propagated lunar collision orbits. *Chaotic* regions are present in the general picture, to further confirm the behaviour of the involved dynamics.

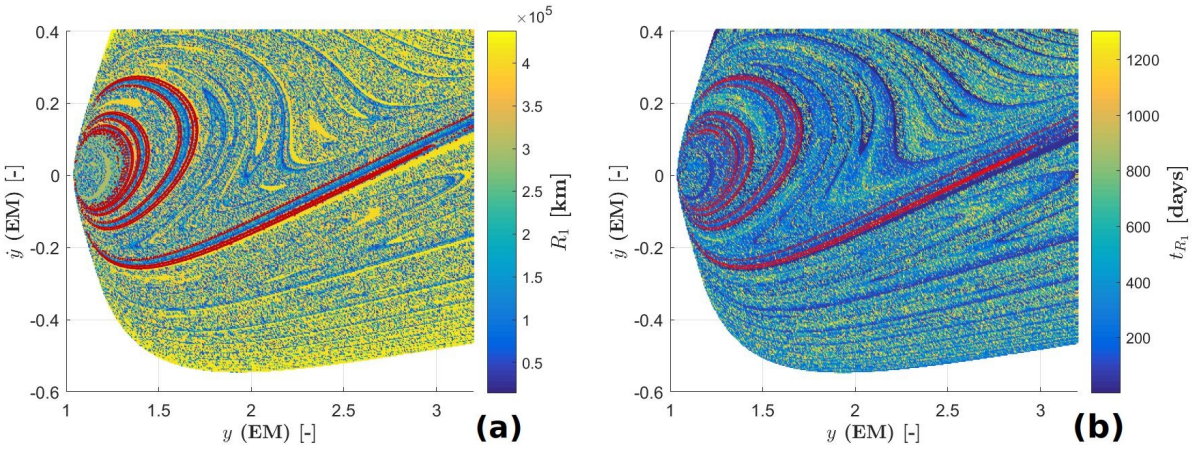

Figure 3.13: Second-order intersections of the forward-propagated lunar collision orbits (red) with the Poincaré cut on the positive y-axis, for $\bar{C} = 3.01$ and $\dot{x} \geq 0$; grid of points propagated backward in time, reporting **(a)** minimum perigee heights and **(b)** the associated time to reach the perigee.

3.3. Collision and Lyapunov orbits

A special attention is given in this section to the simple periodic orbits of the collinear Lagrange points; in particular, it is pointed out a similar behaviour of lunar collision orbits with the invariant manifolds emanated from the Horizontal Lyapunov Orbits (HLOs') related to the collinear Lagrange points.
One of the intuition leading to this research was to solve for the bad-behaving nature of the invariant manifolds of the periodic orbits associated to the Lagrangian points by using lunar collision orbits. These invariant manifolds are computed according to the algorithm explained in Section 2.2.1.
In particular, the stable and unstable invariant manifolds of the L_2-originating HLO intersect the positive $y-$axis, as depicted in Figs. 3.14a and 3.14b respectively (in black) for the stable and unstable manifold (both exterior and interior branches). Analogously happens for the negative $y-$axis, although not shown here.

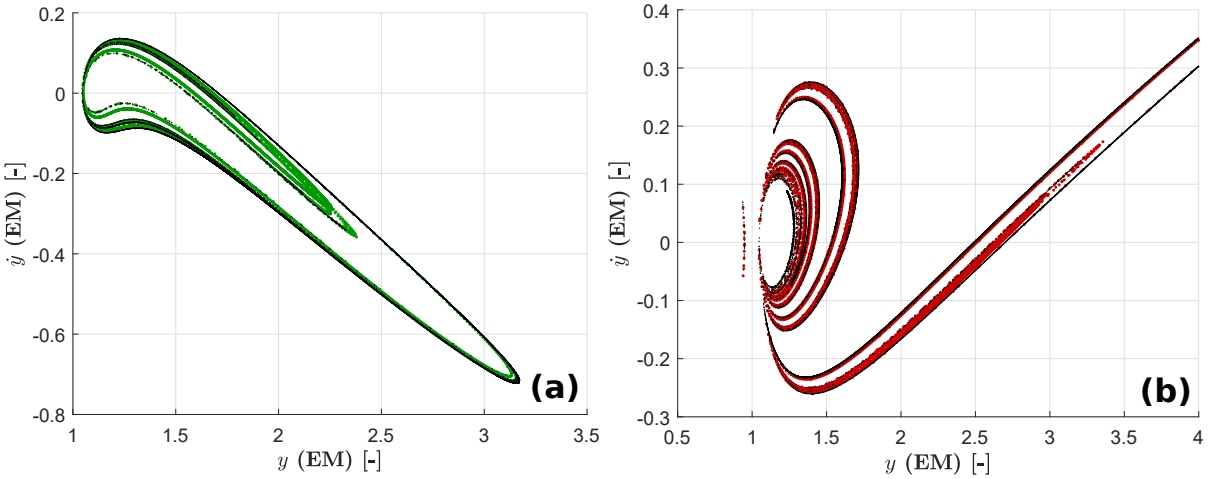

Figure 3.14: **(a)** First order intersections of the backward-propagated lunar collision orbits (green) and the stable invariant manifolds of the L_2 HLO (black) with the Poincaré cut at the positive y-axis; **(b)** second order intersections of the forward-propagated lunar collision orbits (red) and the unstable invariant manifolds of the L_2 HLO (black) with the Poincaré cut at the positive y-axis; $\bar{C} = 3.01$ and $\dot{x} \geq 0$.

It is quite remarkable how, similarly to what obtained by Oshima et al. [21], the invariant manifold of the HLO in L_2 *shadows* the intersections of the collision orbits. The same behaviour is recognizable at lower values of $\bar{C}$ (again, not shown here). However, the latter invariant manifold shadows *part* of the whole collision-orbit figure, namely the external region only, where the collision orbits are rarefied, since represented by a low-density trace of points. An example of a collision orbit piercing the Poincaré cut close to an intersection of the invariant manifold of the L_2 HLO with the same cut, is depicted in Fig. 3.15, together with the associated trajectory from the invariant manifold. Their similarity is evident.

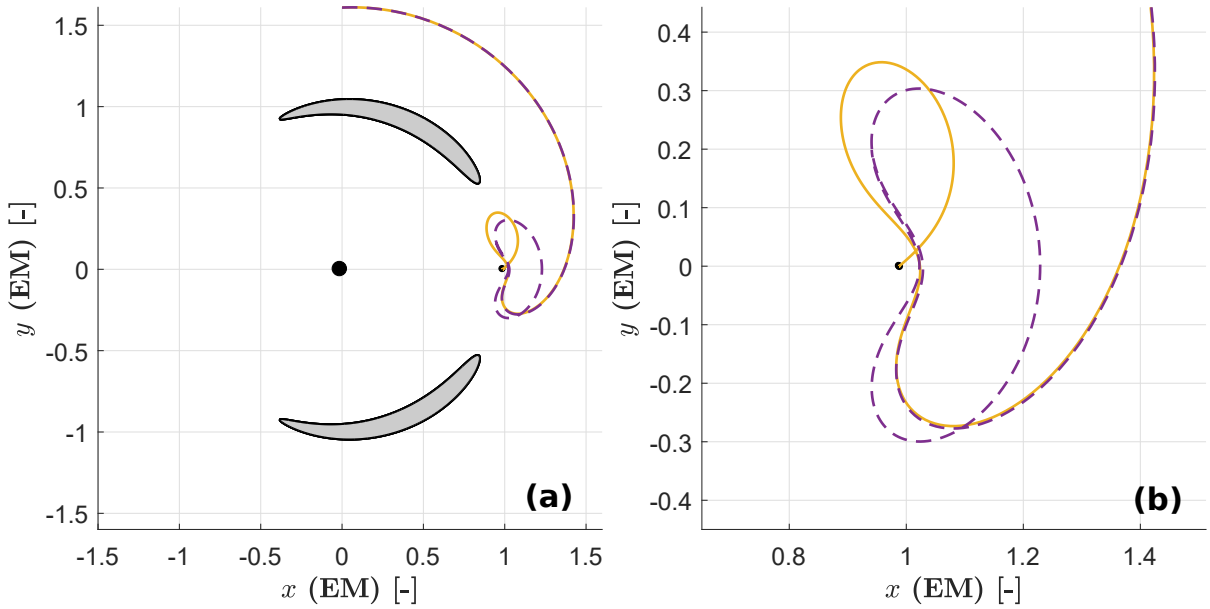

Figure 3.15: **(a)** Forward-integrated collision orbit (straight yellow) and orbit approaching L_2 HLO on the stable manifold (dashed magenta), from two close initial points on the Poincaré cut. Zero Velocity Curve highlighted in grey. Earth and Moon depicted as black dots; **(b)** magnification of (a) in a neighbourhood of the Moon.

Analogously to what is observed in Fig. 3.14, the invariant manifolds associated with the HLOs' of L_1 and L_3 at the same $\bar{C}$ can be represented: as shown in Figs. 3.16a and 3.16b, respectively for L_1 and L_3 HLOs' for the stable branch only (both exterior and interior), they maintain the shadowing characteristic with the collision orbits.

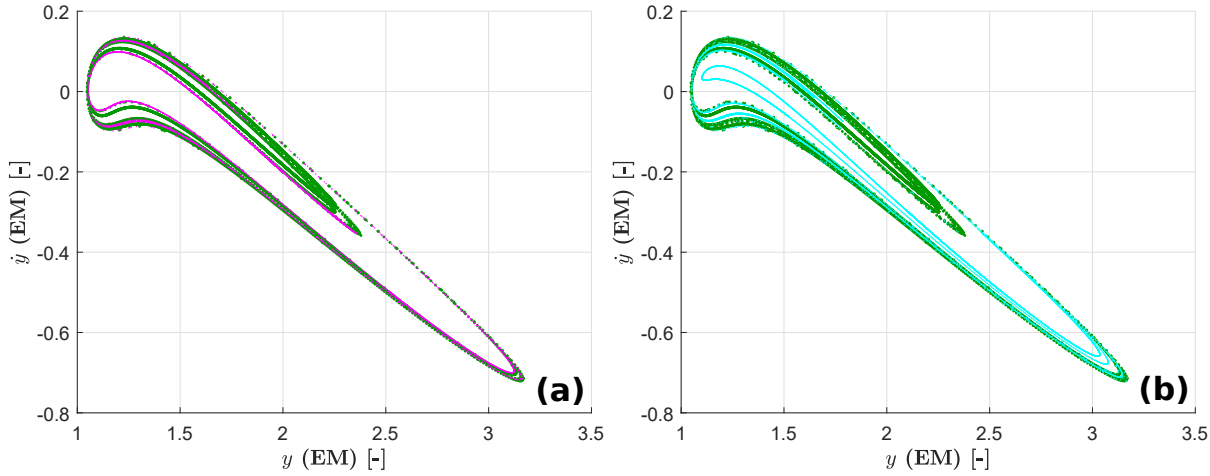

Figure 3.16: First order intersections of lunar ejection orbits (green) and the stable invariant manifold of **(a)** L_1 (magenta) and **(b)** L_2 (cyan) HLOs' with the Poincaré cut at the positive y-axis.

A similar result is observable for L_1 HLO for what concerns the unstable branch. However, for the first intersection of the unstable invariant manifold emanating from L_3 HLO with the positive $y-$axis, the shadowing characteristic is maintained, although merely in the inner circle of the second-order intersection of the forward-propagated collision orbits (red): this is comprehensible, since the L_3 unstable invariant manifold does not pass close by the Moon, therefore it does not receive a sensible gravitational influence. Nevertheless, the third encounter of the L_3 HLO with the Poincaré cut gains back the typical structure shown by the collision orbits, since trajectories now pass close by the Moon. The same analysis is applicable with the first intersection of the interior unstable invariant manifold of L_3 HLO with the negative $y-$axis, once compared to the second-order forward-propagated collision orbits.
Concluding, comparing the results of Figs. 3.14a and 3.14b with Figs. 3.12a and 3.12c it can be inferred how the intersections of the invariant manifold associated with L_2 HLO may have a separatrix nature with respect to the lunar energy at perilune for trajectories approaching the Moon. Figure 3.17 shows how the external part is ruled by the invariant manifold emanating from L_2 HLO (black), while the internal one by the L_1 HLO (magenta). The invariant manifolds are computed slightly changing $\bar{C}$, according to the algorithm highlighted in Section 2.2.1, therefore the location of the points loses in accuracy. However, it seems how the invariant manifolds emanating from L_2 HLO (black) are slightly shifted from the $H_2 = 0$ boundary. Although not shown in this report, the same procedure has been repeated for different areas and for a range of $2.97 \leq \bar{C} \leq 3.01$. If the analysis is limited to a particular $\bar{C}$, the separatrix behaviour with respect to perilune H_2 is overall the same across the cut; however, by comparing the results for different values of $\bar{C}$, the outcome changes, since the separatrix nature is once more imputable to the invariant manifold of the HLO and once to the collision orbits. Therefore, it can be stated how it exists a different (and unknown up to now) object, which stands in between the two elements here treated, namely collision orbits and invariant manifold of HLOs', carrying this interesting separatrix property about H_2. This report does not show *who* this character is, although it claims how it is bounded by the collision orbits and the treated invariant manifolds.

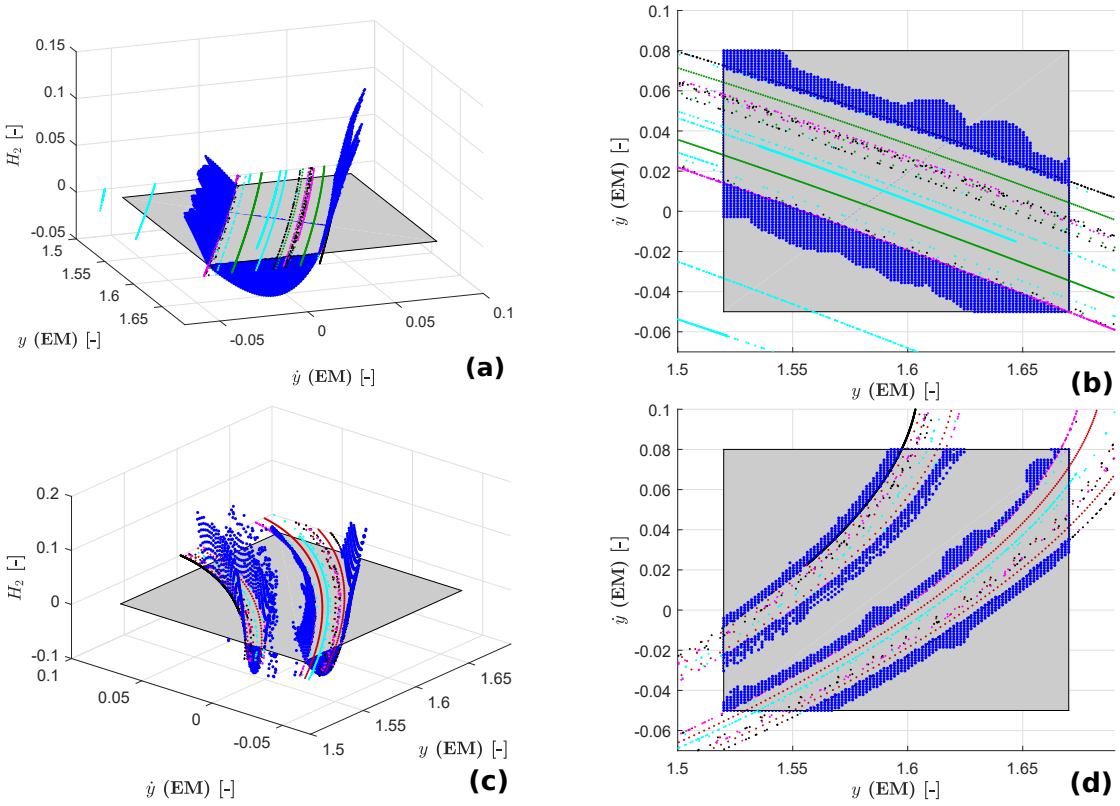

Figure 3.17: Trend of H_2 at perilune (in blue) for trajectories propagated from the Poincaré cut; **(a)** first-order intersections of backward-propagated lunar ejection orbits (green) with stable invariant manifold of L_2, L_1 and L_3 HLOs' (black, magenta and cyan respectively); in blue, H_2 for forward-propagated trajectories; **(b)** top-view of (a); **(c)** second-order intersections of forward-propagated lunar ejection orbits (red) with unstable invariant manifold of L_2, L_1 and L_3 HLOs' (black, magenta and cyan respectively); in blue, H_2 for backward-propagated trajectories; **(d)** top-view of (c).

3.4. Conclusion and possible applications

The analysis performed in the previous sections outlines important qualitative characteristics about the M2M transfers in the Earth–Moon CR3BP. This section summarizes the most prominent aspects, presenting possible applications of the latter as a preliminary trajectory design or analysis tool; indeed, due to the simplification introduced by the dynamical model, the applicability of this research is constrained to a first-order design only.

In the first part, the features of the intersections of lunar collision orbits with the Poincaré cut on the positive y-axis are extensively discussed. In particular, Section 3.2.2 reports the location of the points on the cut so that the propagated trajectories have certain characteristics in terms of minimum distance from the Moon, angular momentum and energy at perilune, referred to as r_2, h_2 and H_2 respectively.

In order to find a proper M2M transfer, a certain distance from the intersections of the collision orbits with the cut needs to be maintained, as shown in Fig. 3.10c. This limits the available space to certain regions which are not too far from but not too close to the intersections of the collision orbits with the cut; however, by looking at the behaviour of the perilunes, an initial point on the cut so that a certain condition is reached can be easily selected. This is helpful for trajectory design and analysis purposes.

For what concerns the angular momentum at perilune, lunar collision orbits show a parabolic-like separatrix nature for trajectories approaching and departing from the Moon, distinguishing the *prograde* from the *retrograde* motion. The energy H_2 for trajectories approaching the Moon at perilune, shows an analogous parabolic-like behaviour, although with respect to a particular curve different from the one drawn by lunar collision orbits: together with what is described for h_2, this can be leveraged to target specific conditions at lunar encounter, both qualitatively (in sign) and to a lesser extent quantitatively (in magnitude). This knowledge can be employed as an analysing tool: indeed, H_2 is a key-element when referring to orbital *capture*, while the sign of h_2 is an important parameter for lunar fly-by.

In Section 3.3, the invariant manifolds associated with HLOs' about the collinear Lagrangian points are treated together with lunar collision orbits in order to highlight their relation: following from Conley [7], these invariant manifolds have an intrinsic separatrix behaviour for what concerns the inbound and outbound motion of a massless body (like a spacecraft) with respect to the analysed system (for example, Earth–Moon). Extending his results to the case discussed in this report, a threefold behaviour for the orbits propagated from the cut can be observed: depending on the location of the starting point, they can remain within the originating zone (inner and outer), they can asymptotically reach the HLO or they can escape from one zone reaching the other one. With reference to Fig. 3.13, a point on a blue region can be potentially selected in order to have a backward close encounter with the Earth and at the same time leverage the information brought by the invariant manifold. An example of a possible behaviour is depicted on the cut in Fig. 3.18a for a trajectory experiencing a ballistic Earth-M2M-escape sequence (green dot), later plotted in Figs. 3.18c and 3.18d in both the synodic and Earth-centered inertial reference frame. This can be used to obtain a first-guess solution for a highly elliptic orbit which actively and repeatedly benefits from Moon's presence in order to ballistically escape from the Earth–Moon system: this is, to a certain extent, the baseline of JAXA's DESTINY+ mission. As a subsequent example, in Fig. 3.18b two points are highlighted which, once propagated, direct the spacecraft towards an HLO in L_2 and L_3 (yellow and magenta, respectively). The propagated trajectories, both fully ballistic and accounting for a single M2M transfer, are shown for the HLO at L_2 in Figs. 3.18e and 3.18f and at L_3 in Figs. 3.18g and 3.18h. Collision orbits clearly demonstrate a similar behaviour to the invariant manifolds emanating from HLOs': this may suggest how the former can be employed as a substitute of the latter, being less complex to compute and behaving better on a wider energetic range.

All in all, new characteristics concerning collision orbits are here shown, which are not addressed in the existing literature. The knowledge presented in this chapter, concerned with the single M2M transfer in the Earth–Moon CR3BP, is further extended in the next one, by embracing more complex themes. For this reason, more general remarks pertaining to the subject here treated are delayed to the conclusions of Chapter 4.

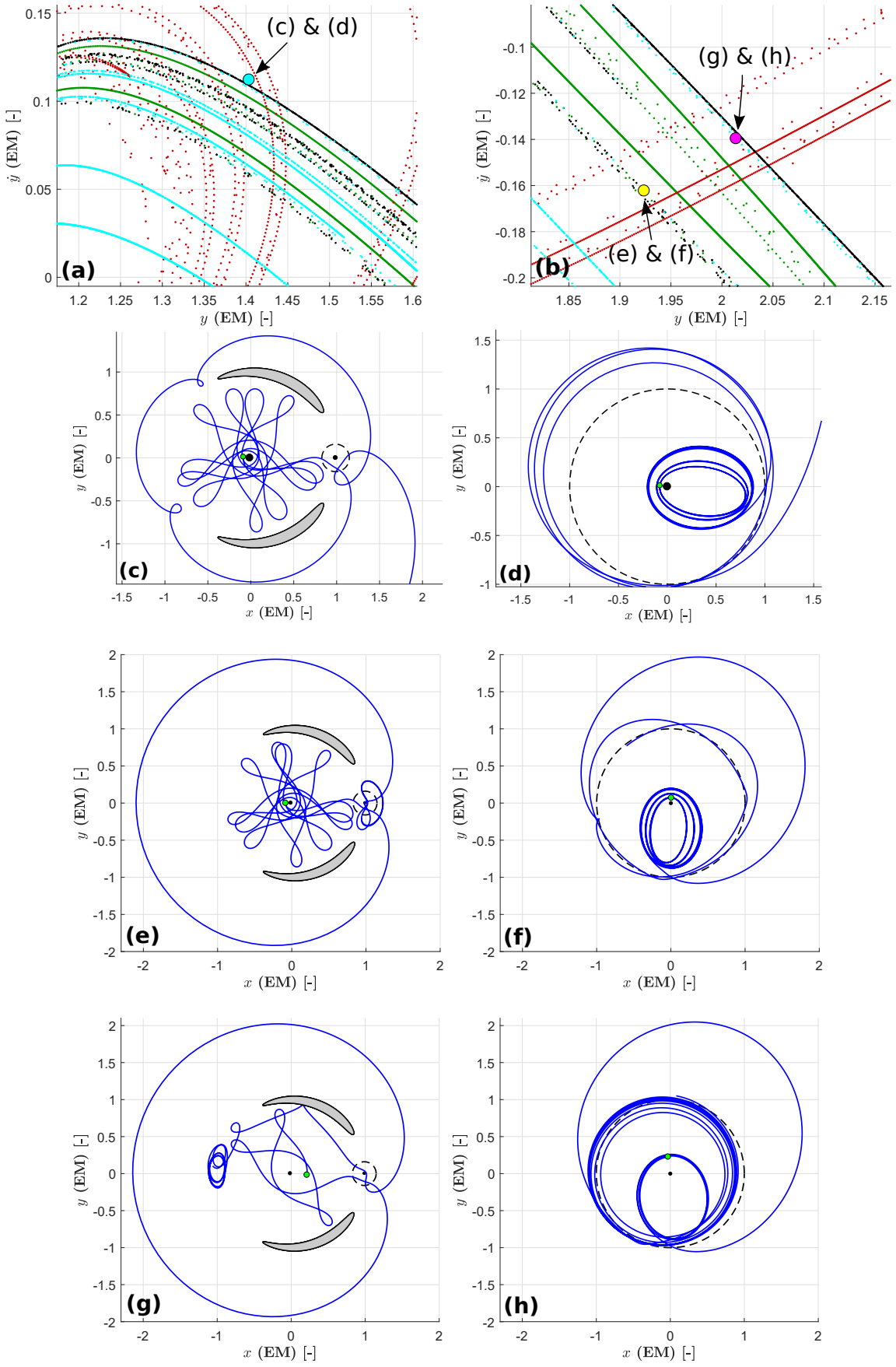

Figure 3.18: **(a)** & **(b)** $\left(1^{st}\text{ bw}, 2^{nd}\text{ fw}\right)_{y+}$ intersections (green and red respectively) and stable invariant manifolds from L_2 and L_3 HLOs' (black and cyan respectively). $\bar{C} = 3.01$. Earth-M2M-escape ballistic sequence propagated from the cyan dot of (a) depicted in **(c)** and **(d)** for the synodic barycentric and Earth-centered inertial reference frames (≈ 238 days); Earth-M2M-HLO in L_2 ballistic sequence propagated from the yellow dot of (b) depicted in **(e)** and **(f)** for the barycentric synodic and Earth-centered inertial reference frames (≈ 208 days); Earth-M2M-HLO in L_3 ballistic sequence propagated from the magenta dot of (b) depicted in **(g)** and **(h)** for the barycentric synodic and Earth-centered inertial reference frames (≈ 313 days). Earth and Moon are black dots in the synodic frame, while lunar Hill's sphere is as a dashed circle. Lunar orbit about the Earth plotted as a dashed circle in the inertial frame.

4

Extended M2M transfer in the Earth–Moon CR3BP

With the results shown in the previous chapter, more complex topics are here discussed, extending the concept of the single M2M transfer in the Earth–Moon CR3BP. The structure is divided in three main parts. Lunar collision orbits and Poincaré cuts are again largely employed: in Section 4.1, a method to obtain ballistic sequences of M2M transfers is presented, while in Section 4.2 the constraint of a ballistic trajectory is removed, allowing to obtain controlled M2M transfers by means of a Δv. Section 4.3 concludes both this chapter and the discussion concerning M2M transfers in the CR3BP.

4.1. Ballistic multiple M2M transfer

In this section, a method to obtain a so-called ballistic *multiple* M2M transfer is highlighted. First, an important definition is here given:

Definition Multiple M2M transfer:
A multiple M2M transfer, interchangeably referred to as *sequence* of M2M transfers, is defined as a succession in time of single M2M transfers which are mutually and continuously patched.

The main idea behind a multiple M2M transfer is based on the same approach outlined in Section 3.2, although the complexity is here enhanced: briefly, the M2M transfers are found by propagating points on the Poincaré cut at the positive $y-$axis which are close to both the second-order forward-propagated and first-order backward-propagated intersection sets of the collision orbits with the common cut, briefly referred to as $\left(1^{st}\,\text{bw}, 2^{nd}\,\text{fw}\right)_{y+}$. This combination of orders is one of the best two options (together with its symmetric counterpart) since both sets are obtained by the collision orbits which travel the closest distance between the start (namely the Moon) and the Poincaré cut (the positive $y-$axis); this leads to the lowest possible contribute by the nonlinear dynamics to the trajectory.
However, different orders of intersections may be used: if for example a region of the search space on the cut has the peculiarity of having points from the $\left(1^{st}\,\text{bw}, 3^{rd}\,\text{bw}\right)_{y+}$ sufficiently close, that area is *probably* reach of feasible M2M transfers, which can be obtained with a forward-propagation. However, with this approach, two drawbacks may occur. First, the collision orbit may perform a loop on the cut, therefore misleading the search. Second, as already suggested, the higher the order, the stronger the nonlinear effect of the dynamics since the longer the time to re-encounter the Moon. As it is stated above, in the latter case the propagation is performed in one direction only (forward) and there is no patching in between a single M2M transfer as it is done in Section 3.2.1: two starting points on the same cut which are slightly shifted may consequently lead to two completely different trajectories. In a similar fashion, this idea may be applied to the $\left(2^{nd}\,\text{fw}, 4^{th}\,\text{fw}\right)_{y+}$ intersections.
Following, the concept of a multiple M2M transfer is quite straightforward: indeed, taking points on the Poincaré cut which are simultaneously close to every of the above mentioned cuts may lead, after a proper propagation, to sequences of triple, double and single M2M transfers (the latter representing an extreme case). The intersections are referred to as $\left(1^{st}\,\text{bw}, 3^{rd}\,\text{bw}, 2^{nd}\,\text{fw}, 4^{th}\,\text{fw}\right)_{y+}$, consistently with the previous

nomenclature.
In order to show where these areas are, a grid search is performed to cover the whole feasible region on the cut; subsequently, every point in this grid is checked whether it has at least one point from every of the analysed cut in its neighbourhood. The latter is defined as an ellipse centered at every grid point, with semiaxes $r_y = 0.04$, $r_{\dot{y}} = 0.01$, whose magnitudes are defined by trial and error. Fig. 4.1a depicts the four analysed cuts, while Fig. 4.1b highlights the points of the grid complying with the requirement mentioned above (black dots). These points are propagated both forward an backward in time: if they comply with the requirements of a triple multiple M2M transfer, they are marked in yellow, while in magenta if representing a sequence of two M2M transfers. In Fig. 4.2a the trajectory propagated from one of the yellow points of Fig. 4.1b is presented, highlighting the triple M2M transfer, and subsequently magnified in Fig. 4.2b to point out the four different lunar swing-bys. Figure 4.2c highlights the trends in r_2 (red) and H_2 (blue) in time.

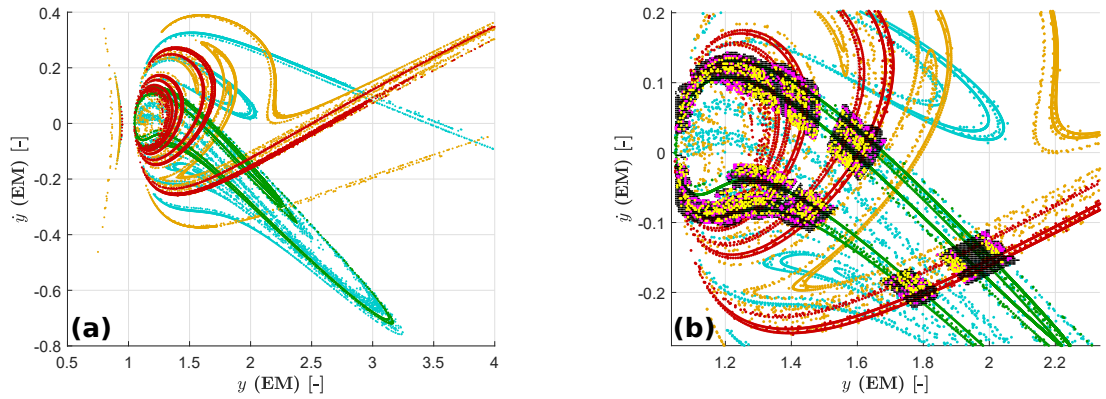

Figure 4.1: **(a)** $\left(1^{st}\,\text{bw}, 3^{rd}\,\text{bw}, 2^{nd}\,\text{fw}, 4^{th}\,\text{fw}\right)_{y+}$ intersections (green, cyan, red and orange respectively) with the Poincaré cut on the positive y-axis with $\bar{C} = 3.01$ and $\dot{x} \geq 0$; **(b)** magnification of (a), with highlighted the candidate points for the propagation (7207, black), the actual points generating a sequence of three and two M2M transfers (yellow, 1136 ≈ 16% and magenta, 889 ≈ 12% respectively). Mind how every sequence of three M2M transfers can be regarded as two distinct sequences of two M2M transfers.

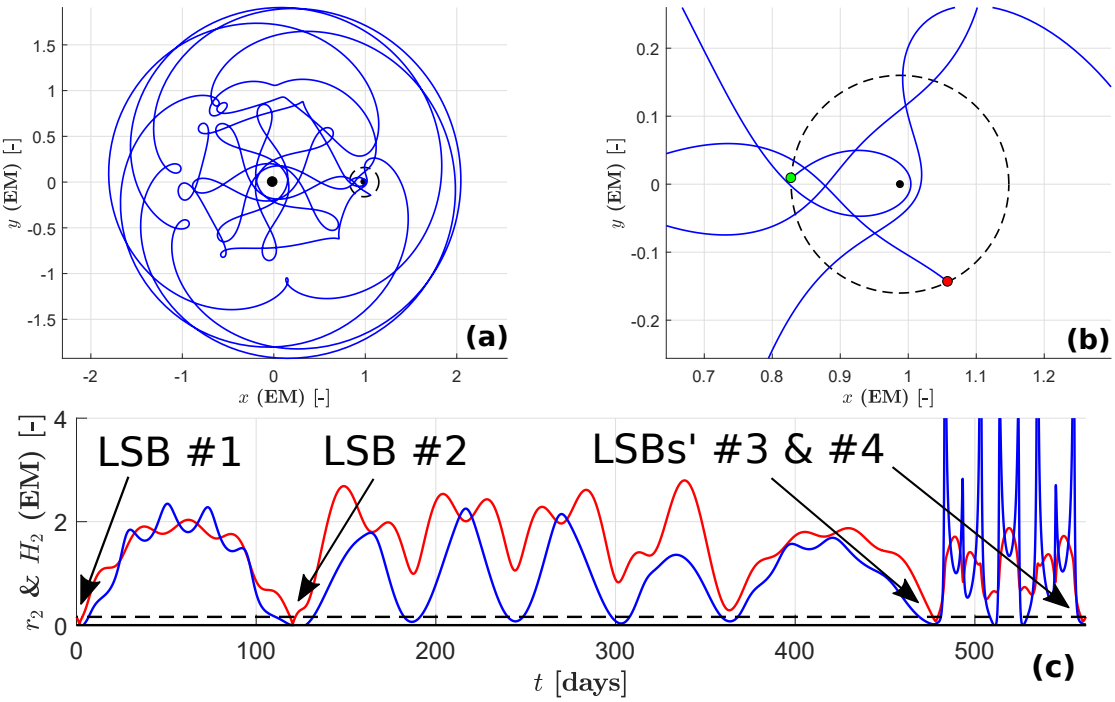

Figure 4.2: **(a)** Example of a sequence of three M2M transfers. Earth and Moon depicted as black dots, lunar Hill's sphere as a dashed circle about the Moon; **(b)** magnification of (a) about the Moon. Green and red dots marking the start and end of the trajectory, respectively; **(c)** trend in time of r_2 and H_2 (red and blue, respectively) for the trajectory highlighted in (a) and (b).

4.2. Controlled M2M transfer

In this section, the ballistic constraint is removed, to seek *controlled* M2M transfer, by means of an impulsive maneuvers. The structure is the following: in Section 4.2.1 two possible optimal strategies to *correct* a missing single M2M transfer are highlighted, while in Section 4.2.2 a sub-optimal iterative approach is outlined, to systematically retrieve a multiple M2M transfer.

4.2.1. Single M2M transfer

The underlying philosophy of this section is to properly correct the state using impulsive Δvs' in order to meet the M2M transfer requirements, by allowing a second fly-by with the Moon, otherwise missed.
The maximum Δv that can be considered as impulsive is taken as 5 m/s, referencing to EQUULEUS data [22]. The motivation behind this boundary can be explained by the following statement: a maneuver can be considered as impulsive if the path covered by the spacecraft in the time frame needed by its engine to actually perform that Δv is *negligible* with respect to the system scale. To support the previous statement, in Fig. 4.3 a collection of six different initial conditions is propagated (blue), for an amount of time derived from engine's characteristics, reported in Table 4.1. The propagation time is obtained accounting for an increasing $\Delta v = \{1, 5, 12\}$ m/s from Fig. 4.3a to Fig. 4.3c (left to right). A $\Delta v = 12$ m/s cannot be treated as impulsive even when the spacecraft is far from the main attractive bodies, while a $\Delta v = 1$ m/s can be approximated as impulsive even for trajectories close to Earth: a $\Delta v = 5$ m/s is found to be a possible optimal choice, especially for trajectories far enough from both primaries. This represents a really simple and short qualitative analysis, which is much more complex whereas one treats a real mission scenario. However, in order to obtain a fair upper boundary for the admissible Δv, this analysis is thought to be legitimate.

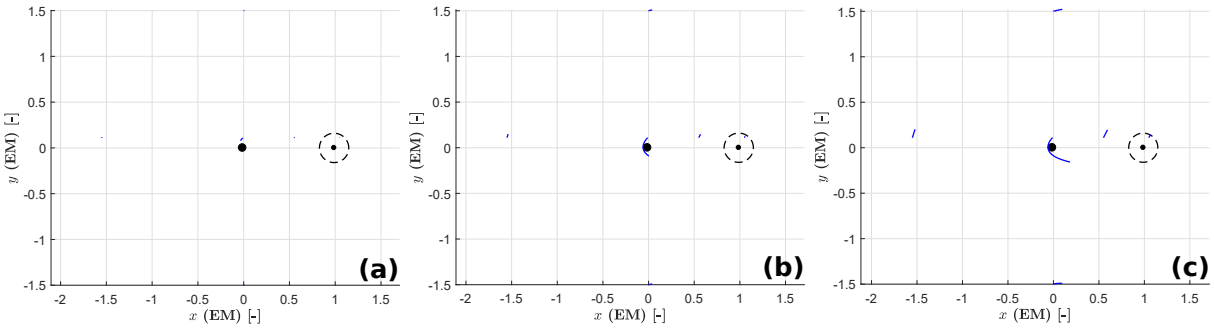

Figure 4.3: Different trajectories (blue) propagated for the amount of time needed by EQUULEUS engine ([22]) to perform a maneuver of **(a)** $\Delta v = 1$ m/s, **(b)** $\Delta v = 5$ m/s, **(c)** $\Delta v = 12$ m/s. Earth and Moon depicted as black dots, lunar Hill's sphere as dashed circle about the Moon.

I_{sp}	$M_{propellant}$	M_{wet}	$\bar{T}_{total}$	Δv budget
70 s	≈ 1.47 kg	< 14 kg	4 mN (100% duty cycle)	80 m/s

Table 4.1: EQUULEUS' engine characteristics ([22]). I_{sp} indicates the specific impulse, M the mass and $\bar{T}$ the thrust.

For what follows in this section two main optimizing approaches are discussed: a shooting technique with a fixed initial state is first studied, employing the Differential Corrector highlighted in Section 2.1.4 to adjust the initial state in order to meet the M2M transfer criteria. Successively, a more complex algorithm used to target a specific condition on a Poincaré cut is analysed, using MATLAB built-in function `fmincon`. Two equal example-trajectories are treated in both cases, in order to obtain a more general view either within and between the two strategies.

Shooting with fixed initial position

The Differential Corrector discussed in Section 2.1.4 is used to opportunely tune a certain state along the trajectory: a re-encounter with the lunar Hill's sphere, missed in the case of a purely ballistic approach, is achieved. Using the $\left(1^{st}\text{bw}, 2^{nd}\text{fw}\right)_{y+}$ intersections of the collision orbits, two points on the cut which are close to the *forward* set but properly far from the *backward* one are taken into account, in order to have, for

a limited propagation time, a trajectory encountering the lunar Hill's sphere just once, namely backward in time. Since the orbit is discretized in n different epochs, the idea is to have n different trajectories: each of the latter is equal to the unperturbed one up to the epoch where the impulse is applied. For every trajectory the impulse is applied once, at the t_i epoch, with $i \in \{1, 2, \ldots, n-1\}$. This gives a first fair idea on where to thrust in order to have an M2M transfer with the lowest consumption in terms of Δv. However, the initial part of the unperturbed trajectories is not here taken into consideration: indeed, flying close to the Moon enhances the weight of the nonlinear dynamics, therefore the assumption made for the derivation of the STM loses in terms of efficiency and the algorithm rapidly diverges.
The selected points on the cut are depicted in Fig. 4.4a, while the associated unperturbed trajectories are shown in Fig. 4.4b. The latter clearly miss the second lunar fly-by.

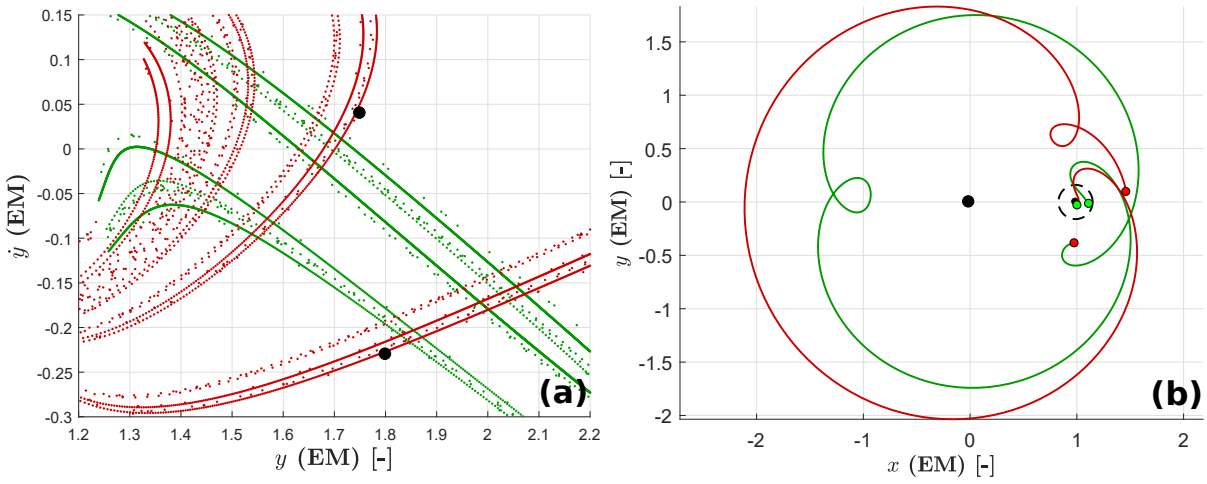

Figure 4.4: **(a)** location of the propagation points on the $\left(1^{st}\text{ bw}, 2^{nd}\text{ fw}\right)_{y+}$ Poincaré cut; **(b)** trajectories propagated forward and backward in time from the black dots in (a). Initial and final points marked by green and red dots respectively.

In order to retrieve at t_i the required Δv_i leading back to the lunar Hill's sphere, the STM $\Phi(t_i, t_n)$, which maps a perturbation from t_i to t_n, is defined thanks to Eq. (2.5) as

$$\Phi(t_i, t_n) = \Phi(t_0, t_n)\Phi(t_0, t_i)^{-1} \tag{4.1}$$

so that the equation which linearly maps a perturbation at the generic epoch t_i to a perturbation at epoch t_n becomes $\delta \boldsymbol{x}_n = \Phi(t_i, t_n)\delta \boldsymbol{x}_i$. The velocity components only, at epoch t_i, can be corrected in order to have a shift in final position at t_n. Therefore, only the up-right part of the 4×4 system of equations is taken into account, leading to the following set of equations

$$\begin{bmatrix} \delta x \\ \delta y \end{bmatrix}_n = \begin{bmatrix} \phi_{1,3} & \phi_{1,4} \\ \phi_{2,3} & \phi_{2,4} \end{bmatrix} \begin{bmatrix} \delta \dot{x} \\ \delta \dot{y} \end{bmatrix}_i \tag{4.2}$$

where $\phi_{k,j}$ is the (k, j)th term of $\Phi(t_i, t_n)$.
For this optimization, the cost function is set as a final distance from the Moon equal to 90% of the lunar Hill's sphere radius. Considering as $\boldsymbol{x}(t) = \phi(\boldsymbol{x}_i; t)$ the solution of Eq. (2.8), a radial unit vector $\boldsymbol{u}_r$, directed from the unperturbed final state $\boldsymbol{x}_n = \phi(\boldsymbol{x}_i; t_n)$ (whose distance from the Moon is $r_2(\boldsymbol{x}_n)$) to the Moon is constructed, so that the final shift in position is straightforward as

$$\begin{bmatrix} \delta x \\ \delta y \end{bmatrix}_n = \left[r_2(\boldsymbol{x}_n) - 0.9R_{Hill}\right] \boldsymbol{u}_r \tag{4.3}$$

Substituting Eq. (4.3) in the left-hand side of Eq. (4.2) and inverting the system, the equation of the impulse is obtained. Due to the nonlinearity of the problem, the steps mentioned above are iterated. Although being a really simple shooting algorithm, an optimization problem statement can be outlined as:

$$\begin{aligned} &\text{Find } \boldsymbol{y} = \left(\Delta v_x, \Delta v_y\right)_i, \text{ such that :} \\ &\left|r_2\left(\boldsymbol{x}_n\left(\boldsymbol{y}\right)\right) - 0.9R_{Hill}\right| \text{ is minimized} \end{aligned} \tag{4.4}$$

Where the cost function is now expressed in terms of the variable $\boldsymbol{y}$, thanks to Eq. (4.2).
A visual example of two corrected trajectories is reported in Fig. 4.5a, while the needed Δv (in terms of magnitude) versus the distance in time between the epoch at the impulse and the second encounter with the Moon is reported in Fig. 4.5b. In particular, the latter outlines how it is not straightforward to state *the sooner, the cheaper* for what concerns the impulsive maneuver: this is due to the involved nonlinear dynamics. None of the cases respects the 5 m/s boundary for the impulse: this is generally due to the trajectory under study, since using a different transfer which spends more time flying before the second lunar encounter usually leads to a lower corrective Δv. Both the unperturbed trajectories fall quite apart from the lunar Hill's sphere, as outlined by the red points in Fig. 4.4b as well as by the dashed curves in Fig. 4.5a: the resulting lowest impulse for a trajectory whose starting propagation point on the Poincaré cut was closer to the backward-propagated intersection set of the lunar ejection orbits (green in Fig. 4.4a) would have probably been less.

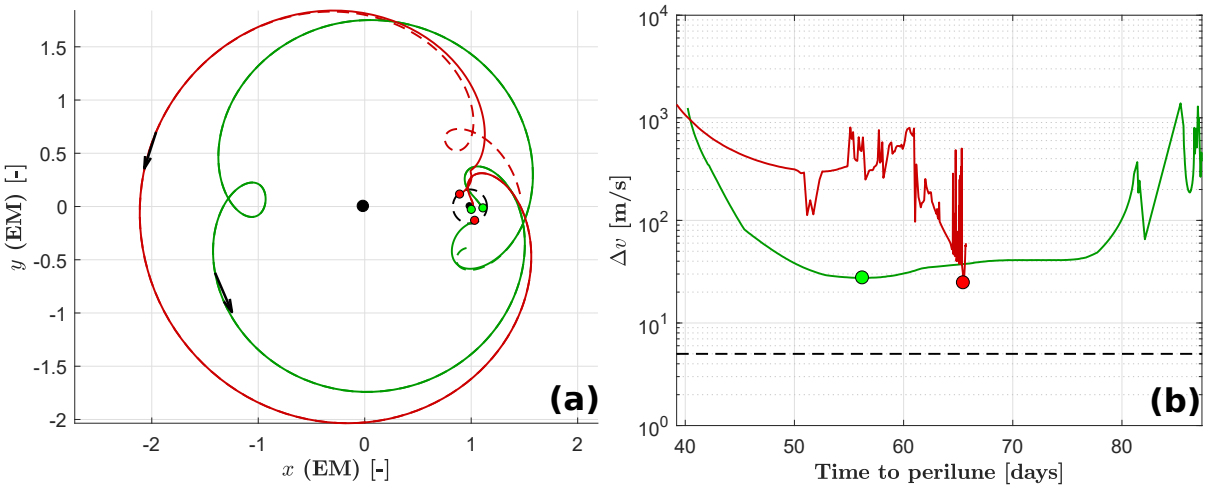

Figure 4.5: **(a)** Corrected trajectories (straight lines) compared to unperturbed ones (dashed lines). Impulses given by black arrows and magnified by a factor of 15. Initial and final state depicted as green and red points respectively; **(b)** Time of the impulse with respect to perilune vs magnitude of the impulse. Red and green points represent the plotted case in (a), as well as the minima for the corrected red and green dashed trajectories.

In conclusion, this approach may lead to feasible results in order to *recover* a proper M2M transfer from an otherwise single-flyby trajectory. However, few drawbacks are evident: first, the target condition cannot be sufficient, since aiming at a particular state, or a condition in terms of energy can be preferred; second, this approach loses in terms of effectiveness whereas the nonlinearities are enhanced; third, as previously indicated, the best results exceed the imposed boundary in Δv; fourth, a strategy with more than one impulse would be hard to properly set-up.
This approach represents one of the possible strategies to *recover* a properly defined M2M transfer. Other solutions may be preferred, for example targeting a fixed position at the end, as well as a different distance from the Moon or a certain condition on energy or angular momentum at the re-encounter. In any case, the same approach can be repeated when looking for a backward encounter with the lunar Hill's sphere, as well as a double one (both forward and backward): however, since this approach does not look promising in terms of Δv magnitude, every other possible implementation is here discarded.

Targeting the Poincaré cut

In this case, the yet-acquired knowledge of the intersections of the lunar ejection orbits with the Poincaré cut is employed in order to optimally correct a non-M2M transfer, making it comply with the specified M2M requirements. An initial point on the cut, similar to what is seen above, is selected, namely close to the *forward* set (red in Fig. 4.4a) but properly far from the *backward* one (green in Fig. 4.4a). By means of an impulsive maneuver, the optimization aims at correcting that intersection by reducing its gap with the backward set. For this reason, the same black dots in Fig. 4.4a are here used as an example: however, the optimizer seeks to correct with an impulse from the moment the unperturbed trajectory leaves the lunar Hill's sphere, so that the backward M2M requirement is always met. This because the optimizer, represented by MATLAB `fmincon` routine, has a softer linear approximation, despite what is done with the Differential Corrector. The

optimization problem statement is

$$\begin{aligned}
&\text{Find } \boldsymbol{y} = \left(\Delta v_x, \Delta v_y, t_{impulse}, t_{int}\right), \text{ such that :} \\
&100 * d([y, \dot{y}]_{int}, \text{P-cut}_{y,\dot{y}}) \text{ is minimized} \\
&\text{subject to :} \\
&t_{impulse} - t_{int} \leq 0, \quad x_{int} = 0 \\
&\begin{pmatrix} -\sqrt{1000}\,\text{m/s} \\ -\sqrt{1000}\,\text{m/s} \\ t_{0,unp} \\ t_{int,unp} - 0.5 \end{pmatrix} \leq \boldsymbol{y} \leq \begin{pmatrix} \sqrt{1000}\,\text{m/s} \\ \sqrt{1000}\,\text{m/s} \\ t_{int,unp} + 0.5 \\ t_{int,unp} + 0.5 \end{pmatrix}
\end{aligned} \tag{4.5}$$

The optimized variable $\boldsymbol{y}$ is different to what is reported in the former section: in particular, $\boldsymbol{y}$ is constituted by the components of the impulse $\Delta v_x, \Delta v_y$, the epoch at the impulse $t_{impulse}$ and at the intersection with the Poincaré cut t_{int}, which corresponds to the final propagation time for the optimized arc. The trajectory is then ballistically propagated from t_{int} onwards. The cost function is represented by the distance $d()$ on the $y\dot{y}$-plane between the intersection of the perturbed trajectory (i.e. the one obtained by applying the impulsive maneuver) with the Poincaré cut, and the closest point from the set of the intersections of the first-order backward-propagated lunar ejection orbits with the same cut, referred to in Eq. (4.6) as P-cut$_{y,\dot{y}}$ and shown in green in Fig. 4.4a. Since the optimization algorithm excels in efficiency whereas the cost function is close in magnitude to the unit value, the latter is increased by two orders of magnitude, due to the employed scale. Linear constraints are added on the epoch at impulse, occurring before the intersection with the cut, on the x-component of the state at the epoch of intersection (this forces the Poincaré cut piercing) and on the maximum admissible values of the different components of the variable $\boldsymbol{y}$. The unperturbed values of the epoch at the intersection with the cut and at the exit from the lunar Hill's sphere, respectively $t_{int,unp}$ and $t_{0,unp}$, are employed as reference for the time boundaries.
The boundaries for the Δv components exceed what stated for the maximum impulse; this is accepted in order to understand more in depth the behaviour of the optimizer, leaving it more freedom. An impulsive maneuver always causes a change in Jacobi constant $\bar{C}$, except when the impulse itself merely rotates the instantaneous velocity vector without changing its magnitude: this potentially causes a loss in validity for the utilized intersections of the ejection orbits P-cut$_{y,\dot{y}}$ for the computation of the cost function, since they are $\bar{C}$-depending. However, the impulse components are so low that a drastic change in $\bar{C}$ is not here achieved; this, combined with the almost negligible change in the shape of the intersections of the lunar ejection orbits with the Poincaré cut on the $y\dot{y}$-plane when $\bar{C}$ is slightly varied (discussed in Section 4.2.2) confirms the validity of the approximation. With the same unperturbed trajectories as depicted in Fig. 4.4b, the optimizing algorithm is applied: the results are reported in Fig. 4.6a.

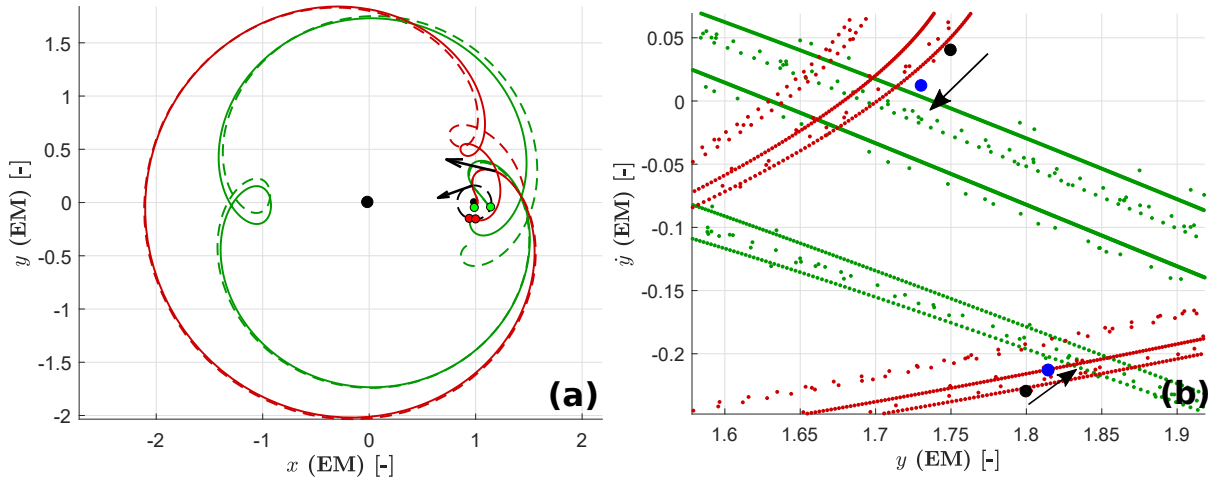

Figure 4.6: **(a)** Corrected trajectories (straight lines) compared to unperturbed ones (dashed lines). Impulses given by black arrows and magnified by a factor of 15. Relative impulses' magnitudes reported in Table 4.2. Initial and final state depicted as green and red points respectively. Red and green trajectories last for about 90 and 70 terrestrial days, respectively; **(b)** result of the optimizing algorithm in terms of piercing the Poincaré cut, from the unperturbed black dots to the optimized blue points.

As a result, the intersections of the transfers on the $y\dot{y}$-plane have shifted, as confirmed in Fig. 4.6b by the blue points. Both figures are obtained with a specific first guess, here not reported. The nonlinear dynamics makes the final optimized result highly dependant on the first guess. Indeed, for the identical problem statement highlighted in Eq. (4.6), but for other two different first guesses, the solution changes, as highlighted in Figs. 4.7a and 4.7b. The associated Δvs' are reported in Table 4.2.

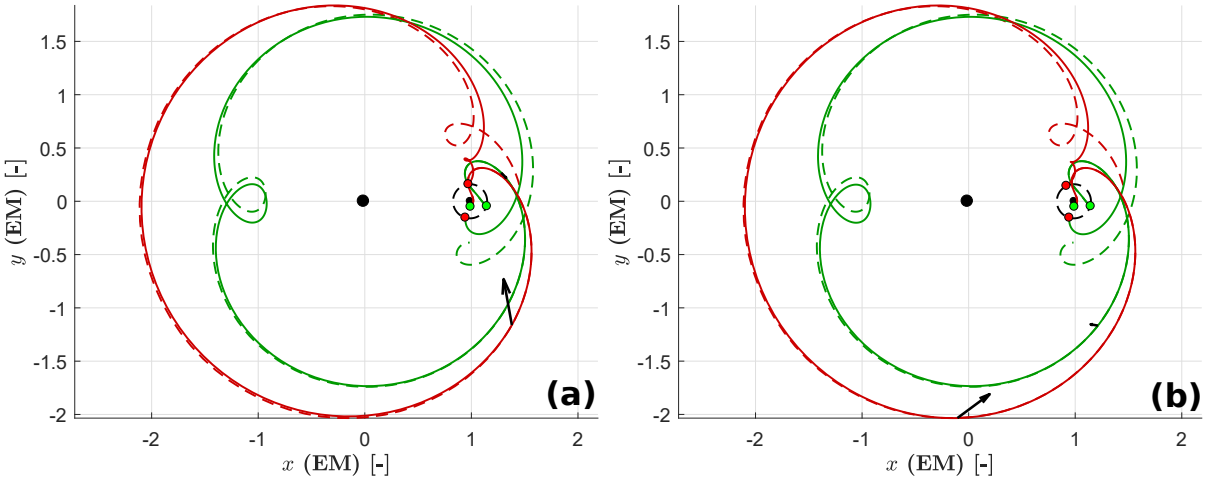

Figure 4.7: Corrected trajectories (straight lines) vs unperturbed ones (dashed lines). Impulses given by black arrows and magnified by a factor of 15. Impulses' magnitudes reported in Table 4.2. Initial and final state depicted as green and red points respectively. Red and green trajectories last for about 90 and 70 terrestrial days, respectively. Two different initial guesses used for **(a)** and **(b)**.

# Figure	Δv [m/s]	$\Delta\bar{C}$ [-]
Fig. 4.6a	Green: 23.5 - Red: 32.5	Green: -0.004 - Red: 0.027
Fig. 4.7a	Green: 4.62 - Red: 29.9	Green: -0.005 - Red: 0.053
Fig. 4.7b	Green: 4.78 - Red: 25.8	Green: -0.004 - Red: 0.060

Table 4.2: Δvs' and $\Delta\bar{C}$s' of the different optimized perturbed trajectories.

For some of the analysed cases, the results comply with the requirement of the maximum impulsive Δv. When this does not happen, a possible solution for lowering the corrective maneuver consists in splitting the total cost in a number of impulses $N > 1$. The new problem statement becomes

$$
\begin{aligned}
&\text{Find } \boldsymbol{y} = \left(\Delta v_{x,1}, \Delta v_{y,1}, \ldots, \ldots, \Delta v_{x,N}, \Delta v_{y,N}, t_{impulse,1}, \ldots, t_{impulse,N}, t_{int}\right),\\
&\text{such that :}\\
&100 * d([y,\, \dot{y}]_{int}, \text{P-cut}_{y,\dot{y}}) \text{ is minimized}\\
&\text{subject to :}\\
&t_{impulse,i} - t_{impulse,i+1} \leq 0 \quad \forall i \in \{1, 2, \ldots, N-1\}\\
&t_{impulse,N} - t_{int} \leq 0\\
&x_{int} = 0\\
&\begin{pmatrix} -\bar{V} \\ \vdots \\ t_{0,unp} \\ \vdots \\ t_{int,unp} - 0.5 \end{pmatrix} \leq \boldsymbol{y} \leq \begin{pmatrix} \bar{V} \\ \vdots \\ t_{int,unp} + 0.5 \\ \vdots \\ t_{int,unp} + 0.5 \end{pmatrix}
\end{aligned}
\tag{4.6}
$$

Without deepening in the criteria for selecting an optimum number of impulses as well as showing a comparison for different initial guesses, an example with two and five impulses is depicted in Figs. 4.8a and 4.8b

respectively, with supporting data in Table 4.3. $\bar{V} = 5$ m/s and $\bar{V} = 1.5$ m/s in Eq. (4.6) for the two- and five-impulses case respectively.

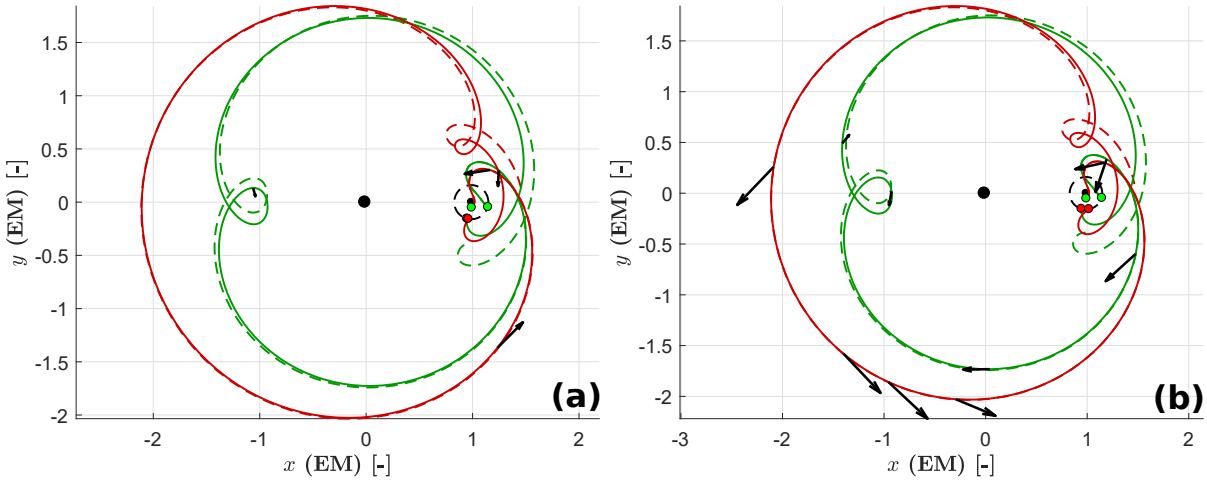

Figure 4.8: Corrected trajectories (straight lines) vs unperturbed ones (dashed lines). Initial and final state depicted as green and red points respectively. Red and green trajectories last for about 90 and 70 terrestrial days, respectively; **(a)** two impulses per trajectory, $\bar{V} = 5$ m/s, magnification by a factor of 50; **(b)** five impulses per trajectory, $\bar{V} = 1.5$ m/s, magnification by a factor of 300. Data reported in Table 4.3

# Figure	Δv_i [m/s]	Δv_{tot} [m/s]	$\Delta\bar{C}$ [-]
Fig. 4.8a	Green: (3.03 1.68) Red: (4.97 6.99)	Green: 4.71 Red: 11.96	Green: −0.002 Red: 0.020
Fig. 4.8b	Green: (1.17 1.37 0.90 0.47 0.37) Red: (1.01 1.46 1.80 1.82 1.77)	Green: 4.28 Red: 7.86	Green: −0.005 Red: 0.020

Table 4.3: Δvs' and $\Delta\bar{C}$s' of the different optimized perturbed trajectories in Fig. 4.8

As a conclusion, using more impulses allows to maintain the approximation discussed above. As shown in Table 4.3 it seems how the higher the amount of impulses is, the lower the total fuel consumption becomes: however, this happens for the particular cases here analysed, therefore no general conclusion can be delineated. All in all, the approach here described seems more efficient with respect to the previous one.

4.2.2. Multiple M2M transfer

In this section a potential strategy to derive a sequence of M2M transfers by using impulsive maneuvers is outlined.

In agreement with what is shown in the previous sections, a deep usage of the Poincaré cuts is here performed: however, dealing with impulses and multiple M2M transfers, the general view needs to be extended, in order to encompass a wider energetic domain. Indeed throughout this chapter every trajectory is conceived (or rather approximated, as in Section 4.2) with a fixed Jacobi constant $\bar{C}$: however, the latter is often changed in magnitude if an impulsive maneuver is performed. Therefore the intersections of lunar ejection orbits, computed for a range of different $\bar{C}$, with the Poincaré cut are employed as a framework to opportunely *guide* the state to achieve the main aim, namely building a sequence of M2M transfers.

A great difficulty lies underneath this problem: treating a sequence of M2M transfers is a very complex issue, due to the nonlinearities within the dynamical model, especially when passing by the Moon. This did not allowed the author to derive an efficient optimization strategy to correct a missing M2M transfer and, at the same time, set up the state for the next M2M transfer, within an iterative algorithm. Therefore, unless a very good first guess and a good solver are available, it is discouraged to optimize the sequence as a whole, in favour of an approach which singularly treats every M2M transfer.

As a consequence, in the remaining part of this section a sub-optimal approach is outlined in order to compute a multiple M2M transfer, by employing a *pile* of Poincaré cuts on the negative x-axis.

Jump the Poincaré cut

A *jumping*-strategy for the design of a multiple M2M transfer is here developed; the approach is held on a really basic level, due to the complexity of the problem.
Conversely to what is shown in this whole report, a different Poincaré cut is here employed, namely the negative x-axis: this does jeopardize the correctness of neither the final output of this section, nor the rest of the chapter. For the sake of simplicity, every impulse, if needed, is only applied when the state is located at the cut. The choice of the cut location is quite simple as well: although no optimization is sought, since the cut is on the furthest point from the secondary (namely the Moon), any impulse is *expected* to be near-optimum. In agreement with the previous theory, the intersections of the lunar ejection orbits are shown on the $x\dot{x}$-plane. In Fig. 4.9a the $\left(1^{st}\text{bw}\right)_{x-}$ intersections are depicted, for $\bar{C} \approx 2.963$, while in Figs. 4.9b to 4.9d the same intersections are reported, with the associated value of $\bar{C} \in \{2.930, 2.935, \ldots, 3.000\}$ on the $z-$axis. As previously suggested, the intersections slightly move on the $x\dot{x}$-plane according to a change in $\bar{C}$, while the shape seems to be maintained.

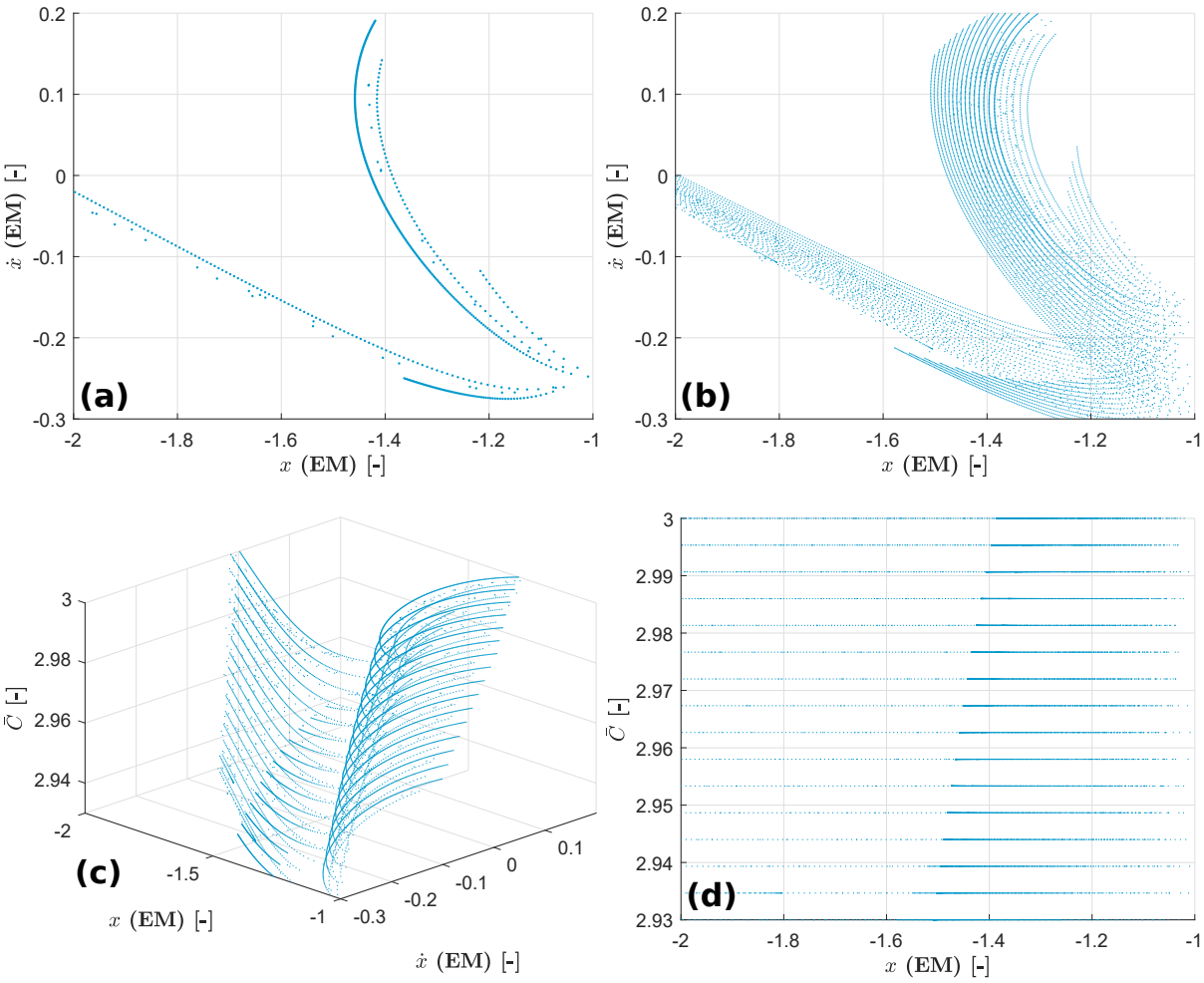

Figure 4.9: **(a)** first-order intersections of the backward-propagated lunar collision orbits with the cut at the negative x-axis, with $\bar{C} \approx 2.962$ and $\dot{y} \geq 0$; **(b)** top-view of a collection of intersections of first-order intersections of backward-propagated lunar collision orbits with the same cut as in (a), for a the range $\bar{C} \in \{2.930, 2.935, \ldots, 3.000\}$; **(c)** 3D-view of (b); **(d)** side-view of (b).

Using the knowledge from this *pile* of Poincaré cuts, a multiple M2M transfer can be designed, controlled by means of impulsive maneuvers.
In order to provide an example, a collection of points close to the $\bar{C} \approx 2.963$ intersections is propagated forward in time and successive intersections with the same Poincaré cut are stored; this means how higher order

encounters with the Poincaré cut may appear within the stored states. Later, if the latter fall within a certain region of the $x\dot{x}$-plane (selected to be a square encompassing the $\left(1^{st}\,\text{bw}\right)_{x-}$), they are perturbed by a Δv: the underlying idea is similar to what is discussed in Section 4.2, namely an impulse is provided so to reduce the gap between the state and the $\left(1^{st}\,\text{bw}\right)_{x-}$ intersections. Thanks to the results of Section 3.2.2, this ensures to meet the M2M transfer requirement when the (perturbed) state itself is propagated forward in time.
The used strategy to *fill the gap* with the cut is really basic and it does not employ any optimization scheme. In this method, a Δv augments the velocity components of the unperturbed state at the cut by means of two simultaneous maneuvers: an iso-$\bar{C}$ and/or a normal-$\bar{C}$ one. The former, found to be the less optimal among the two, consists in a movement of the intersection on a $\bar{C}$-fixed plane, along the $\dot{x}$-axis. This perturbation is added whereas the minimum gap between the unperturbed intersection and the $\left(1^{st}\,\text{bw}\right)_{x-}$ set at the same $\bar{C}$-level is larger than a certain threshold (set at 0.02 units): this represents an iso-$\bar{C}$ shift, which affects the $\dot{x}$-component of the state by two orders of magnitude more than the $\dot{y}$-one (which explains the lower optimality). The latter, namely the normal-$\bar{C}$ maneuver, is retrieved by a movement along the $\bar{C}$-axis (resulting in an iso-$\dot{x}$ maneuver), in order to carry the state towards the $\bar{C}$-plane where the associated $\left(1^{st}\,\text{bw}\right)_{x-}$ has the point with a minimal distance with respect to the unperturbed state.
One of the obtained output is shown in Fig. 4.10d. The path drawn by the successive intersections among the different cuts is shown in Figs. 4.10a to 4.10c.

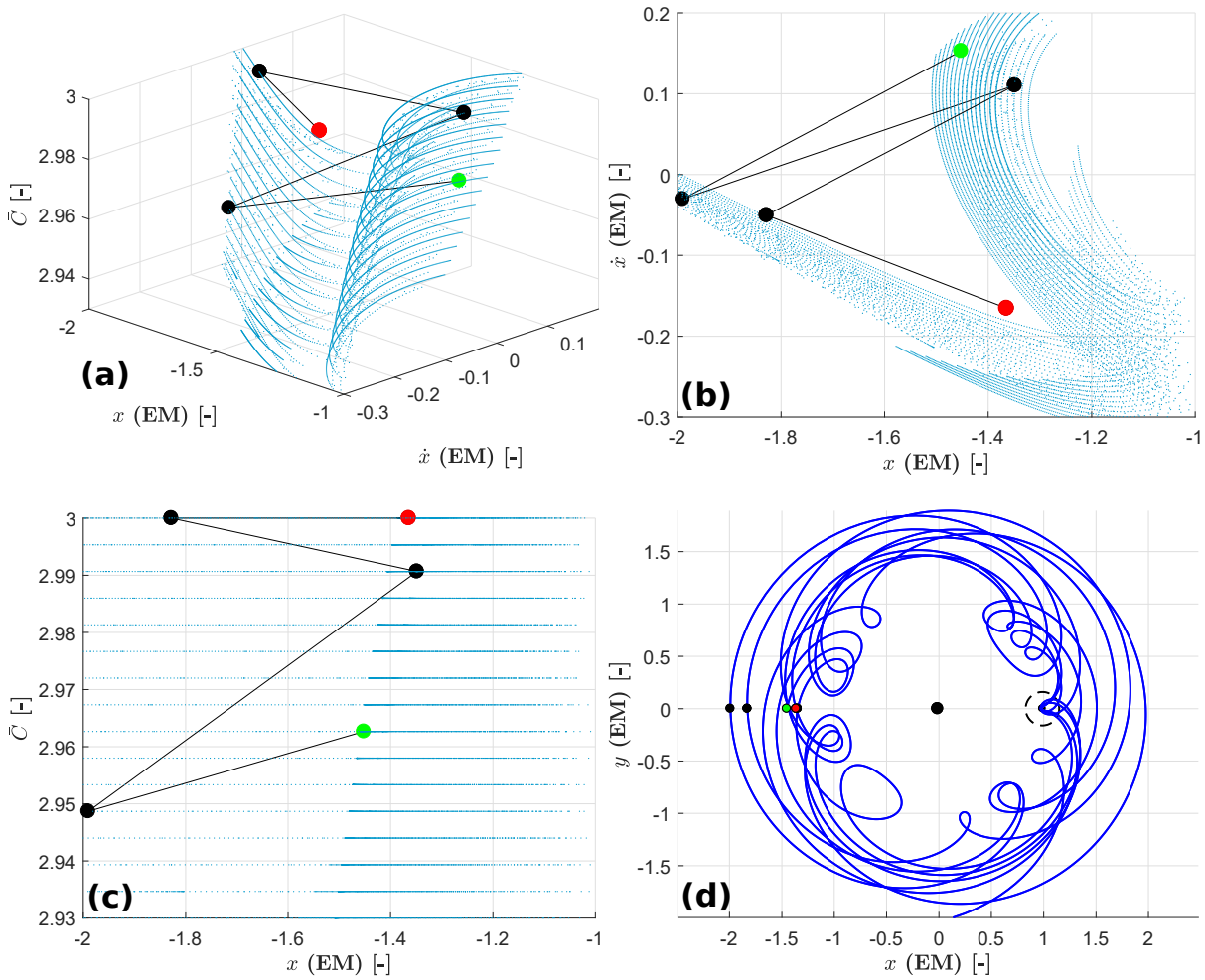

Figure 4.10: **(a)** Path among the different cuts of the perturbed trajectory in (d). Initial, mid and ending points marked in green, black and red; **(b)** top-view of (a); **(c)** side view of (a); **(d)** resulting trajectory (blue) from (a). Clearly notice the location of the start, mid and ending points (green, black and red) at the intersections with the cut.

Starting from the green intersections in Fig. 4.10a, the trajectory performs a triple M2M transfer (four black legs, five associated points) till it reaches the final red point. Every *jump* in the figure incorporates both the

propagation and the subsequent perturbation on the cut: this means every black segment links a perturbed state to the next perturbed one, namely after the subsequent maneuver at the cut, therefore often being at a different $\bar{C}$ value. Figs. 4.10b and 4.10c complete the example by showing the top- and side- view. In Fig. 4.11 the different impulses are clearly evident from the *jumps* in $\bar{C}$: the very last one is missing, since the transfer happens to be ballistic. In Table 4.4 data concerning the magnitude of the associated Δvs' are reported. It is evident how both the impulses and the time between lunar encounters are sub-optimal.

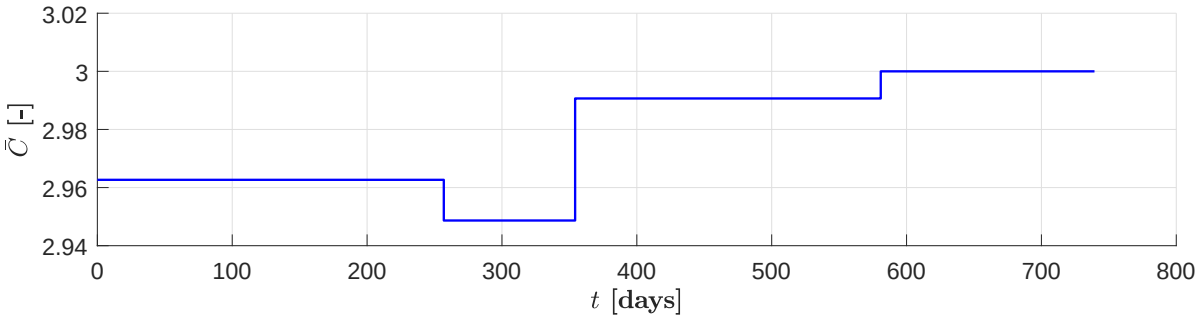

Figure 4.11: Trend of the value of $\bar{C}$ for the trajectory depicted in Fig. 4.10d. Notice how the last jump misses since no correction is needed.

#Impulses	1^{st}	2^{nd}	3^{rd}	4^{th}
Δv [m/s]	5.04	37.07	3.97	0 (ballistic)

Table 4.4: Characteristics of the impulses associated with the trajectory in Fig. 4.10d.

Although interesting, the method outlined in this section for multiple M2M transfer retrieval is highly dependant on the nonlinearities at the Moon: indeed few points among the initial collection of propagated intersections (coming from the $\bar{C} \approx 2.963$ cut, as reported above) manage to produce a high number of successive M2M transfers, since many diverge when leaving the lunar Hill's sphere. This is the same issue occurring when treating this problematic transfer on an iterative optimization scheme.

4.3. Conclusions

This section summarizes the main features of this chapter and provides both advantages and disadvantages of the employed methods.

In Section 4.1, a method to obtain ballistic multiple M2M transfers is discussed: by employing lunar collision orbits at different orders of encounter, dislocated regions on a common Poincaré cut are defined, whose points, once propagated, generate sequences of two and three ballistic M2M transfers. The survey stops at a certain order of encounter, although extending the results to obtain a larger sequence of M2M transfer is rather straightforward, as long as the nonlinearity does not hinder it.

The concept of a ballistic M2M transfer is then extended. In Section 4.2.1 two different strategies, employing optimized impulses, are used to *recover* from a missing single M2M transfer. Studies with the Differential Corrector scheme show worse results when compared to what is obtained with MATLAB `fmincon` routine. Although it is not shown here, the optimization algorithm can be opportunely tuned in order to meet a different specific condition, for example a final energy or angular momentum. As a further extension, a method to obtain sequences of corrected M2M transfer is highlighted in Section 4.2.2. A *pile* of Poincaré cuts is employed to steer the progressive intersections of the trajectory, in order to meet the M2M requirements. Only sub-optimal solutions can be retrieved, which can be used as first guesses for a subsequent optimization.

Being a conclusive section before dealing with a more refined dynamical model, a general overview of the obtained results is now outlined. The outcome is limited by the intrinsic nature of the dynamical model: indeed, by taking into account the presence of the Earth and the Moon only, therefore discarding the gravitational influence of the Sun, the trajectories are sufficiently precise whereas they do not exceed a certain region about the Earth–Moon system. Fixing a strict boundary is either hard and useless, since the solar influence may vary depending on the problem geometry: however, in the existing literature usually a limit of $\approx 1.5(EM) = 576607.5$ km about the Earth–Moon barycentre is defined, corresponding to less then Earth's SOI

(Qi and Xu [24]). Therefore this entire analysis is enough precise whereas trajectories do not largely exceed this boundary.
The used approach has another important drawback: indeed, according to the given definition of the M2M transfer, the latter may not have to cross the cut in order to comply with the requirements. A looping behaviour close by the Moon can correctly fulfil the latter: for example, even though being quite an extreme case, an HLO about either L_2 or L_1 with the proper level of energy can be classified as an M2M transfer, although it does not cross the positive y-axis cut. In Chapter 5 this concept is extended.
Concluding, last two chapters show new methods to construct both single and multiple M2M transfers, in either a ballistic or corrected approach, by exploiting existing and acquired knowledge of lunar collision orbits. To the best of author's knowledge, this kind of trajectories has never been actively employed for preliminary trajectory design.

5

M2M transfer in the Sun–Earth–Moon BR4BP

In this chapter, Moon-to-Moon transfers are studied in a more complex dynamical model than what is used in Chapters 3 and 4. Indeed, the planar Sun–Earth–Moon Bi-circular Restricted Three Body Problem (BR4BP) is here employed. In this case, Earth and Moon, namely P_1 and P_2 move in a circular orbit about their common centre of mass, while the Sun, referred to as P_S, revolves in a circular orbit about the latter point. The problem is simplified once compared to the real dynamics of the involved bodies: however, inaccuracies are quite slight, as supported by Table 2.2.
The chapter is divided in four parts: in Section 5.1 the main aspects of the new dynamical model are compared to the CR3BP, while in Section 5.2 the two main strategies to obtain single M2M transfers are highlighted. In Section 5.3 the latter topic is complicated by referring to sequences of M2M transfers, concluding with the final assessments in Section 5.4.

5.1. BR4BP analysis

First of all, it is important to properly define how lunar ejection orbits are propagated in this chapter; a Levi Civita regularization scheme for the BR4BP is not present in the existing literature, therefore the overall propagation scheme, used throughout this whole chapter, acts as follows

$$\begin{cases} \text{for } \|\boldsymbol{x}-\boldsymbol{x}_{Moon}\| \leq R_{Moon} & \longrightarrow \quad \text{Levi Civita CR3BP scheme} \\ \text{for } \|\boldsymbol{x}-\boldsymbol{x}_{Moon}\| > R_{Moon} & \longrightarrow \quad \text{Cartesian BR4BP scheme} \end{cases} \tag{5.1}$$

where again $\boldsymbol{x}$ represents the state of the spacecraft, $\boldsymbol{x}_{Moon} = (1-\mu, 0)$, while R_{Moon} is the radius of the Moon. This further sustains the choice of switching from the regularized to the Cartesian scheme for the CR3BP model too, as reported in Section 3.1: indeed, this eases a potential comparison between the two dynamical models when treating lunar collision orbits. For the sake of correctness, even though almost negligible when the state is within lunar surface, the trend in time of solar phase angle θ_S is tracked. The approximation of the dynamical model for the propagation part within the Moon does not hinder the truthiness of the derived trajectory: indeed the state is almost at the centre of lunar SOI when propagated with the CR3BP Levi Civita scheme, therefore the motion of the spacecraft is completely influenced by the gravity of the Moon only, while negligibly from both Earth and Sun.
Before starting with the description of the approaches used to retrieve M2M transfers in the BR4BP, it is necessary to understand to what degree is the BR4BP dynamical model different from the CR3BP one. For this purpose, Fig. 5.1 shows two trajectories, propagated in time according to the CR3BP (dashed red) and the BR4BP (straight blue) model. The only difference between the two figures, is that an inbound lunar ejection angle θ_E, with respect to the ZVC, is selected for the trajectories in Fig. 5.1a while an outbound one in Fig. 5.1b. Within the same figure, trajectories are propagated with exactly the same initial condition. In Fig. 5.1b the ZVC is pierced by the orbit propagated with the BR4BP model (straight blue curve): this further confirms the lack of a Jacobi integral in its dynamics, implying the existence of a rather time-pulsating ZVC.
Although a comparison based on few orbits is definitively not enough for obtaining a rigorous discernment

between the two models, Fig. 5.1 catches the main elements of this difference, in agreement with what stated in Section 4.3: the 1.5 (EM) limit (roughly 5.7×10^5 km), taken as a boundary between the CR3BP and the BR4BP dynamical predominance, is confirmed. Indeed, trajectories in Fig. 5.1a stay in the inner zone of the ZVC, therefore their distance from the centre of the reference frame does not exceed the limit, weakening the effect of Sun's gravitational pull down: as a result, these two orbits remain quite aligned, although propagated with different dynamical models. The same cannot be inferred for Fig. 5.1b where the two orbits largely diverge since they experience a stronger perturbation from the Sun, due to the motion in the outer region. Henceforth the ZVC concept is discarded, due to its evident lack of meaning for trajectories propagated in the BR4BP.

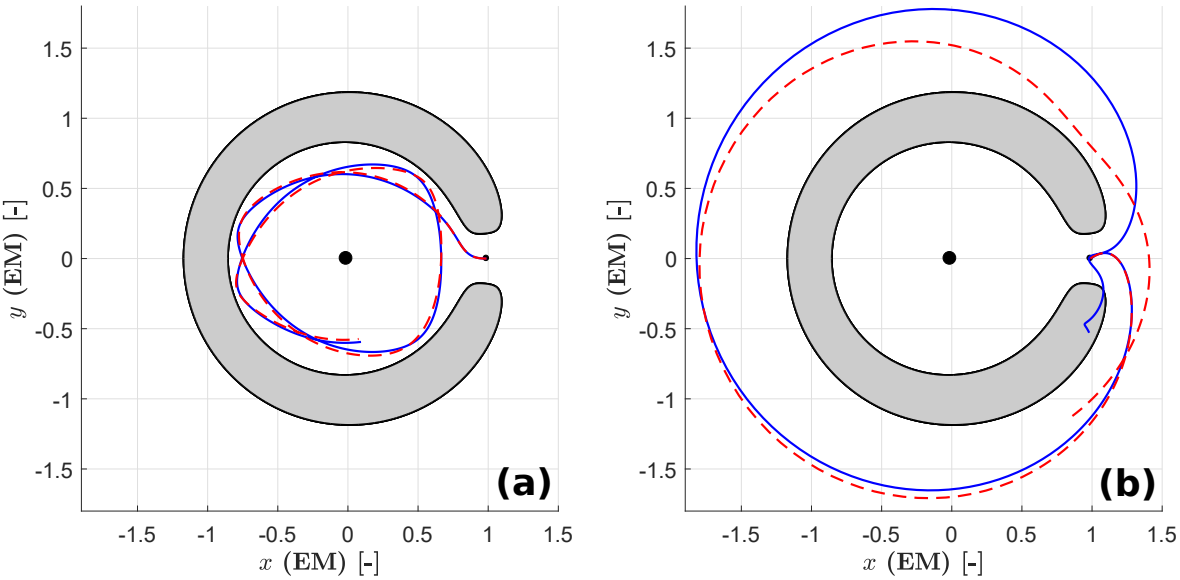

Figure 5.1: Lunar ejection orbits propagated for ≈ 65 days with the BR4BP and CR3BP dynamical models (straight blue and dashed red, respectively) with an equal initial $\bar{C}$ for an **(a)** inbound and **(b)** outbound initial Sun's phase angle θ_{S0}. ZVC depicted in grey, while Earth and Moon as black dots. Synodic barycentric reference frame.

As a subsequent step, the influence of the initial solar phase angle θ_{S0} on the trajectory is highlighted. For this analysis, two different initial conditions, marked by different ejection angles θ_E and equal Jacobi-constant value $\bar{C}$ for the lunar ejection orbits are selected, similarly to what is done in Fig. 5.1. Different initial solar phase angles θ_{S0}, ranging $0 \leq \theta_{s0} < 2\pi$ are used, and coded accordingly with a blue-to-red scale, as plotted in Figs. 5.2a and 5.2b.

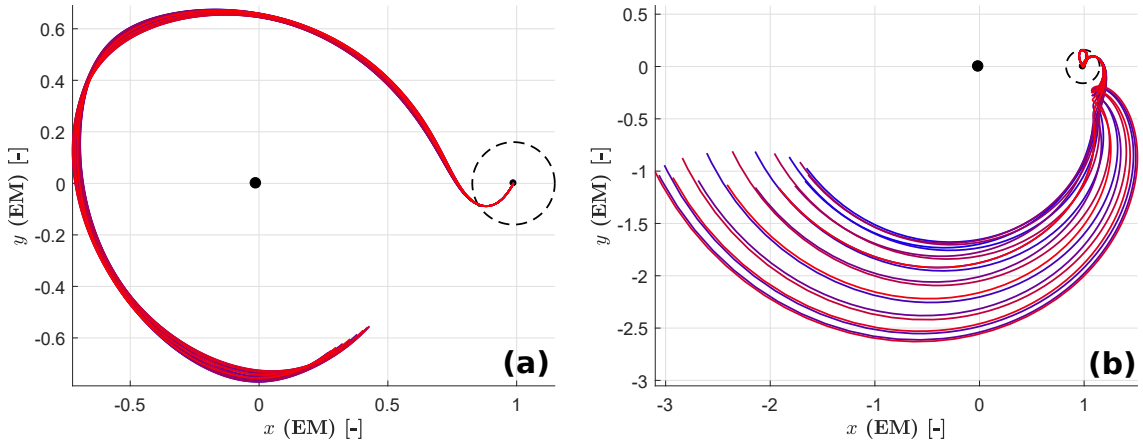

Figure 5.2: Lunar ejection orbits propagated for ≈ 30 days with the BR4BP dynamical model, with an increasing initial Sun's phase angle θ_{S0} (from red to blue); **(a)** inbound initial ejection angle; **(b)** outbound initial ejection angle. Earth and Moon depicted as black dots, while lunar's Hill's sphere as dashed black circle. Synodic barycentric reference frame.

It is again remarkable from Fig. 5.2a how Sun's influence is almost negligible in the inner part of the Earth–Moon system. There is no direct correlation between Sun's initial position and distance of the orbit from the system, according to Fig. 5.2b for the external case. Aligned with what is mentioned above, two examples are not fully representative to discern the main characteristic of the involved models, although they help in defining important qualitative characteristics. A similar analysis, for a collection of M2M transfers, is shown in Section 5.2.2.

5.2. Single M2M transfer

In this section, the concept of single M2M transfer is analysed with the BR4BP dynamical model, analogously to what is explained in Section 3.2 with the CR3BP one. Two different procedures are here highlighted: in Section 5.2.1 an approach similar to what is described in Section 3.2.1 for the CR3BP is outlined, while in Section 5.2.2 a completely different strategy is pointed out to obtain an unconventional (or rather *quasi*-) M2M transfer, leading to a classification of double-collision orbits.

5.2.1. M2M transfer with a pseudo-Poincaré cut

A similar approach to what is performed in Section 3.2.1 for the CR3BP dynamical model is here developed, in order to compute an M2M transfer in the BR4BP: orbits are propagated from lunar centre, set at $(x, y) = (1-\mu, 0)$ in the synodic barycentric frame, according to the scheme sequence pointed out in Eq. (5.1), and their intersections with a Poincaré cut are stored, analysed and used for obtaining the M2M transfers.
One of the most important differences between the CR3BP and BR4BP is the nonautonomous characteristic of the latter; no first integral can be delineated for this model, as outlined in Section 2.2.2, which implies the impossibility of obtaining the unique state $\boldsymbol{x}$ and therefore the unique trajectory out of it, by taking a point on the bidimensional projection of a well-defined Poincaré cut, as it is performed in Chapter 3.
Therefore, the intrinsic usefulness of a Poincaré cut is here limited. However, a Poincaré cut can still be used as a mere order reductant of the dimensionality of the problem. With the only purpose of discerning what is treated in this section to what is extensively employed in Chapters 3 and 4, a *pseudo*-Poincaré cut is defined. The latter remains a semiaxis, in particular for this analysis the positive y-axis, in order to remain aligned with Section 3.2.1.
A new set of points to shortly indicate the intersections of the lunar collision orbits with the cut is here introduced: the former is referred to as $S^{j}_{k,i} \subset D = \{\mathbb{R}^2 \times [0, 2\pi)\}$, where $i = \{bw, fw\}$, the order-encounter $k \in \mathbb{N}^+$ and $j = \{\theta_{S0,1}, \theta_{S0,2}, \ldots\}$. Due to the adjunct timewise variable θ_S, the state has now increased its dimensionality by one element, therefore, although not encompassing every variable, a 3D-representation of the intersections of the lunar ejection orbits with the cut is here employed, with the generic point expressed with the triple $(y, \dot{y}, \theta_S)$. The approach now aims at finding a set $\mathscr{G}$ within the cut where two elements $\boldsymbol{x}_{fw} \in S^{\theta_{S0,2}}_{2,fw}$ and $\boldsymbol{x}_{bw} \in S^{\theta_{S0,1}}_{1,bw}$ are close enough ($\theta_{S0,1}$ may be different from $\theta_{S0,2}$). In this case, the two sets are defined as the set of the first-order intersections of the backward-propagated ejection orbits, with a starting solar phase angle $\theta_{S0,1}$ and the set of the second-order intersections of the forward-propagated lunar ejection orbits, with a starting solar phase angle $\theta_{S0,2}$, respectively with the positive $y-$axis: in agreement with what is discussed in Chapter 3, the combined presence of the two sets can be referred to as $\left(1^{st}\mathrm{bw}_{\theta_{S0,1}}, 2^{nd}\mathrm{fw}_{\theta_{S0,2}}\right)_{y+}$. In this case, the set $\mathscr{G}$ mentioned above consists in

$$\mathscr{G} = \left\{\boldsymbol{x}^*_{2,fw} \in S^{\theta_{S0,2}}_{2,fw} : A^* \neq \varnothing\right\} \tag{5.2}$$

where for every $\boldsymbol{x}^*_{2,fw}$, the associated A^* is defined as

$$A^* = \left\{\boldsymbol{x}_{1,bw} \in S^{\theta_{S0,1}}_{1,bw} : d\left(\boldsymbol{x}^*_{2,fw}, \boldsymbol{x}_{1,bw}\right) < 1\right\} \tag{5.3}$$

and the distance function is $d : D^2 \to \mathbb{R}$, such that

$$d(\boldsymbol{x}_1, \boldsymbol{x}_2) = \frac{(y_1 - y_2)^2}{r_y^2} + \frac{(\dot{y}_1 - \dot{y}_2)^2}{r_{\dot{y}}^2} + \frac{(\theta_{S,1} - \theta_{S,2})^2}{r_{\theta_S}^2} \tag{5.4}$$

where $(r_y, r_{\dot{y}}, r_{\theta_S})$ are the semiaxes of an ellipsoid for the three treated variables, whose tuning is θ_{S0}-depending. In the case here pointed out, a value of 0.02 is used for every semiaxis.

For every element of the set $\mathscr{G}$, the initial point of propagation is obtained by linearly interpolating between every *couple* $(\boldsymbol{x}_{fw}, \boldsymbol{x}_{bw})$ satisfying Eqs. (5.2) and (5.3). The procedure involves a linearization with respect to the coordinate $\dot{x}$ too, which cannot be retrieved by the Jacobi constant, as performed in the CR3BP case.
This method, although incomplete since the four-dimensionality of the problem is not thoroughly covered, is solved with this approach due to the large computational time a 4D grid search would require.
A result of this analysis, for the simple case $\theta_{S0,1} = \theta_{S0,2} = 0$ deg, is plotted in Figs. 5.3a and 5.3b for the 3D- and top-view respectively, showing with the usual colors the $\left(1^{st}\,\mathrm{bw}_0, 2^{nd}\,\mathrm{fw}_0\right)_{y+}$ intersections of the collision orbits with the positive y-axis Poincaré cut. The forward-propagated set of intersections is obtained by the backward-propagated one (at a different order encounter) by employing the time symmetry highlighted in Section 2.2.2. The set $\mathscr{G}$ is here evident by the black disconnected points, while the cyan ones represent the actual M2M transfers. To provide an example, one simple M2M transfer is here shown: in Fig. 5.4a the trajectory is depicted in the synodic frame, while in Fig. 5.4b in the Earth-centered inertial one. As usual, green and red points mark the start and end of the trajectory, respectively.

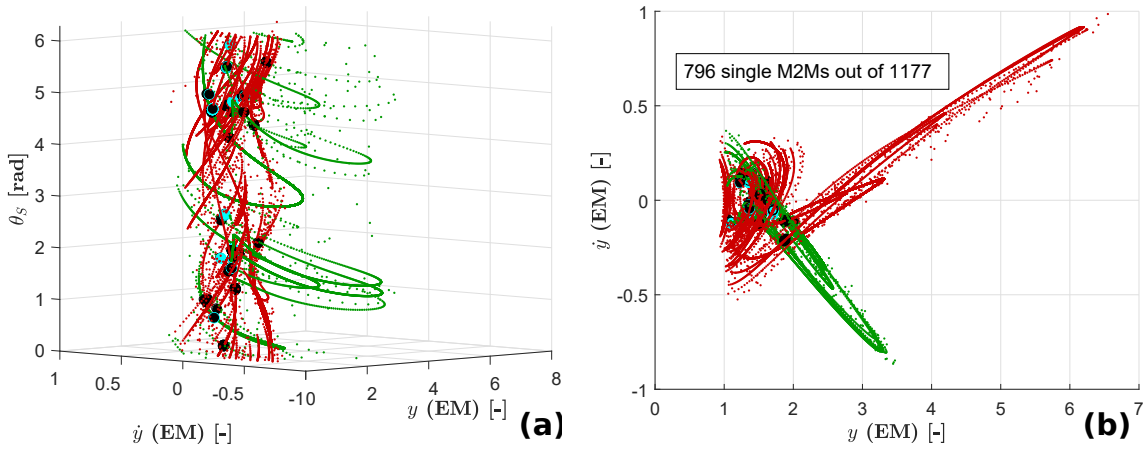

Figure 5.3: $\left(1^{st}\,\mathrm{bw}_0, 2^{nd}\,\mathrm{fw}_0\right)_{y+}$ intersections (green and red respectively) with the Poincaré cut on the positive y-axis, with $\dot{x} \geq 0$, $\bar{C}_0 = 2.97$. Black points representing the ones satisfying Eqs. (5.2) and (5.3), while cyan ones the one where actual M2M transfer are propagated from; **(a)** 3D-view; **(b)** top-view.

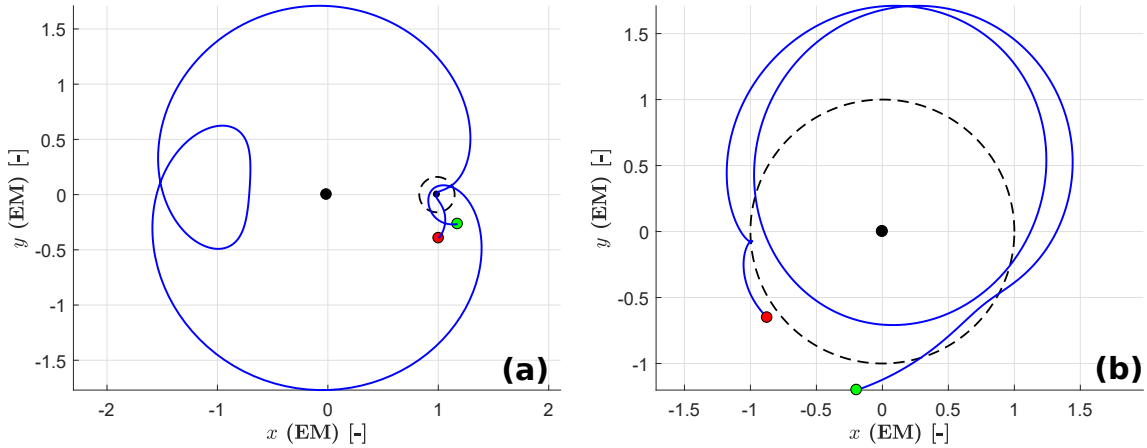

Figure 5.4: One example M2M transfer out of the obtained 796 results in Fig. 5.3; **(a)** synodic barycentric reference frame. Earth and Moon depicted as black dots, lunar Hill's sphere as black dashed circle about the Moon; **(b)** Earth-centered inertial reference frame. Lunar orbit depicted as dashed black line. Starting and ending point marked as green and red dots respectively.

The obtained percentage of M2M transfers, out of the totality of candidate points (more than 67%), clearly highlights the feasibility of this approach for obtaining a single M2M transfer in the BR4BP. However, the study is consistently harder to handle with respect to what seen for the CR3BP, since a slightly different initial angle θ_{S0} leads to different intersections on the cut. Moreover, the *mathematical beauty* given by the Jacobi constant cannot anymore be leveraged.

5.2.2. M2M transfer from double-collision orbits

In this section, a different approach for obtaining an M2M transfer in the BR4BP is described and analysed. Due to the impossibility to completely define the state by using a 3D-representation on a Poincaré cut (the fourth coordinate, $\dot{x}$, is obtained using a trick in Section 5.2.1), the latter is used to define an M2M transfer in a direct way, rather than employing an intermediate patching.
Ejection orbits are once again propagated from the Moon, accounting for the switch in the dynamical model highlighted in Eq. (5.1). The positive x-axis is now used as *cut* for the analysis: in particular, the study focuses on the intersections of lunar ejection orbits falling within an area close to the Moon, namely $x \in [1-\mu-R_{hill}; 1-\mu+R_{hill}]$ in the synodic barycentric frame, where R_{Hill} is the lunar Hill's sphere radius. This automatically gives an M2M transfer if the condition of lunar surface-hitting is discarded, although maintaining the other one; therefore the trajectories here analysed are referred to as *quasi*-M2M. They can be subsequently used as a first guess for obtaining a properly defined M2M transfer, although this is not treated in this report.
These *quasi*-M2M transfers, aside from helping in the definition of an M2M database discussed in Section 5.3.2, have shown a quite rich structure, accounting for their shape as well as for their location at the intersection with the cut. For this reason, in the remaining part of this section, their classification is discussed.

Orbit classification

Following from what is stated above, *quasi*-M2M transfers are here classified based on their shape and the number of encounters with the Poincaré cut of radius R_{Hill} in a neighbourhood of the Moon, set on the $x-$axis. The intersections are reported on the $x\dot{y}$-plane. The trajectories are propagated from the intersection with the $x-$axis forward in time, towards the collision with Moon's center. An initial solar phase angle of $\theta_{S0} = \pi/2$ is used throughout this section; nevertheless, a similar approach can be applied to a different case, bringing slightly different results. *Quasi*-M2M transfers are classified based on the encounter order with the cut, as labelled in what follows.

First encounter: In this case, really simple *quasi*-M2M transfers are shown: their location on the cut is depicted in Fig. 5.5a, which subdivides the trajectories in four main families, reported in Fig. 5.5b.

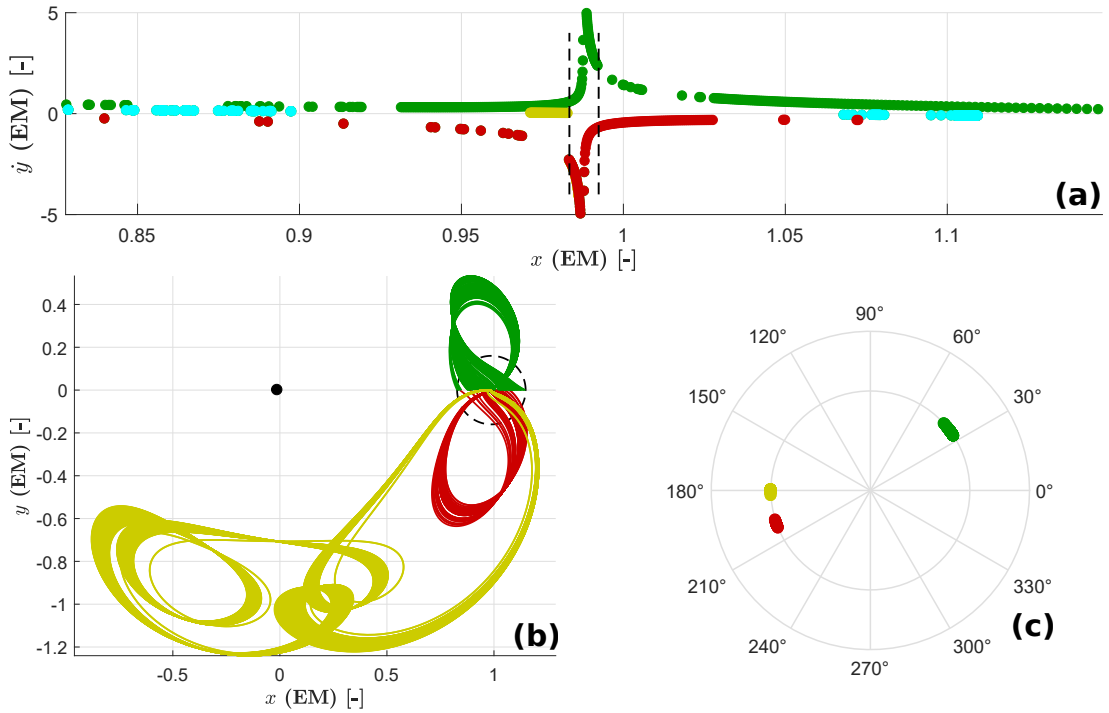

Figure 5.5: First-order intersections with the Poincaré cut on the x-axis for $x \in [1-\mu-R_{hill}; 1-\mu+R_{hill}]$ of lunar ejection orbits. Initial condition $\theta_{S0} = \pi/2$, $\bar{C}_0 = 2.97$; **(a)** view of the intersections of the ejection orbits with the cut in the $x\dot{y}$-plane. Lunar surface depicted as dashed black lines. See the classification in four different families; **(b)** shape of the different families. The cyan one is not reported since meaningless; **(c)** initial lunar collision angles for the different families.

The final ejection angle θ_E for every component of each family is depicted in Fig. 5.5c. Families are discerned by their shape; no elements from the fourth family (cyan in Fig. 5.5a) is reported in Fig. 5.5b since they do not pierce the Hill's sphere. For every family, the intersections with the cut resembles a hyperbola centered on the Moon: this is due to the singularity at this location (i.e. the Moon, $(x, y) = (1-\mu, 0)$), which causes a severe increase of both components of the velocity when approaching it. A similar behaviour can be observed in the $x\dot{x}$-plane, here not reported. Referring to Figs. 5.5b and 5.5c, it can be inferred how Sun's gravitational pull helps in destroying the symmetry between family-1 and -2 orbits (green and red, respectively). Family-3 (in yellow) represents the long-time class of first-encounter *quasi*-M2M transfers.
From Fig. 5.5c it can be noted how each first-order encounter family is positioned on a low range of ejection angles θ_E: this aspect can largely tighten the initial coarse grid search, if seeking a specific family.

Second encounter: In this case the *quasi*-M2M transfers are obtained by propagating second-order encounter ejection orbits with the Poincaré-cut back to lunar central impact. Again, the intersections are reported on the $x\dot{y}$-plane in Fig. 5.6.

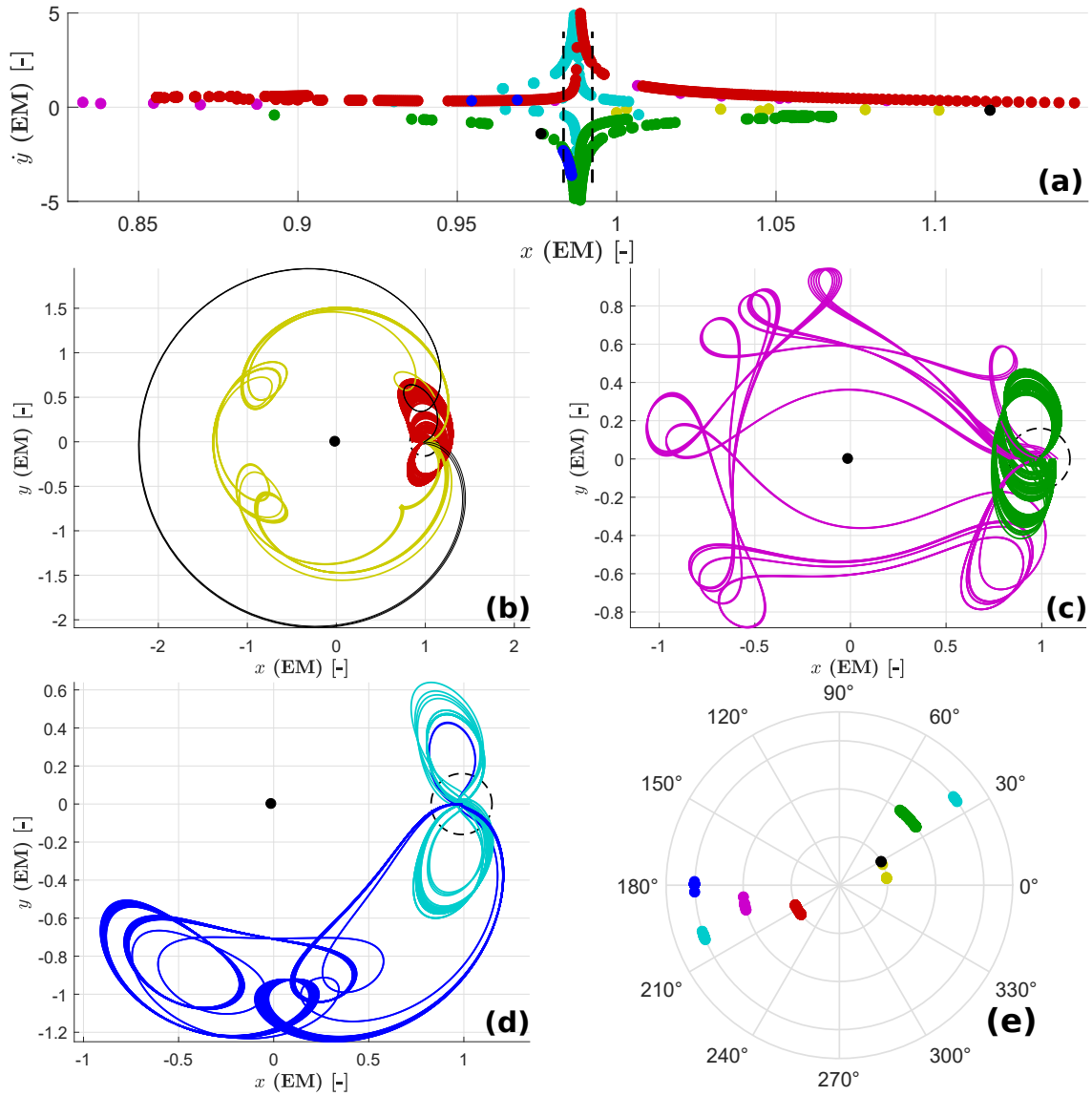

Figure 5.6: Second-order intersections with the Poincaré cut on the x-axis at $x \in [1-\mu-R_{hill}; 1-\mu+R_{hill}]$ of lunar ejection orbits. Initial condition $\theta_{S0} = \pi/2$, $\bar{C}_0 = 2.97$; **(a)** view of the intersections of the ejection orbits with the cut in the $x\dot{y}$-plane. Lunar surface depicted as dashed black lines. See the classification in seven different families; **(b)**, **(c)** and **(d)** shape of the different families; **(e)** initial lunar collision angles for the different families.

Figure 5.6a shows the location and subdivision of the different families based on their shape, while Figs. 5.6b to 5.6d give a representation of the associated propagated *quasi*-M2M transfers: in Fig. 5.6e one can find their culminating ejection angles. From Fig. 5.6a it is evident how family-1 and -2 of first-order encounter transfers (green and red in Fig. 5.5b), are in part translated in family-4, -5 and -6 (green, red and cyan respectively) of the second-order encounter, which are mimicking HLOs about L_1, L_2 and the direct satellite orbits about the secondary, respectively. These three families of *quasi*-M2M transfers find their counterpart in Hénon [10], although referred to as family-a, $-c$ and $-g$ (high energies version), respectively. However, in his work Hénon obtained these three families of periodic orbits with a simpler dynamical model, defined as *Hill's* problem for $\mu \to 0$, within the theory of the CR3BP. The family-3 in the first-encounter class (yellow in Fig. 5.5b) is again observable in Fig. 5.6d, while three new families of long orbits appear, respectively in magenta, yellow and black in Figs. 5.6b and 5.6c: the first one is located almost exclusively within Moon's orbit about the Earth (roughly one unit radius about the origin of the synodic frame), while the other two spend most of their time out from this boundary.

Successive encounters: From the second encounter onwards, the amount of families starts to rapidly grow. Although maintaining an hyperbolic-like structure about the point $(x, y) = (1-\mu, 0)$, the location of the *quasi*-M2M transfers on the cut starts to lose any reasonable pattern. As an example, the cut at the fourth encounter is shown in Fig. 5.7a. In particular, the fourth-encounter *quasi*-M2M transfers show the presence of another member of the family-g' from Hénon [10], depicted in Fig. 5.7b. Similar orbits have been found for different solar starting phase angles θ_{S0}.

Coming to a conclusion for orbit classification, the performed analysis can provide a useful insight in the catalogue of *quasi*-M2M transfers: as previously demonstrated, some family is the perturbed and aperiodic counterpart of orbits centered at the secondary, which can be found in the existing literature [10]. However, this analysis is time consuming, since both the initial Jacobi constant $\bar{C}$ for the propagation within the Moon and Sun's starting phase angle θ_{S0} should be varied.

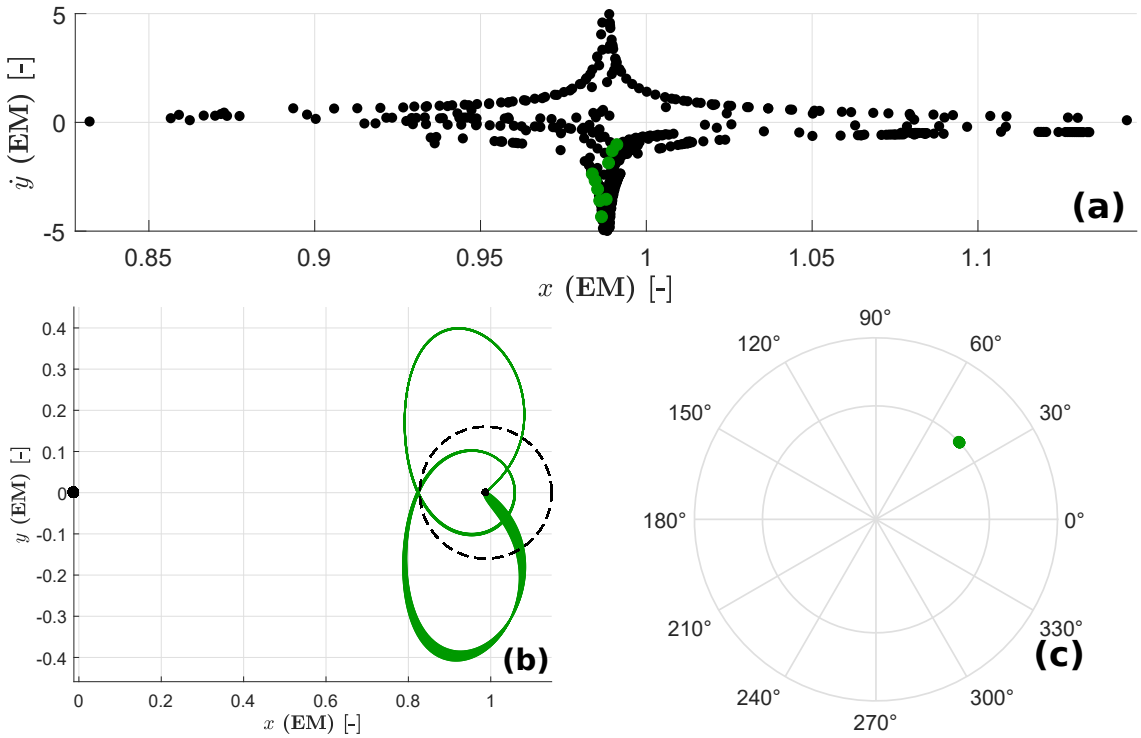

Figure 5.7: Fourth-order intersections with the Poincaré cut on the x-axis at $x \in [1-\mu-R_{hill}; 1-\mu+R_{hill}]$ of lunar ejection orbits. Initial condition $\theta_{S0} = \pi/2$, $\bar{C}_0 = 2.97$; **(a)** view of the intersections of the ejection orbits with the cut in the $x\dot{y}$-plane. One family only here reported, similar to family-g' from [10]; **(b)** shape of the green family shown in (a); **(c)** initial lunar collision angles for the green family.

5.3. Multiple M2M transfer

In this section two different approaches for obtaining sequences of single M2M transfers are described and shown. The definition of multiple M2M transfer is highlighted in Section 4.1.
The outline of this section partially follows from what is described in Section 5.2: in Section 5.3.1, similarly to what is discussed in Section 5.2.1, a *pseudo*-Poincaré cut on the y-axis is used as a dimensionality reductant of the problem in order to visually find possible ballistic sequences of three M2M transfers. Conversely, the concept of Poincaré cut is discarded for the second method, outlined in Section 5.3.2, where double-collision M2M transfers are employed to obtain a first guess for a sequence of ballistic M2M transfers.

5.3.1. Multiple M2M transfer on a pseudo-Poincaré cut

This section can be regarded as the follow-up of Section 5.2.1, where ballistic M2M transfers are obtained with a similar approach to what is described in Section 3.2. Briefly, a method is outlined to obtain an initial propagation point on the cut which has the characteristic of being a good candidate for an M2M transfer in the Sun–Earth–Moon BR4BP. However, the procedure, which depends on three coefficients, succeeds for approximately 60% of the possible cases. In Section 4.1 high-order encounters of lunar ejection orbits are employed in combination with low-order ones to obtain candidate points for sequences of triple (or double) ballistic M2M transfers, with the CR3BP dynamical model.
The approach here employed takes its idea from the latter, although now related to the BR4BP case: aligned with the employed nomenclature, the $\left(1^{st}\,\mathrm{bw}_{\theta_{S0,1}}, 3^{rd}\,\mathrm{bw}_{\theta_{S0,2}}, 2^{nd}\,\mathrm{fw}_{\theta_{S0,3}}, 4^{th}\,\mathrm{fw}_{\theta_{S0,4}}\right)_{y+}$ set of intersections is chosen. However, in this simplified case, the initial solar phase angle is set to be null for every-order intersection, namely $\theta_{S0,i} = 0$ deg for $i = \{1, 2, 3, 4\}$. The 3D- and top-view of the intersections of the four different-order lunar ejection orbits with the common Poincaré cut are shown in Figs. 5.8a and 5.8b, respectively.

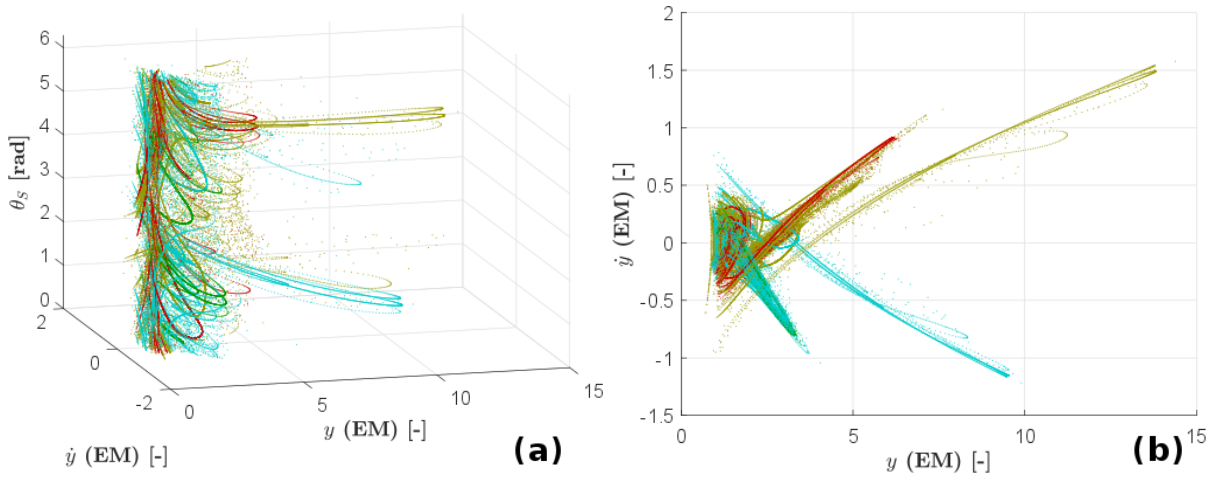

Figure 5.8: $\left(1^{st}\,\mathrm{bw}_0, 3^{rd}\,\mathrm{bw}_0, 2^{nd}\,\mathrm{fw}_0, 4^{th}\,\mathrm{fw}_0\right)_{y+}$ intersections (green, cyan, red and yellow respectively) of lunar ejection orbits with the Poincaré cut on the positive y-axis, for $\dot{x} \geq 0$ and $\bar{C}_0 = 2.97$; **(a)** 3D-view; **(b)** top-view.

The candidate initial propagation points on the cut are retrieved similarly to what is done in Section 5.2.1, although extending the concept to four cuts. The same set $\mathscr{G}$ is now defined as

$$\mathscr{G} = \left\{ \boldsymbol{x}^*_{2,fw} \in S^{\theta_{S0,2}}_{2,fw} : A^* \neq \varnothing \wedge C^* \neq \varnothing \wedge D^* \neq \varnothing \right\} \tag{5.5}$$

where, for every $\boldsymbol{x}^*_{2,fw}$, A^*, B^*, D^* are defined as

$$\begin{aligned} A^* &= \left\{ \boldsymbol{x}_{1,bw} \in S^{\theta_{S0,1}}_{1,bw} : d\left(\boldsymbol{x}^*_{2,fw}, \boldsymbol{x}_{1,bw}\right) < 1 \right\} \\ C^* &= \left\{ \boldsymbol{x}_{3,bw} \in S^{\theta_{S0,3}}_{3,bw} : d\left(\boldsymbol{x}^*_{2,fw}, \boldsymbol{x}_{3,bw}\right) < 1 \right\} \\ D^* &= \left\{ \boldsymbol{x}_{4,fw} \in S^{\theta_{S0,4}}_{4,fw} : d\left(\boldsymbol{x}^*_{2,fw}, \boldsymbol{x}_{4,fw}\right) < 1 \right\} \end{aligned} \tag{5.6}$$

with the same distance function $d(\boldsymbol{x}_1, \boldsymbol{x}_2)$ defined in Eq. (5.4). A value of 0.05 is here used for every semi-axis. The set $\mathscr{G}$ takes a collection of points from $S^{\theta_{S0,2}}_{2,fw}$, while the candidate points are obtained by a 3D-linear

interpolation between every $\left(\boldsymbol{x}^*_{2,fw}, \boldsymbol{x}_{1,bw}\right)$ couple for every A^* whose associated $\boldsymbol{x}^*_{2,fw}$ respects Eqs. (5.5) and (5.6): the approach may easily be extended to interpolate using couples of C^* and D^*. The missing coordinate, namely $\dot{x}$, is obtained using the interpolation between the points of the considered couple, although it is not represented on the cut.
For this simplified case (every initial solar phase angle is set to zero) an example of a sequence of three ballistic M2M transfers is shown in Fig. 5.9a in the synodic frame, magnified in Fig. 5.9b in proximity of the Moon; in Fig. 5.9c the trend in time of both distance and energy with respect to the Moon is outlined.
The locations of the candidate points on the cut, together with the points leading to ballistic sequences of triple M2M transfers are not here reported, due to their overwhelming amount. However, statistics are highlighted in Table 5.1.
It is quite remarkable how the percentage of the sequences of both triple and double M2M transfers is higher than their CR3BP counterparts. Although few of the considered candidates happen to be relatively close in the cut, the associated orbits tend to mutually diverge, due to the nonlinearity introduced by the Moon at the fly-by.

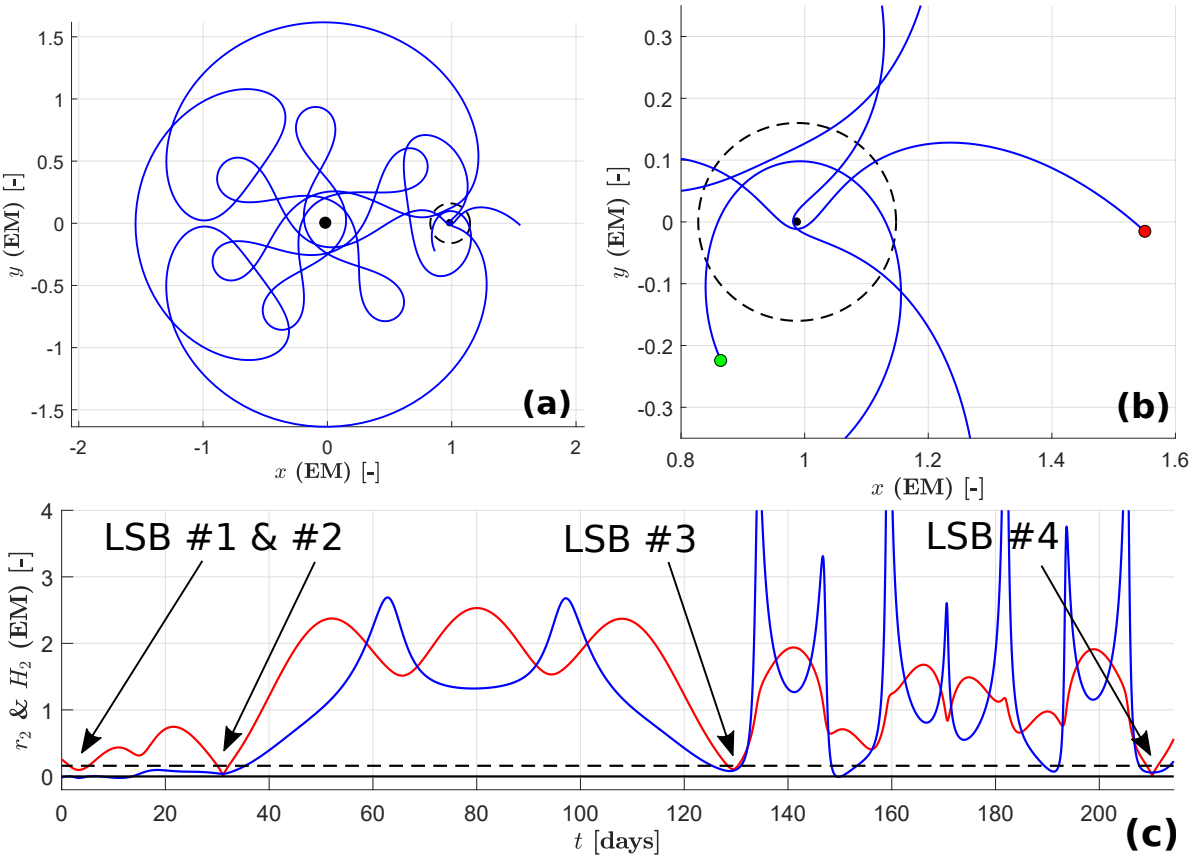

Figure 5.9: **(a)** Example of a ballistic sequence of three M2M transfers in the BR4BP dynamical model. Earth and Moon depicted as black dots, lunar Hill's sphere as a dashed circle about the Moon; **(b)** magnification of (a) about the Moon. Green and red dots marking the start and end of the trajectory, respectively; **(c)** trend in time of r_2 and H_2 (red and blue, respectively) for the trajectory highlighted in (a) and (b).

# Candidates	Triple M2Ms	Double M2Ms
6376	1266 ≈ 20%	1814 ≈ 29%

Table 5.1: Statistics concerning ballistic sequences of M2M transfers. Mind how every sequence of three M2M transfers can be regarded as two different sequences of double M2M transfers: however, this is not considered in the shown numbers. Moreover, notice how the triple and double percentages are higher than what shown in Fig. 4.1.

5.3.2. Database of double-collision M2M transfer

In this section a different approach for potentially obtaining a sequence of M2M transfers with the BR4BP dynamical model is developed and discussed, highlighting both its advantages and disadvantages. As the title suggests, a database of double-collision M2M transfers, previously studied in Section 5.2.2, is built and later employed as a framework for obtaining the trajectory. The database itself can be regarded as a step-back in the construction of a well-defined M2M transfer, since the trajectory is allowed to collide with the Moon: however, this brings to a tremendous reduction of the computational burden and a direct improvement towards a straight usage within a real space mission scenario, thanks to the gained simplicity.
A database of solutions is generally a prerogative for a real space mission, in order to hasten the preliminary trajectory design process and at the same time, account for different errors; as a further reason, as it happens for a secondary payload, the initial condition may significantly vary throughout the whole mission design process, therefore demanding a certain readiness for providing the nominal trajectory. EQUULEUS is an emblematic example of this, since its ejection state depends on the always-changing SLS launching conditions. For the trajectory of a spacecraft which leverages the gravitational influence of the Moon, accounting for the availability of an already-designed and easy-to-inquiry database of M2M transfers becomes a powerful tool: one of the greatest advantages consists in storing the initial and final conditions of the M2M transfers only, therefore avoiding any other mid-course coordinate. With this method, a pre-optimized first guess of the trajectory can be rapidly computed. The benefit of a database is even recognizable in its potential of tightening the whole search space at the very first iteration, defining where the best trajectories are.
With these preliminary concepts in the background, the proposed database is built under the following characteristics:

- Sun–Earth–Moon BR4BP propagating scheme.
- M2M transfers stored as lunar double-collision orbits, namely starting from lunar center and ending at lunar surface.
- Maximum Time Of Flight (TOF) equal to 400 terrestrial days.
- Maximum reachable distance from the origin of the reference frame equal to 15 dimensionless Earth–Moon units (roughly 5766×10^3 km).
- Initial Sun's phase angle $\theta_{S0} \in [0, 2\pi)$ with a step size of $\Delta\theta_{S0} = \pi/500$, initial Jacobi constant $\bar{C} \in [2.8, 3.1]$ with step size $\Delta\bar{C} \approx 0.043$ and lunar collision angle $\theta_C \in [0, \pi)$ with step size $\Delta\theta_C = \pi/360$ (from Fig. 3.2a $\theta_E = 2\theta_C$).

The current version of the database stores almost 730 thousands M2M transfers. The latter are saved considering the following array:

$$\left[\bar{C}_0, \theta_{S0}, \theta_{E0}, v_{\infty,E0}, \bar{C}_f, \theta_{Sf}, \theta_{Ef}, v_{\infty,Ef}, TOF\right] \tag{5.7}$$

where the pedix 0 stands for the initial condition and f for the final one (at lunar re-encounter). The very last variable may have been superfluous for the database if θ_{Sf} was not stored as bounded in $[0, 2\pi)$, since $TOF = \left(\theta_{Sf} - \theta_{S0}\right)\omega_S$. Within the array, $v_{\infty,E}$ represents the magnitude of the v_∞ with respect to Earth. Although defined in a BR4BP, the database itself is designed to carry typical CR3BP and Keplerian quantities. This database has been conceived as the improvement of the work from Yarnoz et al. [36], where a Sun–Earth CR3BP dynamical model is employed to obtain M2M transfers, discarding the gravitational attraction of the Moon.
For the patching of two consecutive M2M transfers, the zero-level strategy is employed: briefly, the final state of the i^{th} M2M transfer is connected to the initial state of the $(i+1)^{th}$ one by assuming a lunar hyperbolic passage. Relative formulae are discussed in Appendix A. This represents a really strong assumption, which does not correctly mimic what really happens in a neighbourhood of the Moon at the moment of patching; however, this assumption becomes admissible to preserve the simplicity of the database.
The latter can be inquired based on different approaches, although in this report one example only is given: the aim is bringing the spacecraft to a final highly energetic condition, key-element for Earth-escaping trajectories. No constraint on the initial condition is addressed. This is perfectly aligned with DESTINY+ mission design, as described in Section 1.1. However, the database may have been used for EQUULEUS case too, since, symmetrically to the DESTINY+ case, the aim is to lower down the energy before reaching the libration orbit about Earth–Moon L_2, since NASA's SLS will give a high push to the spacecraft [36].

Increasing the energy - DESTINY+ case

In this case the M2M database is employed to obtain a trajectory which leverages both lunar and solar gravitational pull to increase the spacecraft energy. This is an usual scenario in case the latter needs to leave the Earth–Moon system. DESTINY+, discussed in Section 1.1, represents one possible example: the trajectory here developed can be used for the mid-phase (or rather M2M-phase) of that mission. Here, the database is inquired starting from the final condition, marked by a high energy with respect to Earth and obtains all the feasible initial conditions and M2M transfers which can achieve it. For what concerns DESTINY+ case, both initial and final state of the M2M-phase will then be patched with the remaining two *pieces* of the mission. However, this study is not here discussed.

Representing a coarse wide search and without having a specific final state for the M2M-phase, the database is inquired without setting any request on θ_{Ef} and θ_{Sf}, therefore looking at those transfers having a $v_{\infty,Ef} > 1.5$ km/s, as specified in [36].

Both single and multiple double-collision transfers are sought: the latter are obtained from a sequence of the former, using a pruning algorithm. This algorithm is implemented accounting for the *continuity* of the whole trajectory by means of the zero-level patching strategy: both $\bar{C}$ and θ_S are approximated as constant during the lunar flyby while θ_E is varied according to the patching. Dealing with a database, therefore with a discrete amount of trajectories, it is almost impossible to find two M2M transfers so that $\bar{C}^i_f = \bar{C}^{i+1}_0$ and $\theta^i_{Sf} = \theta^{i+1}_{S0}$ are valid, where i refers to the i^{th} M2M transfer along the sequence. For this reason, thresholds on both variables are defined before re-inquiring the database for a subsequent M2M transfer; in the case here reported, thresholds are held at a low value in order to diminish the weight on the algorithm. The condition the preceding M2M transfer needs to satisfy in θ^i_{Ef} is related to the patching strategy: if $\theta^i_{Ef} \in \left[\theta^i_{Ef,min}, \theta^i_{Ef,max}\right]$ then the double-collision transfer is considered for the patching. The two boundaries for θ^i_{Ef} are related to θ^{i+1}_{E0} by the lunar flyby deflection angle and a maximum and minimum perilune radius, set at 100 km above lunar surface and at its Hill's sphere border, respectively (see Appendix A). A threshold on the maximum number of double-collision M2M transfers per trajectory is added: this is generally the case in the real mission scenario, since every flyby represents a critical element for the trajectory, enhancing either the workload for the operational control and the risk of error.

In the example here developed, the database parameters are

$$\left(TOF,\, v_{\infty,Ef},\, \Delta\theta_S,\, \Delta\bar{C},\, N_{M2M}\right) = \left(500\,\text{days},\, 1.5\,\text{km/s},\, 1.5\,\text{deg},\, 0.5,\, 2\right) \tag{5.8}$$

Fig. 5.10a shows all the available solutions, reporting the difference in Jacobi constant between the ending and starting point of the trajectory $\Delta\bar{C}$, versus the cumulative TOF; colors provide data on the number of M2M transfers, black for one double-collision, red for a sequence of two. The green dot in Fig. 5.10a is represented by the associated trajectory in Figs. 5.10b and 5.10c, depicted in the inertial Earth-centered and barycentric synodic reference frame respectively, highlighting its starting, patching and ending points (green, yellow and red, respectively) together with the path covered by the Sun throughout the transfer time (red dashed line, not in scale). Figure 5.10d reports the trend in time of the Jacobi constant $\bar{C}$ (blue), the distance from the Moon r_2 (green) and the scaled energy with respect to Earth E (red). The vertical dashed black line marks the connection with the second double collision M2M transfer. Pictures confirm the applicability of the approach, namely the energy of the spacecraft is enhanced: however the latter is primarily increased by lunar flybys, rather than by the solar influence, which takes quite long to properly act. This is usually the case for the trajectories within the database. Although the number of possible solutions is rather high, no triple sequence of M2M transfer is visible: this is due to the low range of initial $\bar{C}$ used for the definition of the database, to the zero-level patching approach and to the low allowed maximum TOF. It is now straightforward to understand some advantages and disadvantages of this method with respect to the former version [36].

- Bringing the Moon within the model increases the complexity and improves the precision. However, thanks to the employment of double-collision orbits, the complexity lies in using the regularization scheme only, equalizing the total number of free variables.
- The presence of the Moon unlocks the possibility to leverage its gravity pull: this translates in general to a lower TOF to reach a specific condition, since Sun's gravitational pull requires more time to be leveraged.
- The former version of the database, built with the CR3BP dynamical model is much lighter: this is in part due to a lower amount of available solutions.

All in all, the idea of a database looks highly promising, since it gives an easy and rapid tool to design a pre-optimized first guess trajectory. However, a future version should be computed for a higher range of initial $\bar{C}$, in order to enhance the feasible sequences of M2M transfers. Concluding, a more efficient method for the patching should be developed, without impairing the simplicity of the tool.

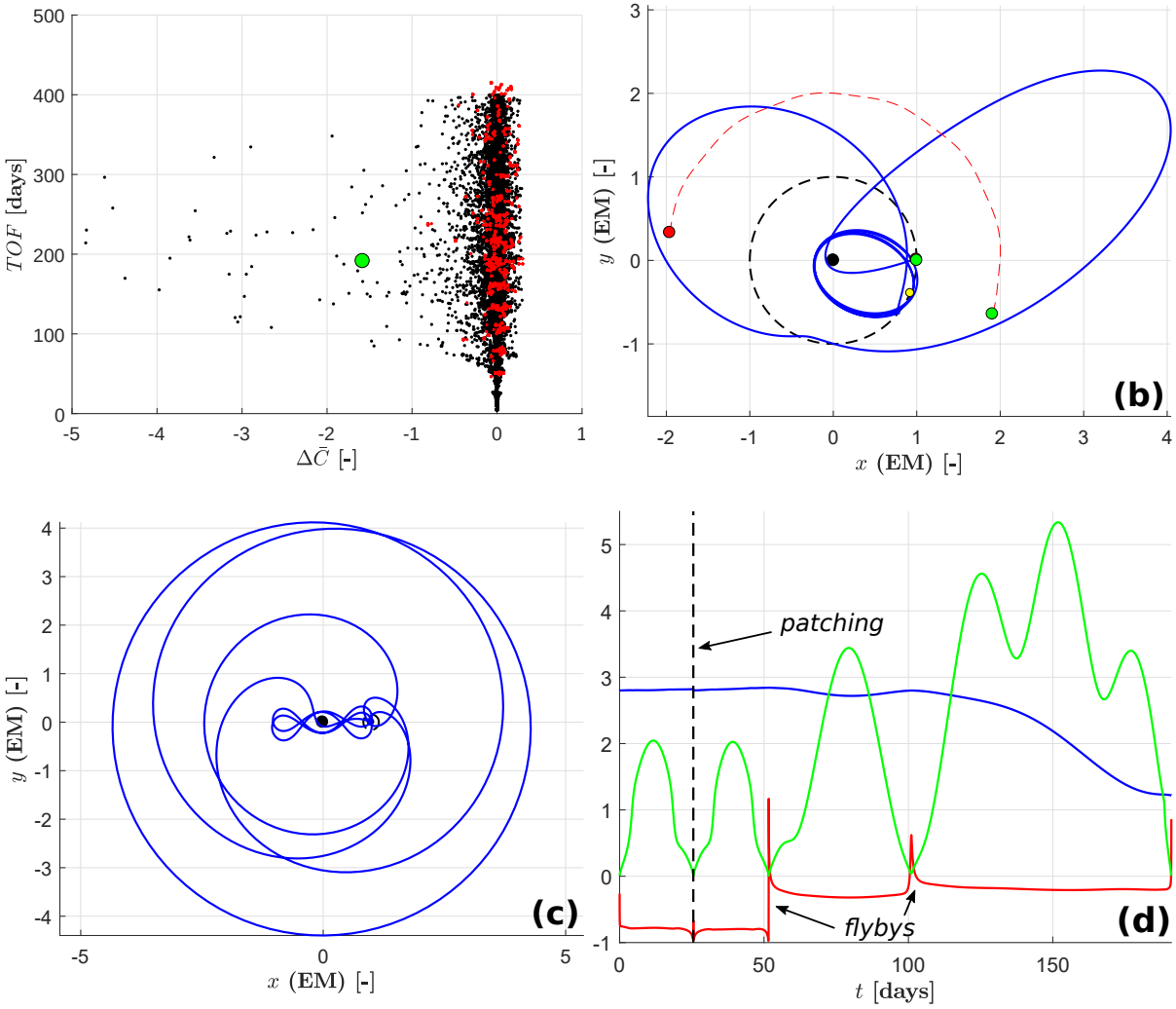

Figure 5.10: **(a)** Single (black) and double (red) double-collision M2M satisfying Eq. (5.8). $\Delta\bar{C}$ vs cumulative TOF. Green point representing the double double-collision M2M transfer depicted in (b) to (d); **(b)** trajectory in the inertial Earth-centered reference frame from the green point in (a). Sun's position depicted in dashed red line (not in scale). Mind how the starting and ending points overlap (green and red), being the latter the one coming from the hyperbolic-like trajectory about the Earth. Sun's path too is marked by same starting and ending points; **(c)** trajectory in (b) in the synodic barycentric frame; **(d)** trend of Jacobi constant $\bar{C}$ (blue), distance from the Moon r_2 (green) and scaled energy with respect to Earth E (red) vs time. Vertical dashed black line marking the patching.

5.4. Conclusions

This section concludes the whole chapter, reporting the major achievements concerning M2M transfers in the BR4BP dynamical model.

In Section 5.1 the propagation scheme for obtaining lunar ejection orbits in the BR4BP model is outlined, counting on a dynamical approximation in the first part of the trajectory. Clearly, the concept of the Zero Velocity Curve is discarded; however the latter helps in defining what represents a reasonable boundary for trajectories propagated with the CR3BP scheme, in agreement with Section 4.3.

Subsequently in Section 5.2 a procedure to obtain single ballistic M2M transfers is outlined, employing the intersections of lunar ejection orbits with the Poincaré cut on the positive y-axis. A classification of double-collision M2M transfers is performed, which finds its corresponding in the existing literature, although for the periodic case in a simplified version of the CR3BP [10]. To the best of author's knowledge, this is the

first time lunar collision orbits are employed for trajectory design in the BR4BP. Similarly, a classification of double-collision M2M transfers in the BR4BP has never been performed, although the proposed one needs to be further extended.
In Section 5.3 both the concept and the method for obtaining a single M2M transfer are extended, towards the definition of an algorithm to delineate ballistic sequences of M2M transfers, by employing the intersections of lunar ejection orbits with a common Poincaré cut. The procedure strongly depends on the geometry of the involved bodies and on an extensive computational effort but results show up, agreeing with the initial intuition. However, aligned with the outcome of their CR3BP counterparts, both single and multiple ballistic M2M transfers obtained from the Poincaré cut do not encompass the whole existing realm of possible solutions, since, according to the algorithm, trajectories need to be patched at the cut: this is not a mandatory requirement for an M2M transfer. Although not complying with the M2M requirements, lunar double-collision orbits solve for this issue.
The second research objective is here achieved: indeed a database of double-collision M2M transfers is built under the assumptions of the BR4BP. With respect to the former version [36], the database can now leverage the gravitational pull of the Moon, allowing to diminish the requested mission time. From a real trajectory design scenario, inquiring the database gives a first and fast broad scan of the whole search space, helping to immediately discard uninteresting regions. The application of the database to the M2M-phase of the trajectory of JAXA's DESTINY+ mission is shown, pointing out its efficiency; the database is easily applicable to JAXA's EQUULEUS case too. However, an extension of the amount of solutions is needed, in order to encompass a wider initial range of energies, together with the implementation of a new and more reliable patching strategy.
Concluding, this chapter highlights the main features of M2M transfers in the BR4BP, allowing to understand the difference with the simpler CR3BP. In particular the former is more complex to handle, since the simplicity provided by the existence of a first integral is not anymore present. The benefit is that trajectories are now considered more precise with respect to their CR3BP counterparts, especially at significant distance from Earth: indeed, the limit of 1.5 (EM) units is now meaningless, since the BR4BP intrinsically accounts for the presence of the Sun.
No discussion on controlled M2M transfer or optimization strategy is provided in this chapter: the reason is that no feasible method has been implemented, besides a simple shooting algorithm with the usage of the Differential Corrector, highlighted in Section 2.1.4, not included in this report to avoid repeating a similar discussion to what is already pointed out for the CR3BP.

6 Conclusions

This chapter concludes the research work here presented. Besides a very brief theoretical introduction, the author highlights throughout this report the main achievements of his research work at ISAS/JAXA. First, a summarizing overview of the obtained results is given in Section 6.1. Subsequently in Section 6.2, future possible improvements of this work are discussed, in order to potentially shape a new research. Eventually in Section 6.3 a new topic, born from different considerations concerning M2M transfers, is highlighted as a possible diversion from this research.

6.1. Achievements

In this section, the main achievements of this six-month research are outlined.
Almost every research work starts with a specific set of questions and objectives; in this report they are extensively highlighted in Section 1.3 and here used to judge the obtained results.

Research question 1: *Which useful information can lunar collision orbits provide to obtain Moon-to-Moon transfers within the framework of the Circular Restricted Three Body Problem and the Bi-circular Restricted Four Body Problem?*
Lunar collision orbits are literally a *basin* of useful information, especially for orbits passing close by the Moon. As pointed out in Chapter 3, lunar collision orbits behave as separatrix with respect to prograde and retrograde motion of orbits approaching the Moon. Useful characteristics of trajectories flying close to collision orbits can be easily inferred: indeed, by looking at their intersections with a Poincaré cut, one can substantially obtain information concerning their perilune and the associated value of energy and angular momentum with respect to the Moon. For these reasons, a Moon-to-Moon transfer can be designed with the information given by lunar collision orbits. In a similar fashion, trajectories which come from a low perigee can be studied, as depicted in Fig. 3.13b.
Lunar collision orbits have again shown an almost equal structure to the invariant manifolds emanating from the HLOs' of the collinear Lagrangian points: this is a remarkable result, since by employing the former as a substitute of the latter one diminishes the computational burden and widens the available energy regime.
For what concerns the BR4BP, discussed in Chapter 5, lunar collision orbits still provide useful information about trajectories approaching the Moon, although the nonautonomous characteristic of the model complicates the problem, losing part of the benefits of the Poincaré cut.
Concluding, lunar collision orbits yield useful information concerning sequences of ballistic M2M transfers, for each of the analysed dynamical model.
All in all it can be asserted how lunar collision orbits can provide useful information on trajectories approaching the Moon, which can be leveraged to obtain a properly defined Moon-to-Moon transfer.

Research question 2: *In the context of a preliminary trajectory design, to what extent can a database of Moon-to-Moon transfers benefit from the introduction of the gravitational pull of the Moon within the dynamical model?*
It is shown in Section 5.3.2 how, by including the presence of the Moon within the dynamical model for the

construction of the database, new trajectories are uncovered which leverage lunar gravitational pull to aim the spacecraft towards the desired final condition. These solutions would have not been present in case the employed dynamical model was a simpler Sun–Earth planar CR3BP. These transfers clearly shorten the required time to achieve a great jump in the energy, since a lunar flyby acts faster than the gravitational influence of the Sun. With the focus on lunar double-collision orbits only, just four variables are needed to completely define every transfer, as it is done in [36]; therefore, the increase in complexity of the dynamical model does not weigh on the computational effort to obtain the database. However, the database itself should include two more variables per M2M transfer.

Sub-questions:
Although part of the sub-questions are already answered above, few others needs a singular proper reply.
What are the benefits of propagating an orbit with Levi Civita regularization scheme, when compared to Cartesian one?
Levi Civita regularization scheme tends to be slightly slower and less precise when compared to the Cartesian one. However the former is necessary to solve for the local singularity at the Moon.
Which are the feasible strategies to opportunely correct a missing Moon-to-Moon transfer by means of impulsive maneuvers?
In this report, different strategies are approached; however, the most promising appears to be the one referred to as *Targeting the Poincaré cut*, using MATLAB built-in optimizer `fmincon`, with a multiple impulsive strategy. Nevertheless, this consideration is restricted to the cases shown in this report; the employment of other more complex optimization schemes may lead to better outcomes.
In which case should the Bi-circular Restricted Four Body Problem dynamical model be preferred to the simpler Circular Restricted Three Body Problem one?
Although the former is more complex than the latter, the BR4BP provides a better estimate of the trajectory, since it is closer to the real model. The CR3BP lacks in precision the more the trajectory gets further from the centre of the analysed reference frame. The characteristic of being autonomous can represent a good feature to gain a deeper insight in the problem. All in all, the BR4BP should be preferred whereas the gain in improved precision outweighs the loss in simplicity.

Research objectives:
Both main research objectives and associated sub-goals have successfully been achieved and addressed in this conclusive report. Being the first main objective more on the research side, it has lead to uncover a severe amount of important features of lunar collision orbits, which partly helped in achieving the second task too. After a clear definition of what an M2M transfer is, quite few methods for obtaining it are disclosed, with their own advantages and drawbacks, for each of the studied dynamical models. Poincaré maps are extensively used to both build M2M transfers and correct missing lunar fly-bys by means of impulsive maneuvers. One of the most remarkable aspects is that collision orbits are here employed for the first time ever for trajectory design, accounting to the best of author's knowledge.
For what concerns the second main objective, being a more industrial-side task, the amount of inherent scientific outcome is rather limited: however, properly setting up the right building blocks in a computational efficient way was not an easy task. By comparing the database with the former version it is shown how the one developed in this report has its own advantages. However, the new version has two more elements stored per transfer, with respect to the former one: this choice eases the inquiry for both missions under study, although increasing the weight of the database. The latter shows a clear applicability to the preliminary design of the M2M trajectory phase of DESTINY+; however, studying the EQUULEUS case would have been equally simple.

6.2. What follows

In this section, possible extensions of the research outlined in this report are highlighted; the main purpose is to potentially trigger new discoveries in the field of astrodynamics by improving the work here presented. The major aspects pertaining the first main objective are:

- Although a single Poincaré cut decreases the complexity of the system, it forces the M2M transfer to pass through it. By opportunely combining more Poincaré cuts, one may overcome this flaw.
- The underlying dynamical model used throughout this work is rather imprecise if one wants to straightforwardly apply the outcome to the real case. Different aspects can be leveraged to solve for this: al-

lowing a 3D-motion where lunar collision orbits can be regularized with Kustaanheimo-Stiefel scheme, including eccentricities and inclination of the main orbiting bodies, accounting for perturbations (solar radiation pressure, higher order gravitational potential and so forth) are possible solutions to close the gap with the real case scenario.

- A more efficient and reliable algorithm needs to be developed for the M2M transfer recovering, thoroughly leveraging the information of a *pile* of Poincaré cuts. A subsequent step would consists in implementing an iterative algorithm for sequences of multiple impulsive M2M transfers, eventually accounting for low-thrust arcs.

For what concerns the second main objective, improvements can be suggested in:

- The patching approximation is rather imprecise. Improving it, without weighing on the simplicity of the approach would lead to a better preliminary design with the database.
- Once the best trajectory is obtained, a subsequent step consists in providing a first optimization to retrieve a properly defined M2M transfer from the double-collision one.
- The database needs to be validated with past flown missions. However, this task depends on the availability of data.
- The classification of lunar double-collision orbits in the BR4BP needs to be extended and strictly formalized in order to encompass more orbits.

6.3. Possible future research

This main topic of this section slightly strays from the aspects treated throughout this report, by providing a new interesting theme concerned with collision orbits. It is proposed as a standalone section since it represents more a diversion from the rest of this report rather than a logical consequence.
The idea is to widen the restrictive view given by one central body (Earth) and one orbiting satellite (our Moon) only, which has been a landmark throughout this report. This concept is here extended to cover a more complex system: for this purpose, the Jovian one is briefly addressed in this survey. Different studies (Campagnola and Russell [5], Koon et al. [13]) have shown interesting features of this system, composed by a central planet, namely Jupiter itself, and plenty of orbiting natural satellites. Among the latter, the present study focuses on two of the so-called Galilean moons, namely Europa and Ganymede. Their main orbital characteristics are briefly reported in Table 6.1.

Moon	a [10^3 km]	T [days]	e [-]	i [deg]
Europa	671.080	3.552	0.010	0.471
Ganymede	1070.400	7.155	0.001	0.204

Table 6.1: Main orbital data for both Europa and Ganymede, second and third Galilean moon of Jupiter respectively, with respect to Jupiter. Table shows their average semi-major axis, periods, eccentricities and inclinations (Jupiter's equator as a reference), respectively from left to right. A single day refer to one terrestrial day, namely 86400 s (constants taken from Acton [1], Lissauer and de Pater [18]).

From Table 6.1 it is evident how the motion of the two analysed moons is almost perfectly coplanar and Ganymede's period is about twice Europa's one.
The idea here is to employ collision orbits for both Europa and Ganymede in order to define a transfer from one moon to the other one: in this case, a transfer from Ganymede to Europa is analysed, shortly referred to as Ganymede-to-Europa (G2E).
The strategy is slightly more complicated to what is described in the previous chapters of this report: two systems, namely Jupiter–Europa–spacecraft (JE) and Jupiter–Ganymede–spacecraft (JG) are simultaneously studied, with the CR3BP assumptions. Ejection orbits from both moons are computed and their intersections with a common Poincaré cut are stored and later analysed. For the sake of easiness, the positive side of the axis parallel to the $y-$axis, passing through Jupiter in the JE-system is used as cut; nevertheless a different choice would have not changed the main results here achieved. The initial propagation epoch for both system is with Jupiter, Europa and Ganymede aligned along the positive inertial Jupiter-centered x-axis, although a different geometry is possible. The initial Jacobi constants for the two systems are $\bar{C}_{JE} = 2.97$ and $\bar{C}_{JG} = 2.9$.

Finding the intersections with the cut for the JE-system is not different to what is described in the previous part of this report. However, for the JG-one a transformation of coordinate is needed: indeed, in the inertial system the common Poincaré cut passes through Jupiter, rotating with an angular velocity given by the JE-system. As a consequence, in the JG-system, the cut is not steady, but rotates.
Since propagated in two different systems, the JE-collision orbits and the JG-ones have a different Jacobi constant at the intersection with the cut: for this reason the $\bar{C}$ of the JE-system is employed as a third representation variable at the moment of patching. This procedure is addressed as patched CR3BP in Koon et al. [14].
Dealing with a G2E transfer, the intersections of the backward-propagated JE-collision orbits and the forward propagated JG-ones are used to geometrically define the initial propagation points. With a proper initial geometry, a G2E can be obtained which is constructed from the first intersections only of the ejection orbits with the common cut, for both systems. However, this case is not here treated.
Conversely to the rest of this report, the trajectory is not *continuous* at the moment of patching, in order to have a double-collision transfer. In Figs. 6.1a to 6.1d the intersections of the collision orbits for the two systems are shown for the backward-propagated JG-ejection orbits (red, up to the sixth order) and the forward-propagated JE-ones (green, up to the fifth order); however, the survey for seeking a feasible G2E is performed on a wider range of order encounters with the cut, not shown to ease the reading. A G2E is then depicted in Figs. 6.2a and 6.2b for the inertial Jupiter-centered and JE-barycentric reference frame, respectively. The green arc is the trajectory propagated in the JE-system, while the red one is obtained from the JG-system.
All in all, the transfer resembles a mere ellipse between the two moons: however, the dynamical model is richer than what achievable with a simple two-body patched conics approach. The obtained geometry is a result of the selected high energies for the JE- and JG-system.

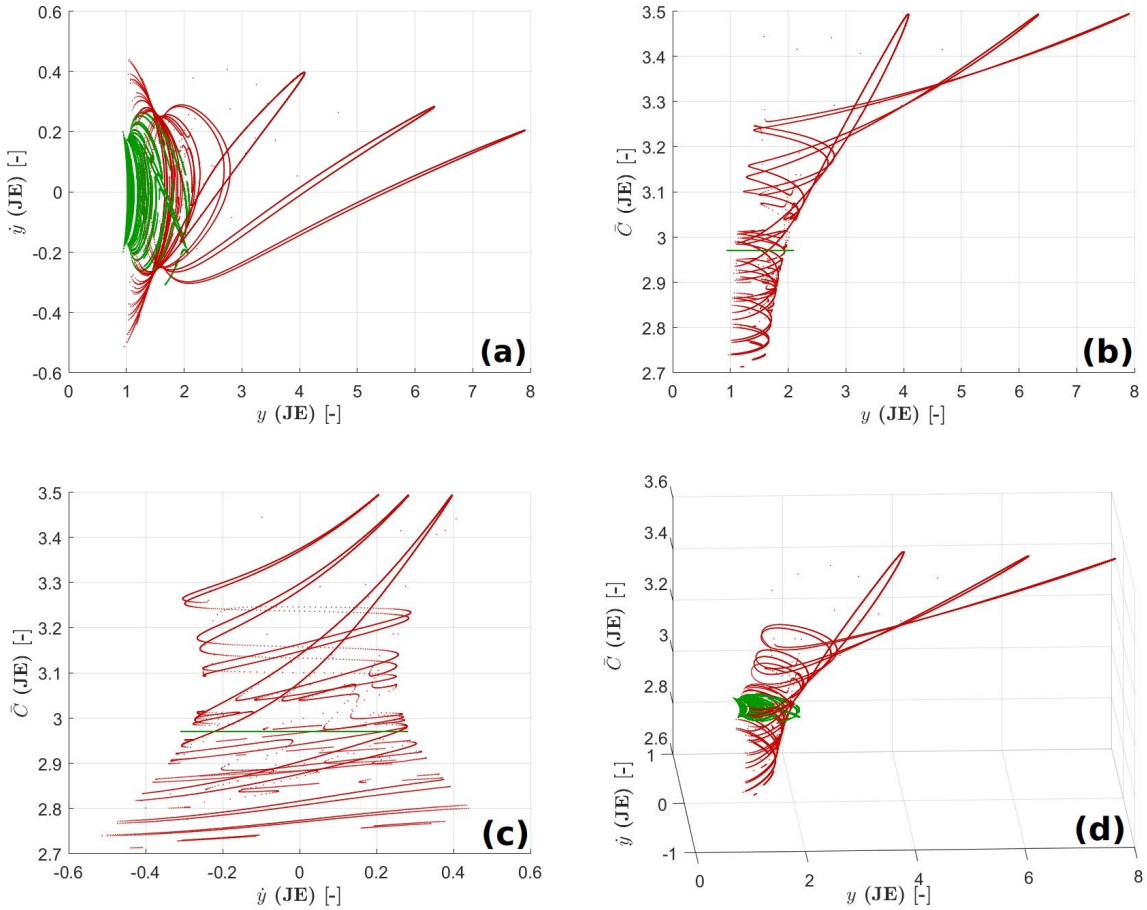

Figure 6.1: Different views for the intersections of the backward-propagated ejection orbits of the JE-system up to the fifth order (green) and the forward-propagated of the JG-one up to the sixth order (red) in the $y\dot{y}\bar{C}_{JE}$-space. The former obtained with a $\bar{C}_{JE} = 2.97$, while the latter with a $\bar{C}_{JG} = 2.9$; **(a)** top-, **(b)** $y\bar{C}$-side, **(c)** $\dot{y}\bar{C}$-side and **(d)** 3D-view, respectively.

Whereas a decreases of the Jacobi constants is performed, medium- and low-energy transfers may be *uncovered*, resulting in a different and less conventional geometry for the trajectory. This further confirms the great potential of collision orbits, which are capable of describing different energetic levels with one theory only. As an extension, the same procedure can be employed for other Jovian moons, accounting for a multi-moon itinerary. Transfers connecting planets of our solar system can be studied and designed with the same procedure.

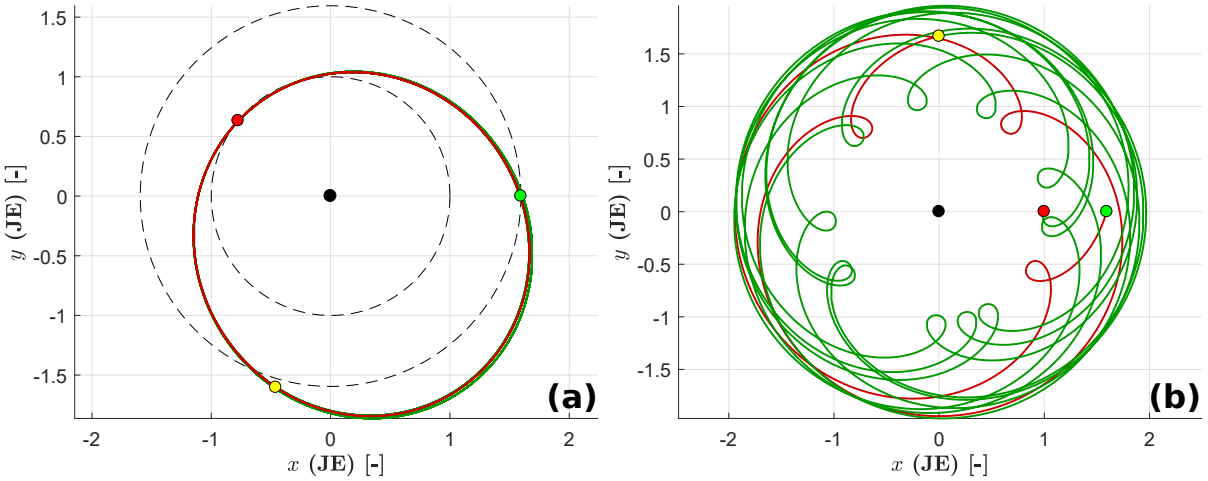

Figure 6.2: Example transfer generated from propagating two initial conditions on the cut distant 4.5×10^{-4} in the $y\dot{y}\bar{C}_{JE}$-space. The transfer starts from Ganymede (green point) along the red trajectory, switching system at the yellow point, representing the Poincaré-cut. The transfer culminates at the red point, namely Europa. Starting propagation points are retrieved from the 21^{st} intersections of the JE-system and the 4^{th} from the JG-one. Transfer time is 90 terrestrial days; **(a)** Jupiter-centered inertial reference frame; **(b)** JE barycentric reference frame.

A

Derivation

Energy and angular momentum with respect to the Moon

In Section 2.2.1 the equations of the angular momentum and energy of the spacecraft with respect to the Moon are delineated. Here the most important steps for their derivation are reported.
Remembering how the synodic reference frame is converted into dimensionless coordinates leading to a fictitious unitary mean motion $\bar{n}$, with an abuse of notation the shifting angle between the barycentric inertial and synodic reference frames can be regarded as the timewise variable, namely $\theta = t$.
This leads to write the coordinates of the system from synodic barycentric $[x(t),\, y(t),\, \dot{x}(t),\, \dot{y}(t)]$ to inertial secondary-centered $[X(t),\, Y(t),\, \dot{X}(t),\, \dot{Y}(t)]$ as

$$\begin{cases} X(t) &= \big(x(t)+\mu-1\big)\cos t - y(t)\sin t \\ Y(t) &= \big(x(t)+\mu-1\big)\cos t + y(t)\sin t \\ \dot{X}(t) &= \big(\dot{x}(t)-y(t)\big)\cos t - \big(\dot{y}(t)+x(t)+\mu-1\big)\sin t \\ \dot{Y}(t) &= \big(\dot{x}(t)-y(t)\big)\sin t + \big(\dot{y}(t)+x(t)+\mu-1\big)\cos t \end{cases} \tag{A.1}$$

leading to the square of the inertial velocity with respect to the secondary expressed as

$$v_2^2(t) = \big(x(t)+\mu-1+\dot{y}(t)\big)^2 + \big(\dot{x}(t)-y(t)\big)^2 \tag{A.2}$$

This straightforwardly leads to H_2 in Eq. (2.12b). For what concerns h_2, by definition, its magnitude is

$$h_2(t) = \|\boldsymbol{r}_2(t) \wedge \boldsymbol{v}_2(t)\| = X(t)\dot{Y}(t) - Y(t)\dot{X}(t) \tag{A.3}$$

which leads to Eq. (2.12a) after substitution.

Differential corrector for periodic orbits

In Section 2.2.1 the Differential Corrector for the computation of the simple planar periodic orbits about the collinear Lagrange points in the CR3BP is highlighted, through Eq. (2.16). Here more details concerning its derivation are given.
According to [23], simple periodic orbits about collinear Lagrangian points pierce orthogonally twice the $x-$axis of the synodic frame and are symmetric with respect to the same axis. Howell [12] used a similar scheme for 3D halo orbits, which is applicable to the planar case too by reducing the dimensionality of the problem.
Due to the above-mentioned characteristics, the starting- and mid-point for the simple T-periodic orbit can be defined as

$$\boldsymbol{x}_0 = \big[x_0,\, 0,\, 0,\, \dot{y}_0\big]^T \tag{A.4a}$$

$$\boldsymbol{x}_{T/2} = \big[x_{T/2},\, 0,\, 0,\, \dot{y}_{T/2}\big]^T \tag{A.4b}$$

By propagating Eq. (A.4a) till it reaches back the $x-$axis, therefore for a time $t = T/2$, one generally obtains a final state which is not in the shape of Eq. (A.4b), since $\dot{x}_{T/2} \neq 0$. Therefore, $\boldsymbol{x}_0$ needs to be corrected using a

shift $\delta \boldsymbol{x}_0$: a Differential Corrector is here employed, by using a single-shooting technique. The linear relation between the deviation of the state at the start and at half the period of the orbit is different with respect to what is pointed out in Eq. (2.3), since propagation time (namely $T/2$) is present in the equations. The equation for the deviation of the final state becomes

$$\delta \boldsymbol{x}_{T/2} = \Phi(t_0, T/2)\delta \boldsymbol{x}_0 + \dot{\boldsymbol{x}}_{T/2}\delta(T/2) \tag{A.5}$$

However, $\delta(T/2)$ can be solved from the second row of Eq. (A.5), as

$$0 = \phi_{2,1}\delta x_0 + \phi_{2,4}\delta \dot{y}_0 + \dot{y}_{T/2}\delta(T/2) \tag{A.6}$$

where $\phi_{j,k}$ is the (j, k)th term of $\Phi(t_0, T/2)$. By setting $\delta \dot{x}_{T/2} = -\dot{x}_{T/2}$ the first row of the matrix in Eq. (2.16) is obtained. In order to have the second one, th relation $J(\boldsymbol{x}_0 + \delta \boldsymbol{x}_0) = \bar{C}$ needs to be enforced. Therefore, using Taylor-series expansion about $\boldsymbol{x}_0$ it follows how

$$\bar{C} = J(\boldsymbol{x}_0) + \nabla J(\boldsymbol{x})|_{\boldsymbol{x}=\boldsymbol{x}_0}\delta \boldsymbol{x}_0 + \mathcal{O}\left(\|\delta \boldsymbol{x}_0\|^2\right) \tag{A.7}$$

So the second row can be retrieved, by rearranging the equation and neglecting the second-order terms as

$$\delta \boldsymbol{x}_0 = \left[\nabla J(\boldsymbol{x})|_{\boldsymbol{x}=\boldsymbol{x}_0}\right]^{-1}\left(\bar{C} - J(\boldsymbol{x}_0)\right) \tag{A.8}$$

noting how $\delta y_0 = 0$ and $\delta \dot{x}_0 = 0$. The procedure is then iterated until convergence.

Symmetry for the BR4BP

In Section 2.2.2, a time-symmetry was presented. By applying transformation of Eq. (2.19) to system of Eq. (2.18), it follows

$$\begin{cases} \dfrac{\mathrm{d}x}{\mathrm{d}(-t)} = -\dot{x} = -\dot{x} \\ \dfrac{\mathrm{d}(-y)}{\mathrm{d}(-t)} = \dot{y} = \dot{y} \\ \dfrac{\mathrm{d}(-\dot{x})}{\mathrm{d}(-t)} = \ddot{x} = x + 2\dot{y} - \dfrac{(1-\mu)(x+\mu)}{r_1^3} - \mu\dfrac{x-1+\mu}{r_2^3} - \mu_S\dfrac{x - a_s\cos(-\theta_{S0} + \omega_S(-t+t_0))}{r_s(\theta_S)^3} - \dfrac{\mu_S}{a_S^2}\cos(-\theta_{S0} + \omega_S(-t+t_0)) \\ \dfrac{\mathrm{d}(\dot{y})}{\mathrm{d}(-t)} = -\ddot{y} = -y + 2\dot{+} + \dfrac{(1-\mu)y}{r_1^3} + \mu\dfrac{y}{r_2^3} - \mu_S\dfrac{-y - a_s\sin(-\theta_{S0} + \omega_S(-t+t_0))}{r_s(\theta_S)^3} - \dfrac{\mu_S}{a_S^2}\sin(-\theta_{S0} + \omega_S(-t+t_0)) \end{cases} \tag{A.9}$$

Where $-\theta_S = -(\theta_{S0} + \omega_S(t - t_0))$. Using the well-known symmetries of the $\cos()$ and $\sin()$ functions, one can obtain the same starting system of Eq. (2.18), therefore the existence of the symmetry of the solution is verified. Of course, this result can be easily extended to the easier planar CR3BP (setting $\mu_S = 0$).

Initial condition for ejection orbits

In Section 2.2.3, the initial condition for orbits ejected from $(x, y) = (1-\mu, 0)$ is given as

$$\boldsymbol{u}_0 = \begin{bmatrix} u_1 \\ u_2 \\ u_3 \\ u_4 \end{bmatrix}_0 = \begin{bmatrix} 0 \\ 0 \\ \sqrt{\dfrac{\mu}{2}}\cos\theta_{c,0} \\ \sqrt{\dfrac{\mu}{2}}\sin\theta_{c,0} \end{bmatrix} \tag{A.10}$$

The last terms u_3, u_4 are derived similarly to what is done in Broucke [3]: starting from the energy in Cartesian coordinates

$$E(x, y, \dot{x}, \dot{y}) = \frac{1}{2}\left(\dot{x}^2 + \dot{y}^2\right) - U_3(x, y) \tag{A.11}$$

through Eq. (2.20b), it follows

$$\dot{x}^2 + \dot{y}^2 = \frac{2}{r_0}\left(u_3^2 + u_4^2\right) \tag{A.12}$$

so, by multiplying both left- and right-hand side in Eq. (A.11) for $r_0 = r_2$ (since the singularity is at the Moon), it is obtained

$$\begin{aligned} r_2 E(\boldsymbol{u}) &= 2\left(u_3^2 + u_4^2\right) - U_3\left(x(\boldsymbol{u}), y(\boldsymbol{u})\right) \\ &= 2\left(u_3^2 + u_4^2\right) - \frac{r_2}{2}\left(x(\boldsymbol{u})^2 + y(\boldsymbol{u})^2\right) - r_2\frac{1-\mu}{r_1} - \mu - r_2\frac{\mu(1-\mu)}{2} \end{aligned} \tag{A.13}$$

then, by setting $r_2 \to 0$ the final result follows as

$$u_3^2 + u_4^2 = \frac{\mu}{2} \tag{A.14}$$

Including a parametrizing angle θ_C, referred to in this report as collision angle, Eq. (A.10) is obtained.

Zero-level patching approach

In Section 5.3.2 a zero-level patching strategy is employed at the Moon to approximate the connection of two consecutive double-collision M2M transfers; here the theory behind this patching is discussed. Briefly, accounting to the shape of the database, as explained in Eq. (5.7), one can assume that for the whole duration of the connecting fly-by, both $\bar{C}$ and the solar phase angle θ_S do not change. However, the lunar ejection angle θ_E is modified by the lunar close passage, by the assumption of an instantaneous fly-by.
With the fly-by equations in the background (Wakker [34]), the position and velocity of the spacecraft are obtained, in an inertial reference frame centered on the flown-by object, namely the Moon. The position and velocity at the lunar crossing in the inertial frame, $\boldsymbol{r}_i$, $\boldsymbol{v}_i$ respectively, are employed to obtain the asymptotic velocity with respect to the Moon $v_{\infty,M}$ as

$$v_{\infty,M} = \sqrt{\|\boldsymbol{v}_i\|^2 - v_{esc}^2} = \sqrt{\|\boldsymbol{v}_i\|^2 - \frac{2\mu_M}{\|\boldsymbol{r}_i\|}} \tag{A.15}$$

where μ_M represents the gravitational parameter of the Moon. Consequently, imposing as a minimum and maximum perilune radius r_p 100 km above lunar surface and the boundary of Hill's sphere, respectively, the deflection angle α can be computed as

$$\alpha = 2\arcsin\left(\frac{1}{1 + r_p v_{\infty,M}^2/\mu_M}\right) \tag{A.16}$$

To connect the final state of the i^{th} M2M transfer with the initial state of the $(i+1)^{th}$ one, the new ejection angle, after geometrical considerations about prograde fly-by, becomes

$$\theta_{E,0}^{i+1} = \theta_{E,end}^{i} + \alpha - 2\pi \tag{A.17}$$

B

Code validation

Levi Civita propagation scheme validation

The Levi Civita regularized system of equations, described in Eq. (2.21), is compared to the results of Oshima et al. [21], thanks to the kind help of the first author in providing the originating scripts. Their results are compared to what is derived from the model employed throughout this report, showing a perfect agreement, as depicted in Fig. B.1a for orbits propagated for $t_{end} \approx -4.3$ days and equal set of initial conditions. In Fig. B.1b the $\Delta\bar{C}$ between the report's and the Oshima et al.'s originated lunar ejection orbits at t_{end}, versus the associated originating θ_C is reported, further confirming the correctness of the employed model: the differences are due to numerical discrepancies, originating from different strategies used to write the same model.

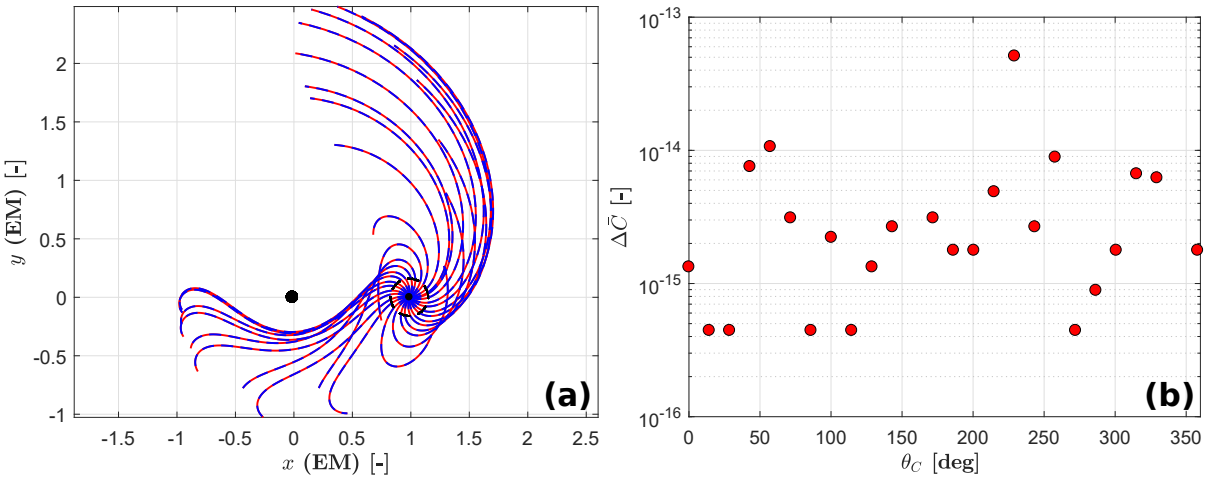

Figure B.1: **(a)** Orbits from [21] (straight red) compared to the ones originated from the dynamical model employed in this report (dashed blue) for different starting collision angles θ_C; **(b)** difference in $\bar{C}$ between straight red and dashed blue orbits of (a) versus the relative value of θ_C.

BR4BP validation

The BR4BP dynamical model, described in Eq. (2.18) is compared to the results of the online supplement material of Topputo [29]. By validating the BR4BP model, the CR3BP is implicitly validated, being the latter a simplification of the former ($\mu_S = 0$).

Since it is really hard to find a properly well-propagated trajectory in the BR4BP in the available literature, the model employed in this report is considered as validated if the results agree in terms of position with the referenced material: indeed, in his work Topputo provided initial conditions for different Earth-to-Moon transfers, whose final state should comply with the requirement of a radial distance from the Moon of 100 km.

The (x) solution, reported in Fig. 8 in [29] is here used as a validating sample. The resulting trajectory, propagated with the dynamical model used throughout this report, is depicted in Fig. B.2a in the Earth-centered inertial reference frame: the trajectory starts in the neighbourhood of the Earth, ending in proximity of the lunar orbit about the Earth.
A magnification of the transfer in proximity of the Moon, plotted in the synodic frame in Fig. B.2b, further supports the evident correctness of the implemented dynamical model: the ending point, marked by the red dot, perfectly meets the dashed line, corresponding to the 100 km circular orbit about the Moon (shown as a straight black line).

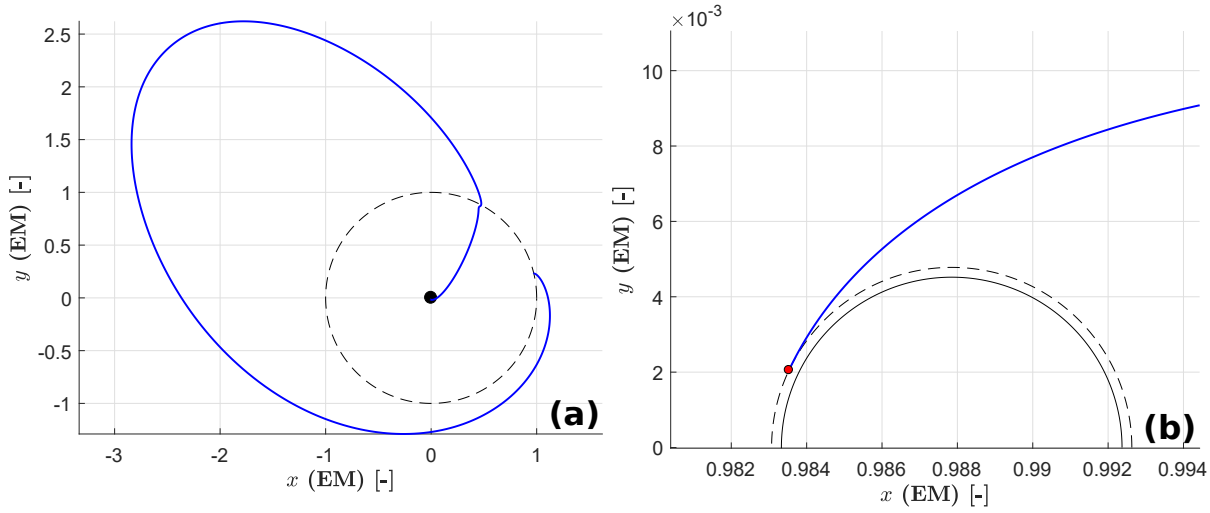

Figure B.2: **(a)** (x) trajectory (blue) in the Earth-centered inertial reference frame from Fig. 8 of [29], propagated with the dynamical model used in this report. Earth referred to as black central dot, while lunar circular orbit depicted as a dashed black line; **(b)** magnification of (a), in the synodic barycentric reference frame. Ending point for the trajectory (red dot) intersects the 100 km circular orbit (dashed black line) about the Moon (straight black line).

Propagator selection

Throughout this report, the `ode113` built-in MATLAB function is used as a propagator. It represents a fully variable step-size, multi-step, nonstiff, PECE implementation of an Adams-Moulton-Bashforth propagator, employed to solve for a system of ordinary differential equation, like the one highlighted in Eq. (2.8).
Although specifically indicated, thanks to its characteristics, for problems like orbital dynamics, `ode113` precision and propagation time is here compared to the famous explicit Runge-Kutta (4,5) [26] and the third-party implemented Runge-Kutta (7,8) [9], both with Dorman and Prince formulation. All the relevant subject has already been treated in author's previous literature study, therefore it is not here repeated.
Two different orbits are propagated for 250 terrestrial days with the CR3BP dynamical model. The resulting absolute shift in Jacobi constant $\Delta\bar{C} = |\bar{C}_{start} - J(\boldsymbol{x}(t_i))|$ is computed along the orbit and shown for the three propagators in Fig. B.3, supported by the required computational time in Table B.1.
Although the precision is case-depending (for example, `ode78` outperforms for orbits spiralling outwards), `ode113` is chosen for its speed, due to the large amount of computed trajectories, and to its robustness (compared to the less reliable `ode78`).

Propagator	`ode113`	`ode45`	`ode78`
Fig. B.3a comp. time [s]	0.885	4.298	0.969
Fig. B.3b comp. time [s]	0.297	1.999	0.371

Table B.1: Computational time for the two orbits in Fig. B.3 for the different propagation schemes.

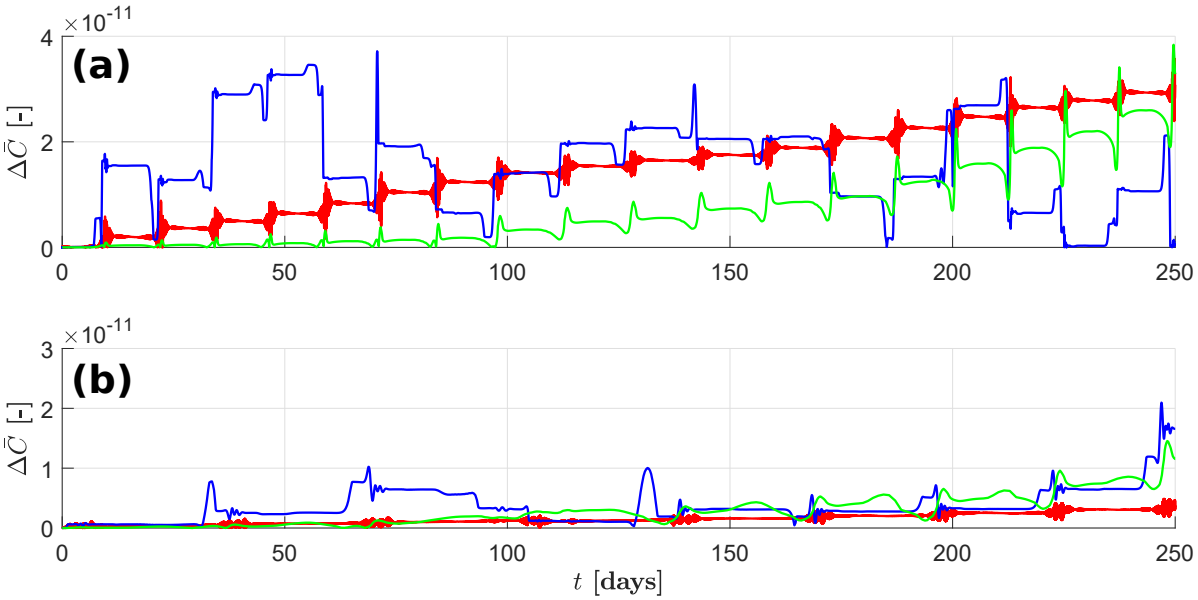

Figure B.3: Trend of Jacobi constant difference $\Delta\bar{C} = |\bar{C}_{start} - \bar{C}_i|$ compared to time. Two different orbits compared in **(a)** and **(b)** respectively, revolving in the vicinity of the system (i.e. not spiralling outwards). `ode113`, `ode45` and `ode78` in blue, red and green respectively.

Bibliography

[1] C.H. Acton. Ancillary Data Services of NASA's Navigation and Ancillary Information Facility. *Planetary and Space Science, 44*, pages 65 – 70, 1996.

[2] J.T. Betts. *Practical Methods for Optimal Control and Estimation Using Nonlinear Programming*. Society for Industrial and Applied Mathematics, 1st edition, 2001. doi: 10.1137/1.9780898718577.

[3] B. Broucke. Periodic collision orbits in the elliptic restricted three-body problem. *Cel. Mech., 3*, pages 461–477, 1971. doi: 10.1007/BF01227792.

[4] V.S. Bruno, Y. Kawakatsu, and T. Arai. Design of a Multiple Flyby Mission to the Phaethon–Geminid Complex. *Journal of Spacecraft and Rockets, 52*, pages 739–745, 2015. doi: 10.2514/1.A33130.

[5] S. Campagnola and R.P. Russell. Endgame Problem Part 2: Multibody Technique and the Tisserand–Poincaré Graph. *Journal of Guidance, Control, and Dynamics, 33*, pages 476 – 486, 2010. doi: 10.2514/1.44290.

[6] C. Castilho and C. Vidal. Regularization of Restricted 3-Body Problems. *Qual. Theory Dyn. Syst., 7*, pages 451–466, 2009. doi: 10.1007/s12346-008-0026-x.

[7] C.C. Conley. Low energy transit orbits in the restricted three-body problem. *SIAM J. Appl. Math.*, pages 732–746, 1968.

[8] G. Gómez, W.S. Koon, M.W. Lo, J.E. Marsden, J. Masdemont, and S.D. Ross. Connecting orbits and invariant manifolds in the spatial restricted three-body problem. *Nonlinearity, 17*, pages 1571 – 1606, 2004.

[9] V.N. Govorukhin. MATDS. http://www.math.rsu.ru/mexmat/kvm/matds/, 2003. Accessed: 2017-08-14.

[10] M. Hénon. Numerical Exploration of the Restricted Problem. V. Hill's Case: Periodic Orbits and Their Stability. *Astron. & Astrophys., 1*, pages 223 – 238, 1969.

[11] M. Hénon. A Trust Region Method Based on Interior Point Techniques for Nonlinear Programming. *Mathematical Programming, 89*, pages 149 – 185, 2000.

[12] K.C. Howell. Three-dimensional, Periodic, 'Halo' Orbits. *Cel. Mech., 32*, pages 53 – 71, 1984. doi: 10.1007/BF01358403.

[13] W.S. Koon, M.W. Lo, J.E. Marsden, and S.D. Ross. Design of a Multi-Moon Orbiter. 2003.

[14] W.S. Koon, M.W. Lo, J.E. Marsden, and S.D. Ross. *Dynamical Systems, the Three-Body Problem and Space Mission Design*. Marsden Books, 2011.

[15] G. Lantoine and T.P. McElrath. Families of solar-perturbed Moon-to-Moon transfers. 2014.

[16] E. Lega, M. Guzzo, and C. Froeschlé. Detection of close encounters and resonances in three-body problems through Levi-Civita regularization. *Mon. Not. R. Astron. Soc., 418*, pages 107–113, 2011.

[17] T. Levi Civita. Sur la régularisation du problème des trois corps. *Acta Math. ,42*, pages 99–144, 1920.

[18] J.L. Lissauer and I. de Pater. *Fundamental Planetary Science: Physics, Chemistry and Habitability*. Cambridge, 1st edition, 2013.

[19] Mathworks. fmincon. https://it.mathworks.com/help/optim/ug/fmincon.html, 2006. Accessed: 2017-08-07.

[20] A. Miele. Revisit of the Theorem of Image Trajectories in the Earth-Moon Space. *Journal of Optimization Theory and Applications,147*, pages 483–490, 2010.

[21] F. Oshima, K. and·Topputo, S. Campagnola, and T. Yanao. Analysis of medium-energy transfers to the Moon. *Celest. Mech. Dyn. Astr. ,127*, page 285, 2017. doi: 10.1007/s10569-016-9727-7.

[22] K. Oshima, S. Campagnola, C.H Yam, Y. Kayama, Y. Kawakatsu, Q. Verspieren, K. Kakihara, K. Oguri, and R. Funase. EQUULEUS Mission Analysis: Design of the Transfer Phase. 2017.

[23] J.S. Parker and R.L. Anderson. *Low-Energy Lunar Trajectory Design.* Wiley, 2014.

[24] Y. Qi and S. Xu. Mechanical analysis of lunar gravity assist in the Earth–Moon system. *Astrophys Space Sci. 360*, page 55, 2015.

[25] D.J. Scheeres. *Orbital motion in strongly perturbed environments. Applications to Asteroid, Comet and Planetary Satellite Orbiters.* Springer, 2012. doi: 10.1007/978-3-642-03256-1.

[26] L. F. Shampine and M. W. Reichelt. The MATLAB ODE Suite. *SIAM Journal on Scientific Computing, 18*, pages 1 – 22, 1997. doi: 10.1088/0951-7715/17/5/002.

[27] C. Simó, G. Gómez, Á. Jorba, and J. Masdemont. The Bicircular Model Near the Triangular Libration Points of the RTBP. *From Newton to Chaos. Plenum Press, New York*, 1995.

[28] V. Szebehely. *Theory of Orbits: The Restricted Problem of Three Bodies.* Academic, New York, 1967.

[29] F. Topputo. On optimal two-impulse Earth–Moon transfers in a four-body model. *Celest. Mech. Dyn. Astron. 117*, pages 279–313, 2013.

[30] K. Uesugi. Results of the MUSES-A "Hiten" mission. *Advances in Space Research, 18*, pages 69–72, 1996. doi: 10.1016/0273-1177(96)00090-7.

[31] K. Uesugi, H. Matsuo, J. Kawaguchi, and T. Hayashi. Japanese first double lunar swingby mission "Hiten". *Acta Astronautica, 25*, pages 347 – 355, 1991. doi: 10.1016/0094-5765(91)90014-V.

[32] M. Valtonen and H. Karttunen. *The Three-Body problem.* Cambridge, 2005.

[33] F. Verhulst. *Nonlinear Differential Equations and Dynamical Systems.* Springer, 2nd edition, 2006.

[34] K.F. Wakker. *Fundamentals of Astrodynamics.* Institutional Repository Library, Delft University of Technology, 1st edition, 2015.

[35] T. Yamamoto, S. Sato, Y. Kawabata, S. Campagnola, B.V. Sarli, S. Ogura, and Y. Kawakatsu. Mission design of DESTINY+. 2016.

[36] D.G. Yarnoz, C.H. Yam, S. Campagnola, and Y. Kawakatsu. Extended Tisserand-Poincaré graph and multiple lunar swingby design with Sun perturbation. 201.